A Study of D-State Upsilon Spectroscopy Using Lattice QCD

Mark Campbell

Department of Physics and Astronomy
University of Glasgow

Thesis submitted to the University of Glasgow
for the degree of Master of Science
February 1998

Acknowledgements

I would like to give special thanks to my two supervisors Sara Collins and Christine Davies for their help and guidance over the last year and a half. Thanks must also go to another member of the NRQCD collaboration; John Sloan, for several interesting and useful discussions. I must also thank two members of the group, Paul McCallum and Joachem Hein for their assistance and advice. Lastly I would like to thank the other members of the theory group; Alex, David, Gordon, Gunner, Laurence, Mark, Nektarios, Peter B, Peter C and Susan.

Declaration

Apart from chapters 1, 2 and 3 and except where specific reference is made to the work of others, this thesis has been composed by the author.

Contents

Abstract

The theory of nonrelativistic QCD, developed by the NRQCD collaboration, is employed in simulations producing the D states of the upsilon system in the quenched approximation. Correlations are analysed using multi-correlation fitting routines to obtain energies and amplitudes for the ground and first excited states. Since the D states have never been observed, comparison of the simulation results cannot be made with the experimental upsilon spectrum. However various phenomenological potential model studies have been made and their results can be used as an estimation of the D state part of the upsilon spectrum. The D state spectrum at $\beta = 6.0$ is studied in detail and the ground state of $^1D_2$ is studied at $\beta = 5.7$ to test the scaling of the results at the two different lattice spacings.

Chapter 1

Introduction to Lattice QCD

1.1 Introduction

The traditional goal of particle physics has been to identify what appear to be point-like units of matter, and to understand the nature of the forces acting between them. Briefly there are two fundamental types of matter: leptons and quarks. Both are spin-1/2 fermions and are structureless at the smallest distances currently probed by the highest energy accelerators. The interactions of these fundamental particles are described by a highly successful model called the Standard Model (SM), where the fermions interact with each other via the exchange of gauge bosons. To understand the nature of these interactions requires the principle of gauge invariance, where the SM demands invariance under the gauge group of rotations $SU(3) \otimes SU(2) \otimes U(1)$. The gauge group $SU(2) \otimes U(1)$ defines the electroweak interaction describing the interactions between leptons and the W and Z gauge bosons, with the symmetry breaking at low energies to $U(1)$ of Quantum Electrodynamics (QED). The gauge group $SU(3)$ describes Quantum Chromodynamics (QCD), the theory of the strong interaction of quarks and gluons. QCD incorporates the $SU(3)$ group to account for the property of quarks and gluons known as colour, which both types of particle are believed to carry. Although quarks and gluons are only ever observed as constituents of colourless objects known as hadrons, which can be split into two types: baryons

and mesons. Baryons are formed from three quarks, each having one of the three colours of the $SU(3)$ colour group, while mesons are formed from a quark and an antiquark, the antiquark possessing the anticolour corresponding to that of the quark. Quarks also come in six known flavours, up, down, strange, charm, bottom and top.

In the past perturbation theory was used to great success in QED to calculate physical quantities of interest such as matrix elements and scattering amplitudes. This involves the use of a power series expansion in the coupling constant of the appropriate fermion and gauge boson: the electron and photon. The higher orders generally represent very complicated processes involving the exchange of virtual photons between electrons. Calculations in QED are relatively easy to solve since the coupling constant between electrons and photons is a small number $\alpha_e \approx \mathcal{O}(1/137)$ making the power series very convergent. However, unlike QED, QCD is a non-Abelian gauge theory and consequently displays properties associated with this type of theory. For example the coupling constant in QCD, α_s displays a property known as asymptotic freedom. Asymptotic freedom means that the coupling goes to zero as the quark separation becomes very small, and at distances less than about 0.1 fm the lowest order diagrams in perturbation theory dominate. At these distances quark-quark scattering, for example, is given approximately by one-gluon exchange diagrams and it is in this short-distance region that perturbative QCD has been highly successful for analysing high energy phenomenon such as Bjorken scaling. However, as the distance between the quarks increases, the interaction gets stronger, and many higher order diagrams become important. Another consequence of the non-Abelian nature of QCD is confinement; at distances of order 1 fm, quarks are confined into bound states called hadrons and at these medium and low energy scales the coupling is $\alpha_s \approx \mathcal{O}(1)$, and so perturbation theory breaks down, thus a non-perturbative treatment of QCD is required to study fundamental properties of hadrons such as quark confinement and the hadron mass spectrum.

1.2 Defining QCD

In order to describe the true hadron picture, it is important to obtain an appropriate Lagrangian density $\mathcal{L}_{QCD}$ and use this as the starting point for a quantum field theory of quarks and gluons. This Lagrangian must contain a kinetic term for the quarks:

$$\mathcal{L}_q^{(0)}(x) = \sum_{j=1}^{f} \overline{\psi}_j(x)(i\gamma^\mu \partial_\mu - m_j)\psi_j(x) \tag{1.1}$$

where $j = 1, \ldots, f$ numbers the different quark flavours and m_j denotes their masses. The quark fields ψ_j have three colour components

$$\psi_j = \begin{pmatrix} \psi_j^1 \\ \psi_j^2 \\ \psi_j^3 \end{pmatrix} \tag{1.2}$$

The Lagrangian density $\mathcal{L}_q^{(0)}$ cannot itself be satisfactory since $\mathcal{L}_q^{(0)}$ only describes the motion of free quarks. But there is a more subtle physical reason why $\mathcal{L}_q^{(0)}$ is unacceptable. Hadrons are colour singlet states, for example a π^+-meson can be imagined as a bound state of a u and a $\overline{d}$ quark:

$$\pi^+ \sim u_1\overline{d}_1 + u_2\overline{d}_2 + u_3\overline{d}_3 \tag{1.3}$$

The physical π^+-meson is invariant under $SU(3)$ rotations in colour space. When the bound states display an invariance, this should be a consequence of the underlying Lagrangian density. In fact $\mathcal{L}_q^{(0)}$ is invariant under the following $SU(3)$ colour transformation

$$\psi_j(x) \rightarrow U\psi_j(x) \qquad \text{(j=1,...,f)} \tag{1.4}$$

where $UU^\dagger$=1, $detU$=1 and U is independent of x. The important point here is that U is a constant matrix. This means that with $\mathcal{L}_q^{(0)}$, we can choose the unobserved directions of the axes in colour space in any manner we like. They must however be defined globally, that is the directions of the axes must be the

same at every point in the universe, which is very unsatisfactory since it would give the relative orientation in colour space at different space-time points absolute significance, even though there are no corresponding observable effects.

In the case of classical electrodynamics, Weyl discovered a principle that can be regarded as the "reason" for the existence of the photon. The starting point is the Lagrangian density for a free Dirac electron:

$$\mathcal{L}_e^{(0)} = \overline{\psi}(x)(i\gamma^\mu \partial_\mu - m_e)\psi(x) \tag{1.5}$$

Typical observable quantities are bilinear expressions, e.g. the current density

$$j^\mu = \overline{\psi}\gamma^\mu \psi(x) \tag{1.6}$$

These observables are unchanged when $\psi(x)$ is multiplied by a phase factor. The phase factor can have an arbitrary x-dependence and we make the substitution

$$\psi(x) \rightarrow \psi'(x) = e^{i\alpha(x)}\psi(x) \tag{1.7}$$

We can see immediately that the Lagrangian $\mathcal{L}_e^{(0)}$ is not invariant under the above phase transformation. Weyl discovered that the coupled system of electrons and photons, which is described by the Maxwell-Dirac Lagrangian, is invariant under the above transformation and is given for completeness by

$$\mathcal{L}_{MD} = \overline{\psi}(x)(i\gamma^\mu D_\mu - m_e)\psi(x) - \frac{1}{4}F_{\mu\nu}F^{\mu\nu} \tag{1.8}$$

Here $F_{\mu\nu}$ is the field-strength tensor, and D_μ is the covariant derivative:

$$\begin{aligned} F_{\mu\nu} &= \partial_\mu A_\nu(x) - \partial_\nu A_\mu(x) \\ D_\mu\psi(x) &= (\partial_\mu - ieA_\mu(x))\psi(x) \end{aligned} \tag{1.9}$$

and the electron charge is given by $(-e)$. It is easily shown that $\mathcal{L}_{MD}$ is invariant under the following 'gauge' transformations:

$$\begin{aligned} \psi(x) &\rightarrow e^{i\alpha(x)}\psi(x) \\ A_\mu(x) &\rightarrow A_\mu(x) + \frac{1}{e}\partial_\mu\alpha(x) \end{aligned} \tag{1.10}$$

Here $\alpha(x)$ is an arbitrary real function of x. In formal terminology, these transformations are said to form a $U(1)$ gauge group. Weyl interpreted this result to mean that the invariance of the Dirac field under the phase transformation (1.10) can be thought of as a "reason" for the existence of the photon.

Returning to QCD, it is possible to construct a Lagrangian density along similar lines to electrodynamics. It should be possible to choose the directions of the axes in colour space completely freely at all space-time points, since they are unobserved. Indeed, since all hadrons are colour singlets, we can demand gauge invariance under local gauge transformation in colour space:

$$\psi_j(x) \rightarrow U(x)\psi_j(x) \tag{1.11}$$

where $U(x)$ is an $SU(3)$ matrix and for all x it must hold that

$$U(x)U^\dagger(x) = 1 \qquad \text{and} \qquad detU(x) = 1 \tag{1.12}$$

It is easy to see that the Lagrangian of the free quark fields $\mathcal{L}_q^{(0)}$ is not invariant under (1.11). The way to save the invariance was discovered by Yang whilst investigating non-Abelian gauge theories. As seen above for electrodynamics, the gauge principle was saved by the introduction of photons. Analogously the gauge principle of QCD also requires the introduction of vector fields, which of course represent the gluons. We need eight gluons corresponding to the eight linearly independent generators of the $SU(3)$ colour group. The eight real gluon vector potentials $A_\mu^a(x)$ (with $a = 1, \ldots, 8$) are combined into a 3×3 Hermitian traceless matrix

$$\begin{aligned} A_\mu(x) &= A_\mu^a(x)\frac{\lambda_a}{2} = A_\mu^\dagger(x) \\ & \quad TrA_\mu(x) = 0 \end{aligned} \tag{1.13}$$

The λ_a are the Gell-Mann λ-matrices [3] now operating in colour space. For the coupling of the gluons to the quarks, we can use a 'minimal' substitution as in electrodynamics, i.e replace all partial derivatives ∂_μ with

$$\partial_\mu \rightarrow D_\mu = \partial_\mu + ig_s A_\mu(x) \tag{1.14}$$

where the quantity D_μ is the covariant derivative and g_s is a dimensionless coupling constant analogous to the electronic charge e. With this substitution, we obtain from $\mathcal{L}_q^{(0)}$ the following expression:

$$\mathcal{L}_q(x) = \sum_{j=1}^{f} \overline{\psi}_j(x)(i\gamma^\mu D_\mu - m_j)\psi_j(x) \tag{1.15}$$

It is easy to see that $\mathcal{L}_q$ is invariant under local gauge transformations (1.11), provided the gluon field is transformed as follows:

$$A_\mu(x) \rightarrow A'_\mu(x) = U(x)A_\mu(x)U^\dagger(x) - \frac{i}{g_s}U(x)\partial_\mu U^\dagger(x) \tag{1.16}$$

where the matrix $A'_\mu(x)$ is also Hermitian and traceless for any $U(x)$ that satisfies the conditions (1.12).

Nothing useful can be been gained from this treatment as long as the vector potential $A_\mu(x)$ of the gluons is treated as an external field. The gluon field itself must become a dynamical variable. In order to construct the part of the Lagrangian that contains the gluons dynamics, we introduce a gluon field-strength tensor $A_{\mu\nu}(x)$, in analogy with the electromagnetic field-strength tensor

$$F_{\mu\nu}(x) = \partial_\mu A_\nu(x) - \partial_\nu A_\mu(x) + ig_s[A_\mu(x), A_\nu(x)] \tag{1.17}$$

which for fixed x is Hermitian with zero trace. Thus we define its components by

$$F_{\mu\nu}(x) = A^a_{\mu\nu}(x)\frac{\lambda_a}{2} \tag{1.18}$$

and obtain from (1.17)

$$F^a_{\mu\nu} = \partial_\mu A^a_\nu(x) - \partial_\nu A^a_\mu(x) - g_s f_{abc} A^b_\mu(x) A^c_\nu(x) \tag{1.19}$$

The f_{abc} are the structure constants of the $SU(3)$ group [3] and are defined by the commutation relation

$$[\lambda_a, \lambda_b] = 2if_{abc}\lambda_c \tag{1.20}$$

The quadratic term in the gluon field has no analogue in electrodynamics and is typical of the non-Abelian nature of the $SU(3)$ colour group. The term is necessary in order to achieve a simple transformation behaviour for the field-strength tensors under gauge transformations, i.e.

$$F_{\mu\nu}(x) \rightarrow U(x)F_{\mu\nu}(x)U^{\dagger}(x) \tag{1.21}$$

It is now possible to write down a gauge invariant Lagrangian density for quarks and gluons

$$\mathcal{L}_{QCD} = \sum_{A,B,j} \overline{\psi}_q^A(x)\left(i\gamma^{\mu}[D_{\mu}]_{AB} - m_j\delta_{AB}\right)\psi_j^B(x) - \frac{1}{4}F^a_{\mu\nu}F_a^{\mu\nu} \tag{1.22}$$

where the summation over A, B represents the quark colour ($A = 1, 2, 3$) and j represents the quark flavour. D_{μ} is the covariant derivative and $F^a_{\mu\nu}$ is the gluon field-strength tensor defined by

$$[D_{\mu}]_{AB} = \delta_{AB}\partial_{\mu} + ig[\frac{\lambda_a}{2}]_{AB}A^a_{\mu}(x) \tag{1.23}$$

and

$$F^a_{\mu\nu} = \partial_{\mu}F^a_{\nu} - \partial_{\nu}F^a_{\mu} - gf_{abc}F^b_{\mu}F^c_{\nu} \tag{1.24}$$

a sum is implied over the eight gluon colour fields $A^a_{\mu}(x)$.

1.2.1 Bottomium

The upsilon (Υ) meson, which is the subject of this thesis, is a bound state composed of the bottom quark (b) and its antiquark ($\overline{b}$). Since quarks do not, apparently, exist as free isolated particles, it is not straightforward to decide how

to define their mass. However, for the heavier meson states (such as $c\bar{c}$ and $b\bar{b}$) an approximation can be made by supposing the major contribution to the hadronic mass is given by an effective quark mass contributing additively. Thus from experimental values from the $c\bar{c}$ states of mass ~ 3 GeV, $m_c \sim 1.5$ GeV, and from the $b\bar{b}$ ones at ~ 10 GeV, $m_b \sim 5$ GeV, in very rough terms [4]. The average value for the square of the velocity of the b quark in the Υ is estimated from potential models (See Chapter 2) as $v^2 \sim 0.1$, which is essentially nonrelativistic. This gives an average b quark momentum (and consequently gluon energy) of $\mathcal{O}(M_b V) \sim 1.4$ GeV. In this low energy regime, the strong coupling $\alpha_s \sim \mathcal{O}(1)$ and so perturbation theory is not applicable here. This means that an alternative method has to be employed to study the Υ system, which leads to the subject of the next section, Lattice gauge theory.

1.3 Lattice QCD

Having examined the formulation for QCD it is necessary to discuss the starting point for lattice calculations of non-perturbative quantities: Feynman's sum over paths formulation of quantum field theory. Feynman's approach allows us to calculate the expectation values of time ordered products of field operators as a path integral of the form

$$\langle 0|\mathcal{T}(\hat{\phi}_{j_1}(x_1)\ldots\hat{\phi}_{j_n}(x_n))|0\rangle = \frac{1}{Z[\phi]}\int\prod_k \mathcal{D}\phi_k \phi_{j_1}(x_1)\ldots\phi_{j_n}(x_n)\exp\left(iS[\phi]\right) \tag{1.25}$$

where $\mathcal{D}\phi_k$ is the integration measure and S is the action of the theory. The term in the denominator $Z[\phi]$ is called the vacuum functional and is defined such that $\langle 0|1|0\rangle = 1$. Z is given explicitly as

$$Z[\phi] = \int\prod_k \mathcal{D}\phi_k \exp\left(iS[\phi]\right) \tag{1.26}$$

It would be impossible to extract measurable, low energy quantities for QCD analytically using the path integral expressions above since the path integrals do

not have a perturbative expansion in this regime. However after an important modification, the path integral expressions (1.25) and (1.26) can be applied to first principles calculations in QCD using lattice theory. The need for a modification can be appreciated by noting that the quantum amplitudes of (1.25) and (1.26) are very difficult to study numerically because of the rapidly oscillating complex exponentials. To deal with this, we perform a Wick rotation, where we rotate time into an imaginary direction:

$$t \rightarrow i\tau \tag{1.27}$$

This has the effect of converting the oscillating factors $\sim \exp(iS)$ into exponentially decreasing functions $\sim \exp(-S_E)$, so that now they appear much more like classical weighting functions, the most important path still being the one of least S_E. The subscript 'E' stands for Euclidean, since we have now moved from Minkowski space with an invariant squared length of $t^2 - \mathbf{x}^2$ to a four-dimensional Euclidean space with squared length $-\tau^2 - \mathbf{x}^2$. This Euclidean version of quantum field theory, when put on a lattice, is in fact analogous to a statistical mechanical system. The connection is made by observing that in Euclidean space, the equation (1.26) is of the same form as the fundamental quantity of statistical mechanics, the partition function Z

$$Z = \int \prod_k \mathcal{D}\phi_k \exp(-S_E) \tag{1.28}$$

This relationship allows the large number of numerical techniques available in statistical mechanics to be applied to lattice field theory.

Field theories, such as QCD have an infinite number of degrees of freedom. So in order to give path integral calculations meaning (which are well defined only for systems with a finite number of degrees of freedom), we have to split up space-time into a four-dimensional lattice of discrete points with lattice spacing a on a finite volume, i.e, the lattice provides a well defined regularisation of QCD. Coordinates in this space-time lattice are restricted to these points using integer multiples of the lattice spacing a

$$x_\mu \rightarrow n_\mu a \tag{1.29}$$

Continuum integration is replaced by a summation

$$\int d^4x \rightarrow a^4 \sum_n \tag{1.30}$$

and continuum derivatives are replaced by finite differences and will be discussed in section (1.3.2) and in chapter 3.

1.3.1 Gauge Fields on the Lattice

In a lattice formulation of QCD, the fermion fields are only defined on the lattice sites. The representation chosen for the gauge fields $A_\mu(x)$ on the lattice is determined by the requirement that gauge invariance be preserved. In the continuum, in order to construct a gauge-invariant scalar bilinear term from the fields $\overline{\psi}(x)$ and $\psi(y)$, the field $\psi(y)$ must undergo parallel transport from point y to point x using the path-ordered parallel transporter

$$U(x,y) = \mathcal{P} e^{ig\int_x^y A_\mu(z)dz_\mu} \tag{1.31}$$

Thus the quantity

$$\overline{\psi}(x)U(x,y)\psi(y) \tag{1.32}$$

is gauge invariant. This suggests that on the lattice the gauge fields should be associated with the links between neighbouring lattice sites. If x and y are neighbouring sites, the path-ordered integral runs along the connecting link, and if we assume that $|x-y| = a$, is sufficiently small we can approximate the integral by

$$U(x, x+a\hat{\mu}) = U_\mu(x) \simeq e^{igaA_\mu(x+a\hat{\mu})} \tag{1.33}$$

Hence, gauge invariance dictates that the gauge variables be $SU(3)$ matrices. Conventionally U_μ is known as a link variable since it lives on the link connecting

Figure 1.1: Link variables

two neighbouring sites. U_μ can be denoted by $U_{n,n+\hat{\mu}}$ as it is a directed quantity from the site n to $n+\hat{\mu}$. Similarly the hermitian quantity $U_\mu^\dagger$ can be denoted by $U_{n,n+\hat{\mu}}^\dagger$ which is directed in the opposite direction. See fig (1.1).

The gauge link undergoes the local transformation

$$U_{n,n+\hat{\mu}} \rightarrow G(n)U_{n,n+\hat{\mu}}G^{-1}(n+\hat{\mu}) \tag{1.34}$$

where the matrix $G(n)$ is a member of the $SU(3)$ group and is local to the site n. A construction of a lattice version of the continuum gauge action should be strictly gauge-invariant as in the continuum case, and be a function of link variables only. Such gauge invariant functions are easily formed by taking the product of link variables around closed loops on the Euclidean space-time lattice. Since $U_\mu(n)$ transforms as (1.34), the simplest gauge-invariant quantity one can build from the elements $U_\mu(n)$, is the trace of the path ordered product of link variables along the boundary of an elementary plaquette. See fig (1.2).

$$U_P(n) = U_{\mu\nu}(n) = U_\mu(n)U_\nu(n+\hat{\mu})U_\mu^\dagger(n+\hat{\nu})U_\nu^\dagger(n) \tag{1.35}$$

It can be shown to $\mathcal{O}(a^2)$ that

$$U_{\mu\nu}^P(n) = e^{ig_0a^2F_{\mu\nu}(n)} \tag{1.36}$$

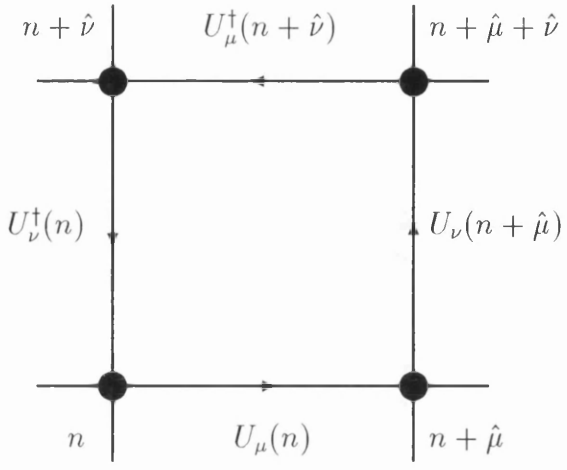

Figure 1.2: The plaquette in the $\mu\nu$-plane is made from four gauge links formed in an anticlockwise direction.

From this it is straightforward to show that the gauge field action on the lattice is given by

$$S_G = \beta \sum_n \sum_{\mu<\nu} \left[1 - \frac{Tr}{6} \left(U^P_{\mu\nu}(n) + U^{P\dagger}_{\mu\nu}(n) \right) \right] \tag{1.37}$$

where $\beta = \frac{6}{g_0^2}$ is often used to specify the size of the lattice spacing, since g is a function of a [2].

This expression reduces to the continuum Euclidean gauge action

$$S_G = \int d^4x \frac{1}{2} Tr(F^{\mu\nu} F_{\mu\nu}) \tag{1.38}$$

as the lattice spacing tends to zero.

1.3.2 Fermions on the Lattice

Consider the Dirac equation in Minkowski space

$$(i\gamma^\mu \partial_\mu - M)\psi(x) = 0 \tag{1.39}$$

where γ^μ are the Dirac matrices satisfying the following anti-commutation relations and ψ is a four component spinor

$$\{\gamma^\mu, \gamma^\nu\} = 2g^{\mu\nu}$$

This equation of motion follows from the action

$$S_F = [\psi, \overline{\psi}] = \int d^4x \overline{\psi}(x)(i\gamma^\mu \partial_\mu - M)\psi(x) \tag{1.40}$$

For reasons mentioned in the last section we need to go from Minkowski to Euclidean space. This can be achieved by making the transformation to imaginary times, $x^0 \to -ix_4$, $y^0 \to -iy_4$ etc. From now on, x and y denote the Euclidean four vectors with components x_μ and y_μ ($\mu = 1, 2, 3, 4$). In order to transform the fermion action into Euclidean space it is also convenient to express the action in terms of a new set of γ-matrices γ_μ^E ($\mu = 1, ..., 4$) satisfying the algebra

$$\left\{\gamma_\mu^E, \gamma_\nu^E\right\} = 2\delta_{\mu\nu}$$

with the hermitian alternatives $\gamma_4^E = \gamma^0$, $\gamma_i^E = -i\gamma^i$.
Applying these transformations to the fermion action S_F, we obtain the following action for the Euclidean action S_F^E

$$S_F^E = \int d^4x \overline{\psi}(x)(\gamma_\mu^E \partial_\mu + M)\psi(x) \tag{1.41}$$

To make the transition from the continuum to the lattice, the action S_F^E has to be discretised. We do this by making the following substitutions:

$$\begin{aligned} M &\to \frac{1}{a}\hat{M} \\ \psi(x) &\to \frac{1}{a^{3/2}}\hat{\psi}(n) \\ \overline{\psi}(x) &\to \frac{1}{a^{3/2}}\hat{\overline{\psi}}(n) \end{aligned} \tag{1.42}$$

where M,ψ and $\overline{\psi}$ have been scaled according to their canonical dimensions. Finally the derivative acting on the fermion field is replaced by

$$\partial_\mu \psi(x) \rightarrow \frac{1}{a^{5/2}} \hat{\partial}_\mu \hat{\psi}(n) \tag{1.43}$$

where $\hat{\partial}_\mu$ is the lattice derivative defined by

$$\hat{\partial}_\mu \hat{\psi}_\alpha(n) = \frac{1}{2a}\left[\hat{\psi}_\alpha(n + a\hat{\mu}) - \hat{\psi}_\alpha(n - a\hat{\mu})\right] \tag{1.44}$$

Here $\hat{\mu} \equiv \hat{e_\mu}$, where $\hat{e_\mu}$ is a unit vector pointing along the μ direction. Applying the above replacements to the Euclidean fermion action, we obtain

$$S_F^E = \sum_{n,\mu} \frac{1}{2} \overline{\hat{\psi}}_n \left(\gamma_\mu^E \hat{\psi}_{n+\mu} - \gamma_\mu^E \hat{\psi}_{n-\mu}\right) + \hat{M} \overline{\hat{\psi}}_n \hat{\psi}_n \tag{1.45}$$

Alternatively the lattice can be written in the matrix form

$$S_F^E = \sum_{n,m} \hat{\overline{\psi}} K_{nm} \hat{\psi}(m) \tag{1.46}$$

where

$$K_{nm} = \sum_\mu \frac{1}{2} \gamma_\mu [\delta_{m,n+\hat{\mu}} - \delta_{m,n-\hat{\mu}}] + \hat{M} \delta_{m,n} \tag{1.47}$$

The propagator for the free fermion in Euclidean space is given by the inverse matrix $K_{nm}^{-1} = \langle \psi(n) \overline{\psi}(m) \rangle$. The inverse matrix K^{-1} is determined from the relation

$$\sum_l K_{nl} K_{lm}^{-1} = \delta_{nm} \tag{1.48}$$

and is easily obtained by switching to momentum space, where δ_{nm} is given by

$$\delta_{nm} = \int_{-\pi}^{\pi} \frac{d^4\hat{p}}{(2\pi)^4} e^{i\hat{p}(n-m)} \tag{1.49}$$

substituting the above equation into (1.47), one finds that K_{nm} is given by

$$K_{nm} = \int_{-\pi}^{\pi} \frac{d^4 p}{(2\pi)^4} \tilde{K}(p) e^{ip(n-m)} \tag{1.50}$$

where

$$\tilde{K}(\hat{p}) = \sum_{\mu=1}^{4} i\gamma_\mu \sin \hat{p}_\mu + \hat{M} \tag{1.51}$$

It is now easily shown, by using (1.48) that K_{nm}^{-1} is given by

$$K_{nm}^{-1} = \langle \hat{\psi}_n \overline{\hat{\psi}}_m \rangle = \int_{-\pi}^{\pi} \frac{d^4\hat{p}}{(2\pi)^4} \frac{[-i\sum_\mu \gamma_\mu \sin \hat{p}_\mu + \hat{M}\ ]}{\sum_\mu \sin^2 \hat{p}_\mu + \hat{M}^2} e^{ip(n-m)} \tag{1.52}$$

In principle to obtain the continuum version of the fermion propagator $\langle \psi(x)\overline{\psi}(y) \rangle$ we rescale $\hat{\psi}_n$, $\overline{\hat{\psi}}_m$ and $\hat{M}$ according to (1.42) and let $a \to 0$, keeping ψ, $\overline{\psi}$, $x = na$, $y = na$ fixed, i.e.

$$\langle \psi(x)\overline{\psi}(y) \rangle = \lim_{a \to 0} \frac{1}{a^3} G(\frac{x}{a}, \frac{y}{a}; Ma) \tag{1.53}$$

Finally a change is made to the integration variable such that

$$\langle \psi(x)\overline{\psi}(y) \rangle = \int_{-\frac{\pi}{a}}^{\frac{\pi}{a}} \frac{d^4p}{(2\pi)^4} \frac{[-i\sum_\mu \gamma_\mu \frac{1}{a} sin(p_\mu a) + M]}{\sum_\mu \frac{1}{a^2} sin^2(p_\mu a) + M^2} e^{ip(x-y)} \tag{1.54}$$

However, looking at the dispersion relation for such fermions in the free field case one has

$$E^2 = M^2 + \frac{1}{a^2} \sum_i \sin^2(p_i a) \tag{1.55}$$

where $-\frac{\pi}{a} < p_i < \frac{\pi}{a}$. For $p_i \to 0$, $E^2 \to M^2$ which is the energy for a fermion with zero momentum in the low energy region. However for $p_i \to \frac{\pi}{a}$, $E^2 \to M^2$ as well. This is known as the fermion doubling problem, where there is an extra particle in the low energy region even though it's momentum is high. This is purely a lattice artifact and in d dimensions one has 2^d fermions using the naive fermion action (1.45). This problem can be avoided by adding extra terms to the Lagrangian which will disappear in the continuum limit. The most commonly used action is given by Wilson where such a correction term is added to the action (1.45) to give

$$S_F^{(W)} = S_F - \frac{r}{2}\sum_n \hat{\overline{\psi}}(n)\Box\hat{\psi}(n) \tag{1.56}$$

where r is the Wilson parameter. The Wilson action can be written in the form of equ (1.47) where

$$K_{nm} = (\hat{M} + 4r)\delta_{nm} - \frac{1}{2}\sum_\mu[(r - \gamma_\mu)\delta_{m,n+\mu} + (r + \gamma_\mu)\delta_{m,n-\mu}] \tag{1.57}$$

Setting r to unity, the dispersion relation for the Wilson action becomes

$$E^2 = \left[M + \frac{1}{a}(1 - \sum_i \cos p_i)\right]^2 + \frac{1}{a^2}\sum_i \sin^2 p_i \tag{1.58}$$

Taking $p_i \rightarrow 0$ as before one has $E^2 \rightarrow M^2$, but now when $p_i \rightarrow \frac{\pi}{a}$, $E^2 \rightarrow (M + 2a^{-1})$. Approaching the continuum $a \rightarrow 0$, the effective mass becomes infinite and the extra $2^d - 1$ fermions do not propagate and decouple from the theory. The above change to the action leads to the continuum single fermion propagator in Euclidean space, $\langle\psi(x)\overline{\psi}(y)\rangle$, as the lattice spacing goes to zero.

In order to maintain the gauge invariance of the Wilson action $S_F^{(W)}$ in the interacting case, i.e $S_{QCD} = S_F^{(W)} + S_G$, the following substitutions

$$\begin{aligned} \psi(n) &\rightarrow G(n)\psi(n) \\ U_{n,n+\hat{\mu}} &\rightarrow G(n)U_{n,n+\hat{\mu}}G^{-1}(n+\hat{\mu}) \end{aligned} \tag{1.59}$$

must be used to modify $S_F^{(W)}$ to include gauge fields.

$$\begin{aligned} S_F^{(W)} = (\hat{M} + 4r)\sum_n \hat{\overline{\psi}}(n)\hat{\psi}(n) - \frac{1}{2}\sum_{n,\mu}\Big(&\hat{\overline{\psi}}(n)(rI - \gamma_\mu)U_\mu(n)\hat{\psi}(n+\hat{\mu}) \\ &+ \hat{\overline{\psi}}(n+\hat{\mu})(rI + \gamma_\mu)U_\mu^\dagger(n)\hat{\psi}(n)\Big), \end{aligned} \tag{1.60}$$

This procedure is analogous to the treatment given in section (1.2), to ensure gauge invariance in the continuum Lagrangian density $\mathcal{L}_{QCD}$.

1.4 Simulations on the Lattice

After defining the lattice actions for the fermion and gauge fields of QCD and showing that they posses the desired naive continuum limit, they can be used to calculate the hadron spectrum from first principles. As mentioned in section (1.3) the method most readily applicable to lattice theory is that of the path integral in Euclidean space. For the vacuum expectation value of an arbitrary function of the gauge and quark fields, $f(U,\psi,\overline{\psi})$ on the lattice, the path integral is

$$\langle 0|f(U,\psi,\overline{\psi})|0\rangle = \frac{1}{Z}\int \mathcal{D}U\mathcal{D}\psi\mathcal{D}\overline{\psi}\, f(U,\psi,\overline{\psi})e^{-S(U,\psi,\overline{\psi})} \tag{1.61}$$

where Z is the partition function defined as

$$Z = \int \mathcal{D}U\mathcal{D}\psi\mathcal{D}\overline{\psi}e^{-S(U,\psi,\overline{\psi})} \tag{1.62}$$

such that $\langle 0|1|0\rangle = 1$ and the integration measures are defined as

$$\mathcal{D}U = \prod_{\mu,n} dU_\mu(n), \quad \mathcal{D}\psi = \prod_n d\psi(n), \quad \mathcal{D}\overline{\psi} = \prod_n d\overline{\psi}(n) \tag{1.63}$$

i.e., $\mathcal{D}U$ is defined over every link in the lattice, and $\mathcal{D}\psi\mathcal{D}\overline{\psi}$ over every site.

The quark fields are Grassman variables and as such difficult to deal with computationally. Fortunately, for calculations of the hadron mass spectrum, one usually only need to solve the path integral for quark propagators $\langle\overline{\psi}(m)\psi(n)\rangle$, which are also known as the quark Greens funcion $G(m,n)$. The Grassman integrals can then be done analytically to give

$$\begin{aligned}\langle\overline{\psi}(m)\psi(n)\rangle = G(m,n) &= \frac{\int \mathcal{D}U\mathcal{D}\psi\mathcal{D}\overline{\psi}\,\overline{\psi}(m)\psi(n)e^{-S_{QCD}}}{\int \mathcal{D}U\mathcal{D}\psi\mathcal{D}\overline{\psi}e^{-S_{QCD}}} \\ &= \frac{\int \mathcal{D}U K_F^{-1}(n,m,U)detK_F(n,m,U)e^{-S_G}}{\int \mathcal{D}U detK_F(n,m,U)e^{-S_G}}\end{aligned} \tag{1.64}$$

In a computer simulation, the lattice necessarily has a finite number of links, hence eq (1.64) is a multi-dimensional finite integral. It can be solved using Monte Carlo integration with importance sampling where a gauge-configuration $U_{(i)}$ is generated (with a random $SU(3)$ matrix for each link $U_\mu(n)$) with weight $detK_F(n,m,U)e^{-S_G}$ and repeated until one has an ensemble of N_{conf} such configurations. Then the quark propagator is estimated by evaluating

$$G(n,m) = \frac{1}{N_{conf}} \sum_{i=1}^{N_{conf}} G(n,m;U_{(i)}) \tag{1.65}$$

where $G(n,m;U_{(i)})$ means the quark propagator between m and n evaluated on the i^{th} gauge configuration. This method proves to be extremely difficult in practice since the weight $detK_F(n,m,U)e^{-S_G}$ is a non-local quantity and is too costly to calculate on most present computers. One way to overcome this problem is simply to set $detK_F(n,m,U)$ equal to unity. This defines the quenched approximation, which is used in most lattice calculations. The meaning of setting $detK_F(n,m,U) = 1$ is equivalent to ignoring internal quark loops in perturbative QCD.

Chapter 2

Potential Models

Since the discovery of the charm quark, potential models have been used with some success to study the heavy meson spectrum of charmonium and more recently bottomium. In the following chapter a simple introduction to such potential models in the continuum is given and results of the Υ D-state spectrum are presented.

2.1 Introduction to Potential Models

Bound states can be treated with the help of the (non-relativistic) Schrödinger equation

$$H\psi = E\psi \tag{2.1}$$

where the nonrelativistic Hamiltonian for a quantum system consisting of two particles with masses m_1 and m_2, respectively, which interact via some potential $V(r)$ is given in the centre of momentum frame by

$$H = m_1 + m_2 + \frac{\mathbf{p}^2}{2\mu} + V(r) \tag{2.2}$$

where μ denotes the reduced mass

$$\mu = \frac{m_1 m_2}{m_1 + m_2} \tag{2.3}$$

Here the main task is to find the potential $V(r)$ describing the interaction of the particles constituting the bound state. By considering the elastic scattering of the constituents, the perturbatively accessible part of the potential may be derived in the following way [5].

(i) compute the scattering amplitude T_{fi}, defined in terms of the S-matrix element S_{fi} by

$$\begin{aligned} S_{fi} &\equiv \langle f, out | i, in \rangle \\ &= \delta_{fi} + i(2\pi)^4 \delta^{(4)}(p_f - p_i) T_{fi} \end{aligned} \tag{2.4}$$

in lowest non-trivial order in perturbation theory:

(ii) perform the non-relativistic limit $\mathbf{p} \to 0$; and

(iii) obtain the potential $V(r)$ as the Fourier transform of the scattering amplitude T_{fi}

$$V(r) = -(2\pi)^3 \int d^3\mathbf{k} e^{-i\mathbf{k}\cdot\mathbf{r}} T_{fi}(\mathbf{k}) \tag{2.5}$$

A simple illustration of the above prescription goes as follows. The relevant situation for the determination of the quark potential which describes the forces acting within mesons is the quark-antiquark scattering

$$q_i(p_1, \sigma_1) + \overline{q}_j(p_2, \sigma_2) - \to q_k(q_1, \tau_1) + \overline{q}_l(q_2, \tau_2) \tag{2.6}$$

where $i, j, \ldots = 1, 2, 3$ label the colour indices (see figure (2.1)). Remembering that the quarks in the meson are in a colour-singlet state and introducing the meson colour wavefunctions $(1/\sqrt{3})\delta_{ij}$, we find from fig. (2.1) for the corresponding T-matrix element

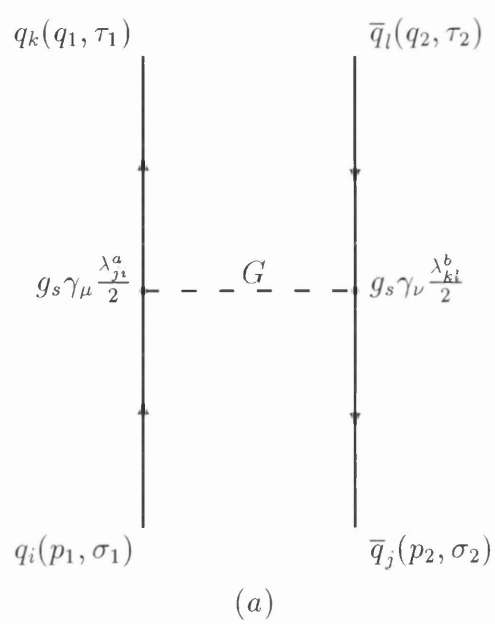

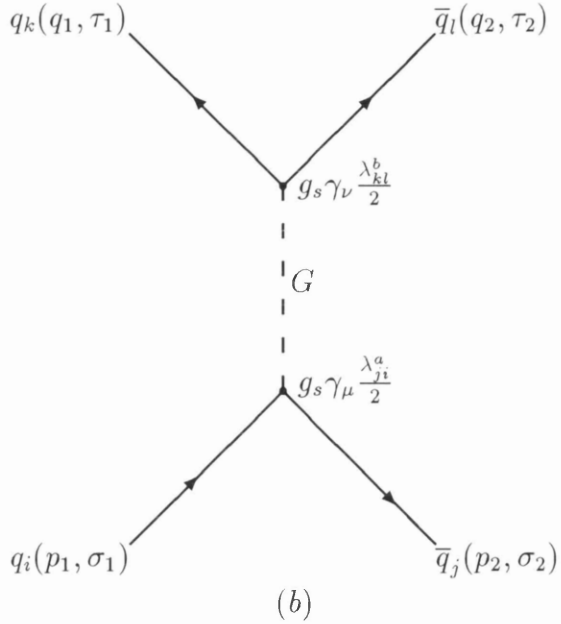

Figure 2.1: (a) quark-antiquark scattering, one-gluon exchange graph (b) quark-antiquark scattering, pair annihilation graph

$$
\begin{aligned}
T_{fi} &= -\frac{1}{(2\pi)^6}\frac{m^2}{(E_{p_1}E_{p_2}E_{q_1}E_{q_2})^{1/2}}g_s^2\frac{\delta_{ij}}{\sqrt{3}}\frac{\delta_{kl}}{\sqrt{3}} \\
&\times\left\{\frac{1}{(p_1-q_1)^2}\frac{\lambda^a_{ki}}{2}\frac{\lambda^a_{jl}}{2}\overline{u}(q_1,\tau_1)\gamma_\mu u(p_1,\sigma_1)\overline{v}(p_2,\sigma_2)\gamma^\mu v(q_2,\tau_2)\right. \\
&\left.-\frac{1}{(p_1+p_2)^2}\frac{\lambda^a_{ji}}{2}\frac{\lambda^a_{kl}}{2}\overline{u}(q_1,\tau_1)\gamma_\mu v(q_2,\tau_2)\overline{v}(p_2,\sigma_2)\gamma^\mu u(p_1,\sigma_1)\right\}. \quad (2.7)
\end{aligned}
$$

The contribution of the one-gluon exchange graph (2.1a) to the scattering amplitude T_{fi} reads

$$
t_{exch} = -\frac{g_s^2}{k^2}\frac{1}{\sqrt{3}}\delta_{ij}\frac{1}{\sqrt{3}}\delta_{kl}\frac{\lambda^a_{ki}}{2}\frac{\lambda^a_{jl}}{2}\overline{u}(q_1,\tau_1)\gamma_\mu u(p_1,\sigma_1)\overline{v}(p_2,\sigma_2)\gamma^\mu v(q_2,\tau_2) \quad (2.8)
$$

where k denotes the momentum transfer $k = p_1 - q_1 = p_2 - q_2$. The colour graph factor stemming from the exchange graph yields

$$
\begin{aligned}
&\frac{1}{\sqrt{3}}\sum_{i,j=1}^{3}\delta_{ij}\frac{1}{\sqrt{3}}\sum_{k,l=1}^{3}\delta_{kl}\times\sum_{a=1}^{8}\frac{\lambda^a_{ki}}{2}\frac{\lambda^a_{jl}}{2} \\
&= \frac{1}{12}\sum_{l,k}^{3}\sum_{a=1}^{8}\lambda^a_{ki}\lambda^a_{ik}
\end{aligned}
$$

$$= \frac{1}{12}\sum_{a=1}^{8} Tr[(\lambda^a)^2] = \frac{4}{3} \tag{2.9}$$

Hence the one-gluon exchange contribution t_{exch} to the scattering amplitude T_{fi} reduces in the nonrelativistic limit to

$$t_{exch} = \frac{4}{3}\frac{g_s^2}{k^2}\delta_{\tau_1\sigma_1}\delta_{\tau_2\sigma_2} \tag{2.10}$$

whereas the colour factor corresponding to the annihilation graph (2.1b) vanishes,

$$\frac{1}{\sqrt{3}}\delta_{ij}\frac{\lambda^a_{ji}}{2} = \frac{1}{2\sqrt{3}}Tr(\lambda^a) = 0 \tag{2.11}$$

Hence to lowest order in perturbation theory, the T-matrix element T_{fi} for quark-antiquark scattering reduces in the non-relativistic limit to

$$T_{fi}\frac{1}{(2\pi)^6}t = \frac{1}{(2\pi)^6}\frac{4}{3}\frac{g_s^2}{\mathbf{k}^2} \tag{2.12}$$

Consequently, one-gluon exchange in mesons leads to a Coulomb-like potential of the form

$$V_{NR}(r) = -\frac{4}{3}\frac{\alpha_s}{r}, \qquad \text{with} \qquad \alpha_s \equiv \frac{g_s^2}{4\pi} \tag{2.13}$$

2.2 The Spin Structure of the Quark Interaction

Colour confinement is described by a long-range part of the potential, which, unfortunately, is of non-perturbative origin. However, it is still useful to investigate the most general spin structure for the quark-antiquark interaction. Allowing in the scattering amplitude for an arbitrary kernal $K(k^2)$, $k = p_1 - q_1$, previously given by

$$K(k^2) = -\frac{4}{3}\frac{g_s^2}{k^2} \tag{2.14}$$

and generalising the spin structure $\gamma_\mu \otimes \gamma^\mu$ arising from vector-boson exchange to an arbitrary spin structure $\Gamma \otimes \Gamma$, the most general ansatz for the T-matrix element for quark-antiquark scattering is

Lorentz Structure	$\Gamma \otimes \Gamma$	Static Potential
Scalar	$1 \otimes 1$	$V_S(\mathbf{r})$
Pseudoscalar	$\gamma_5 \otimes \gamma^5$	0
Vector	$\gamma_\mu \otimes \gamma^\mu$	$V_V(\mathbf{r})$
Axial vector	$\gamma_\mu\gamma_5 \otimes \gamma^\mu\gamma^5$	$4\mathbf{S_1} \cdot \mathbf{S_2} V_A(\mathbf{r})$
Tensor	$1/2\sigma_{\mu\nu} \otimes \sigma^{\mu\nu}$	$4\mathbf{S_1} \cdot \mathbf{S_2} V_A(\mathbf{r})$

Table 2.1: Nonrelativistic interaction potential VNR arising from the various conceivable Lorentz structures $\Gamma \otimes \Gamma$ of an arbitrary fermion-antifermion interaction

$$T_{fi} = \frac{1}{(2\pi)^6} \frac{m^2}{(E_{p_1} E_{p_2} E_{q_1} E_{q_2})^{1/2}} \overline{u}(q_1)\Gamma u(p_1) K(k^2) \bar{(}p_2)\Gamma v(q_2) \tag{2.15}$$

where the possible spin structures $\Gamma \otimes \Gamma$ are shown in table (2.1)
where $\gamma_5 = \gamma^5 \equiv -i\gamma^0\gamma^1\gamma^2\gamma^3$ and $\sigma_{\mu\nu} \equiv \frac{i}{2}[\gamma_\mu, \gamma_\nu]$. Table (2.1) also shows the nonrelativistic potentials V_{NR} arising from the nonrelativistic reduction of the different Lorentz structures [6], where

$$V_S(r) = \frac{1}{(2\pi)^3} \int d^3\mathbf{k} e^{-i\mathbf{k}\cdot\mathbf{r}} K_S(-\mathbf{k^2}) \tag{2.16}$$

$$V_V(r) = \frac{-1}{(2\pi)^3} \int d^3\mathbf{k} e^{-i\mathbf{k}\cdot\mathbf{r}} K_V(-\mathbf{k^2}) \tag{2.17}$$

and $\mathbf{S_1}$, $\mathbf{S_2}$ denotes the spins of the fermions involved, $S_1 = S_2 = 1/2$. The results of the table can be summarised as follows:

- Both scalar and vector Lorentz structures lead to pure potential terms
- The contribution of the pseudoscalar Lorentz structure vanishes.
- Both axial vector and tensor Lorentz structures contribute only to the spin spin interaction term.

Depending on the total spin $\mathbf{S} = \mathbf{S_1} + \mathbf{S_2}$, the quantum number S may accept precisely either of two values:

- $S = 0$, which corresponds to some spin singlet like the η_c in the charmonium system.
- $S = 1$, which corresponds to some triplet, like the J/ψ in the charmonium system or the Υ in the bottomium system.

Accordingly, the expectation values $\langle \mathbf{S_1} \cdot \mathbf{S_2} \rangle$ of the product of the spins $\mathbf{S_1}$, $\mathbf{S_2}$ of the bound-state constituents are given by

$$\langle \mathbf{S_1} \cdot \mathbf{S_2} \rangle = \begin{cases} -3/4 & \text{for spin singlets } S{=}0 \\ +1/4 & \text{for spin triplets } S{=}1 \end{cases} \tag{2.18}$$

The empirically observed hadron spectrum also provides restrictions on the allowed effective quark antiquark interaction. For example the existence of both pseudoscalar mesons (like π, η and η') and vector mesons (like ρ, ω and ϕ) all of which are bound states of a quark and antiquark pair implies that the actual quark antiquark forces must be described by an interaction potential which yields binding for $S = 0$ as well as $S = 1$. This fact rules out both the axial vector and tensor Lorentz structures as the predominant contribution to any realistic quark antiquark interaction potential. Put another way, the theoretically predicted particle spectra would look very different from the experimentally measured ones if the dominant terms in the quark antiquark potential were anything other than some linear combination of vector and scalar Lorentz structure. Therefore, in conclusion the static interaction potential $V_{NR}(r)$ must be given by

$$V_{NR}(r) = V_V(r) + V_S(r) \tag{2.19}$$

2.3 Generalised Breit-Fermi Hamiltonian

The next step in studying nonrelativistic potentials is the improvement to the Hamiltonian (2.2) by taking into account relativistic corrections. We are mainly

interested in the spin-dependent interactions, which induce the fine and hyperfine splitting of the bound-state mass spectra. The spin-independent interactions are detailed in [7]. The Hamiltonian containing all spin-dependent relativistic corrections up to order

$$\frac{v^2}{c^2} = \frac{\mathbf{p}^2 c^2}{E^2} \simeq \frac{\mathbf{p}^2}{m^2 c^2} \tag{2.20}$$

is called the generalised Breit-Fermi Hamiltonian

$$H = m_1 + m_2 + \frac{\mathbf{p}^2}{2\mu} - \frac{1}{8}\left(\frac{1}{m_1^3} + \frac{1}{m_2^3}\right)\mathbf{P}^4 + V_{NR}(r) + H_{LS} + H_{SS} + H_T \tag{2.21}$$

and according to the analysis of section (2.4.1) - the static potential $V_{NR}(r)$ consists of a vector and a scalar contribution

$$V_{NR}(r) = V_S(r) + V_V(r) \tag{2.22}$$

The corresponding spin-dependent relativistic corrections read for equal masses $m_1 = m_2 = m$:

- spin-orbit term:

$$H_{LS} = \frac{1}{2m^2 r}\left(3\frac{d}{dr}V_V(r) - \frac{d}{dr}V_S(r)\right)\mathbf{L}\cdot\mathbf{S} \tag{2.23}$$

where $\mathbf{S} = \mathbf{S_1} + \mathbf{S_2}$ is the total spin of the bound state and $\mathbf{L} = \mathbf{r} \times \mathbf{p}$ the relative orbital angular momentum of its constituents;

- spin-spin term:

$$H_{SS} = \frac{2}{3m^2}\mathbf{S_1}\cdot\mathbf{S_2}\boldsymbol{\nabla}^2 V_V(r) \tag{2.24}$$

- tensor term:

$$H_T = \frac{1}{m^2}\left(\frac{1}{r}\frac{d}{dr}V_V(r) - \frac{d^2}{dr^2}V_V(r)\right)\left(\frac{(\mathbf{S_1}\cdot\mathbf{r})(\mathbf{S_2}\cdot\mathbf{r})}{\mathbf{r}^2} - \frac{1}{3}\mathbf{S_1}\cdot\mathbf{S_2}\right)$$
$$= \frac{1}{12m^2}\left(\frac{1}{r}\frac{d}{dr}V_V(r) - \frac{d^2}{dr^2}V_V(r)\right)S_{12} \qquad (2.25)$$

with the abbreviation

$$S_{12} = 12\left(\frac{(\mathbf{S_1}\cdot\mathbf{r})(\mathbf{S_2}\cdot\mathbf{r})}{\mathbf{r}^2} - \frac{1}{3}\mathbf{S_1}\cdot\mathbf{S_2}\right) \qquad (2.26)$$

Expectation values of the operators V_{LS}, V_{SS} and V_T can be obtained for appropriate states. To do this, it is necessary to calculate the expectation values of the operators $\mathbf{L}\cdot\mathbf{S}$, $\mathbf{S_1}\cdot\mathbf{S_2}$ and S_{12}. If S, L and J are the eigenvalues of the total spin $\mathbf{S}$, orbital angular momentum $\mathbf{L}$ and total angular momentum $\mathbf{J}$. It is easily shown that

$$\langle\mathbf{L}\cdot\mathbf{S}\rangle = \frac{1}{2}[J(J+1) - L(L+1) - S(S+1)] \qquad (2.27)$$

$$\langle\mathbf{S_1}\cdot\mathbf{S_2}\rangle = \frac{1}{2}[S(S+1) - S_1(S_1+1) - S_2(S_2+1)] \qquad (2.28)$$

The derivation of the expectation value of the tensor $\langle S_{12}\rangle$ is non-trivial [8] and is given by

$$\langle S_{12}\rangle = \frac{4}{(2L+3)(2L-1)}[S(S+1)L(L+1) - \frac{3}{2}\langle\mathbf{L}\cdot\mathbf{S}\rangle - 3\langle\mathbf{L}\cdot\mathbf{S}\rangle^2)] \qquad (2.29)$$

It can now be seen that if a state has either $L = 0$ or $S = 0$, there will be no spin-orbit V_{LS}, or tensor V_T, contributions to the potential. Table (2.2) gives the eigenvalues of the operators (2.27) to (2.29) for S, P and D states represented by the spectroscopic notation $^{2S+1}L_J$.

2.4 The Funnel Potential

According to the analysis of section (2.2), the quark-antiquark potential $V_{NR}(r)$ is of vector and/or scalar type. For short distances, the potential (resulting from

	state									
operator	$^1S_0$	$^3S_1$	$^1P_1$	$^3P_0$	$^3P_1$	$^3P_2$	$^1D_2$	$^3D_1$	$^3D_2$	$^3D_3$
$\langle \mathbf{L} \cdot \mathbf{S} \rangle$	0	0	0	-2	-1	1	0	-3	-1	2
$\langle \mathbf{S_1} \cdot \mathbf{S_2} \rangle$	$-\frac{3}{4}$	$\frac{1}{4}$	$-\frac{3}{4}$	$\frac{1}{4}$	$\frac{1}{4}$	$\frac{1}{4}$	$-\frac{3}{4}$	$\frac{1}{4}$	$\frac{1}{4}$	$\frac{1}{4}$
$\langle S_{12} \rangle$	0	0	0	-4	2	$-\frac{2}{5}$	0	-2	2	$-\frac{4}{7}$

Table 2.2: Eigenvalues of the spin-orbit, spin-spin and tensor operators for various states given by their spectroscopic notation.

one-gluon exchange) is essentially Coulomb like

$$V_{exchange}(r) = -\frac{4}{3}\frac{\alpha_s}{r} \tag{2.30}$$

For large distances, there has to exist a contribution $V_{conf}(r)$ in order to describe colour confinement, $V_{conf}(r) = ar^n$ with $n > 0$, implying that for large r the binding force must not decrease faster than $1/r$. From the mesonic mass spectrum the exponent n is in the vicinity of $n \simeq 1$. Moreover lattice gauge theories also find that $V_{conf}(r)$ is roughly proportional to r. Consequently, a linear potential $V_{conf}(r) = ar$ is a sensible choice for $V_{conf}(r)$. The funnel (or Cornell) Potential is given by

$$V_{NR}(r) = -\frac{4}{3}\frac{\alpha_s}{r} + ar \tag{2.31}$$

and despite its simplicity, it was the first model [9] to be able to reproduce the charmonium spectrum quite well. In a strict sense the momentum dependence of the strong coupling constant $\alpha_s(Q^2)$ has to be taken into account, thereby modifying the Coulomb-like behaviour of the first term in (2.31).

2.4.1 Spin Structure of the Funnel Potential

In order to decide whether the spin structure of the potential (2.31) is a pure vector, a pure scalar or a mixing of both, we consider the P-wave spin splitting

	Meson	
Level	$c\bar{c}$	$b\bar{b}$
$^3P_2$	3.5563	9.9132
$^3P_1$	3.5106	9.8919
$^3P_0$	3.4151	9.8598
ρ	0.479	0.664

Table 2.3: Masses (in GeV) and the ratio ρ for P states of $c\bar{c}$ and $b\bar{b}$

of charmonium and bottomium, that is the ratio [10].

$$\rho = \frac{M(^3P_2) - M(^3P_1)}{M(^3P_1) - M(^3P_0)} \tag{2.32}$$

From table (2.3) the experimental average for ρ is $\rho_{exp} \simeq 0.6$.

With the help of the generalised Breit-Fermi Hamiltonian (2.21), we can compute the ratio ρ for the potential (2.31) perturbatively. Since the spin-spin interaction H_{SS} does not depend on the total angular momentum, its contribution cancels in a perturbative evaluation of ρ. Accordingly ρ is determined by the contributions of the spin-orbit term H_{LS} and the tensor term H_T only:

$$\rho = \frac{\langle ^3P_2|H_{LS} + H_T|^3P_2\rangle - \langle ^3P_1|H_{LS} + H_T|^3P_1\rangle}{\langle ^3P_1|H_{LS} + H_T|^3P_1\rangle - \langle ^3P_0|H_{LS} + H_T|^3P_0\rangle} \tag{2.33}$$

From table (2.2) we find for $\langle \mathbf{L}\cdot\mathbf{S}\rangle$ and $\langle S_{12}\rangle$

$$\langle \mathbf{L}\cdot\mathbf{S}\rangle = \begin{cases} +1 \\ -1 \\ -2 \end{cases} \qquad \langle S_{12}\rangle = \begin{cases} -2/5 & \text{for } ^3P_2 \\ +2 & ^3P_1 \\ -4 & ^3P_0 \end{cases} \tag{2.34}$$

For a pure vector $V_V = V$, V_S=0, one obtains

$$\rho = \frac{1}{5}\frac{8\alpha_S\langle r^{-3}\rangle + 7a\langle r^{-1}\rangle}{2\alpha_S\langle r^{-3}\rangle + a\langle r^{-1}\rangle} \tag{2.35}$$

which gives the bounds $4/5 \leq \rho \leq 7/5$ corresponding to $a = 0$ or $\alpha_S = 0$, respectively, in clear conflict with the experimental value $\rho_{exp} \simeq 0.6$. A pure scalar,

$V_S = V$, $V_V = 0$ leads to $\rho = 2$, which is also not tolerable from an experimental point of view. In the case of vector/scalar mixing where it is assumed that $V_V = -4\alpha_S/3r$ and $V_S = ar$, results in

$$\rho = \frac{1}{5}\frac{8\alpha_S\langle r^{-3}\rangle + 5/2a\langle r^{-1}\rangle}{2\alpha_S\langle r^{-3}\rangle + 1/4a\langle r^{-1}\rangle} \tag{2.36}$$

which implies $\rho \leq 4/5$, if the Coloumb part dominates and $\rho \geq 2$ if the linear part dominates. We arrive at the conclusion that the funnel potential (2.31) is a linear combination of a vector and a scalar part, $V_{NR}(r) = V_V(r) + V_S(r)$, where the Coulomb part V_{exch} is of vector type and the linear part V_{conf} is of scalar type. In this form the funnel potential represents the genuine prototype of all QCD potential models proposed for the description of hadrons as bound states of quarks [5].

2.5 Results from Potential Models

So far no D-states for the Υ system have been observed experimentally, however various predictions of the D-state spectrum have been made [11, 12], with the studies of potential models. These phenomenological studies of quarkonia have led to a satisfactory picture of the interquark force [14]. A central potential $V_{NR}(r)$ appears to interpolate between short-distance Coloumbic and long-distance linear behaviour. Following the work of [11], a short review of the predictions for the D-state spectrum will be given here. It was shown in that work that existing bound-state information can be used to reproduce an interquark potential in the range of distances where the bound-state wave functions have appreciable values, using the method of inverse scattering [15]. This method was originally used to construct a potential on the basis of the Υ data on $^3S_1$ bound states; the potential was then used to satisfactorily predict the positions of the P-state levels, which were borne out by experiment.

Briefly the inverse scattering method makes use of the equation

$$\Gamma(^3S_1 \rightarrow e^+e^-) = \frac{4\alpha^2 e_Q^2}{[M(n^3S_1)]^2}|\psi_n(0)|^2 A^{-1} \tag{2.37}$$

where

$$A^{-1} = 1 - \frac{16\alpha_s}{3\pi} \tag{2.38}$$

is a QCD correction. The annihilation decay of the Υ states n^3S_1 into an e^+e^- pair has been observed experimentally [14] and the leptonic width Γ has been measured along with the mass for each level. By inserting these experimental values into (2.37) it is possible to calculate $|\psi_n(0)|^2$ for each of the lowest n^3S_1 Υ levels. An interquark potential $V_{NR}(r)$ can then be constructed [15] for $b\bar{b}$ by solving a Schrödinger equation of the form

$$\left[-\frac{1}{2\mu}\frac{d^2}{dr^2} + V(r)\right]\psi_n(r) = E_n\psi(r) \tag{2.39}$$

A summary of the experimental Υ data used to construct a $b\bar{b}$ potential via the inverse scattering method is given in table (2.4).

Level	Mass (GeV)	Γ_{ee}(KeV)
$\Upsilon(1^3S1)$	9.4604(2)	1.216(27)
$\Upsilon(2^3S_1)$	10.0233(3)	0.553(23)
$\Upsilon(3^3S_1)$	10.3553(5)	0.402(31)
$\Upsilon(4^3S_1)$	10.5800(35)	0.248(31)

Table 2.4: Experimental parameters of Υ levels used to construct an interquark potential

The parameter A in (2.37) is expected to be approximately $A \simeq 1.44$ using $\alpha_s(m_b) \simeq 0.18$ (a value found in the analysis of quarkonium decays [11]). However A and E_0 (from the Schrödinger equation) are left as free parameters such that they can be adjusted to obtain the most accurate predictions of the spin averaged centre of mass levels of $\langle 1P\rangle$ and $\langle 2P\rangle$.

Using the potential constructed from S-state levels, it is possible to solve the Schrödinger equation to obtain the centre of mass P-state and D-state levels. Two different sets of results are shown in table (2.5), for the b-quark mass; m_b =4.5 GeV with A =1.3 and m_b =4.9 GeV with A =1.5. The predictions are nearly indistinguishable from one another.

m_b(GeV)	4.5	4.9	Experimental
a	1.3	1.5	
$1P$	9.9026	9.9031	9.9002
$2P$	10.2584	10.2589	10.2601
$3P$	10.5197	10.5201	
$1D$	10.1562	10.1567	
$2D$	10.4408	10.4412	

Table 2.5: Spin averaged centre of mass P state and D states obtained from a potential constructed from S state parameters

As can be seen from the table, the P-state predictions are very close to the experimental results. In accordance with other potential models [11], A and m_b are chosen to be A =1.5 and m_b =4.9 GeV. The resulting potential can be found in [14].

The fine structure of the triplet D-state levels can be obtained from the centre of mass levels quoted in table (2.5) from the general expression for terms contributing to fine structure in $Q\overline{Q}$ systems

$$V_{FS}(r) = V_{LS}(r) + V_T(r) \tag{2.40}$$

where the terms $V_{LS}(r)$ and $V_T(r)$ are the spin-orbit and tensor contributions (2.23) and (2.25) to the Breit-Fermi Hamiltonian described in section (2.3). These spin-dependent terms resolve the degeneracy in the triplet P or D-state levels such that

$$M(^3L_J) = \overline{M}(^3L) + a\langle \mathbf{L}\cdot\mathbf{S}\rangle + b\langle S_{12}\rangle \tag{2.41}$$

with

$$a = (4\alpha_s\langle r^{-3}\rangle - k\langle r^{-1}\rangle)/2m_Q \tag{2.42}$$

$$b = \alpha_s\langle r^{-3}\rangle/3m_Q^2 \tag{2.43}$$

where $\overline{M}$ is the mass of the spin averaged centre of mass level for the P or D-states. The values of $\langle r^{-1}\rangle$ and $\langle r^{-3}\rangle$ were evaluated for 1D and 2D [11] and are shown in table (2.7). The values of α_s and k can be estimated by calculating a and b for each of the 1^3P_J and 2^3P_J masses M_J, which are known from experiment. These masses are shown in table (2.6).

Level	Mass (GeV)
$\chi_b(1^3P_0)$	9.8598(13)
$\chi_b(1^3P_1)$	9.8919(7)
$\chi_b(1^3P_2)$	9.9133(6)
$\chi_b(2^3P_0)$	10.2321(6)
$\chi_b(2^3P_1)$	10.2552(5)
$\chi_b(2^3P_2)$	10.2685(4)

Table 2.6: Experimental values of Υ levels used to construct an interquark potential

Using the masses from the above table, a and b are calculated by rearranging equation (2.41) to obtain

$$\begin{aligned} a &= (-2M_0 - 3M_1 + 5M_2)/12 \\ b &= 5(-2M_0 + 3M_1 - M_2)/72 \end{aligned} \tag{2.44}$$

Level	$\langle r^{-1} \rangle$ (GeV)	$\langle r^{-3} \rangle$ (GeV^3)	a (MeV)	b (MeV)
$1P$	0.635	0.550	14.27	2.97
$2P$	0.445	0.394	10.35	2.04
$3P$	0.316	0.261	6.90	1.41
$1D$	0.430	0.120	1.78	0.65
$2D$	0.340	0.105	1.71	0.56

Table 2.7: Parameters governing fine structure in $b\bar{b}$ levels.

The values of a and b for 1P and 2P are shown in table (2.7), and as stated above may be used to determine the independent parameters α_s/m_b^2 and $k/2m_b^2$ in (2.42) and (2.43). An average of determinations from the centre of mass 1P and 2P levels yields

$$\alpha_s/m_b^2 = 0.016 \quad \text{GeV}^{-2} \tag{2.45}$$

$$k/2m_b^2 = 0.0049 \tag{2.46}$$

With the help of the values of $\langle r^{-1} \rangle$ and $\langle r^{-3} \rangle$ listed in table (2.7), the values of a and b for 3P, 1D and 2D can be calculated and are also listed in table (2.7). It is now possible to predict the spectrum for triplet D-states of Υ using equation (2.41) and the parameters quoted in table (2.7). The predicted values are shown below in table (2.8).

The left hand column in table (2.8) lists the predictions of the potential model reviewed in this section [11], while the centre and right hand columns show the predictions obtained from other potential models used to predict the D-state masses, [12, 13] respectively. Note that for potential models it is expected that the spin averaged centre of mass of the triplet D states $\langle D \rangle$ will be at the same point as the singlet state $^1D_2$ [16].

From table (2.8) it can be seen that there is an enormous disparity in

State	Model reviewed	[12]	[13]
1^3D_1	10.150	10.153	10.120
1^3D_2	10.156	10.163	10.126
1^3D_3	10.160	10.174	10.130
$\langle 1D \rangle \simeq 1^1D_2$	10.157	10.166	10.127
2^3D_1	10.435	10.444	
2^3D_2	10.441	10.452	
2^3D_3	10.444	10.462	
$\langle 2D \rangle \simeq 2^1D_2$	10.441	10.455	

Table 2.8: Comparison of predictions for masses of $\Upsilon(1D)$ and $\Upsilon(2D)$ levels, in GeV.

the different spin splittings between the different potential model calculations. From the comparison of the predictions obtained using the model reviewed for this thesis with those of [12] there is a general agreement to within ± 10 MeV. However it is not the size of the splittings but the changes that are important, e.g. the model of [12] has splittings twice as large as the model reviewed [11]. The final column in the table shows the results of a more recent study [13], which predicts much lower masses for the D states than the two earlier models, but the changes in the splittings are in complete agreement with those of the model reviewed.

The differences between the predictions of the first two models in table (2.8) points clearly to problems with the potential model approach, which seems to be rather poor at obtaining spin splittings because these depend on details of the potential that are not really known.

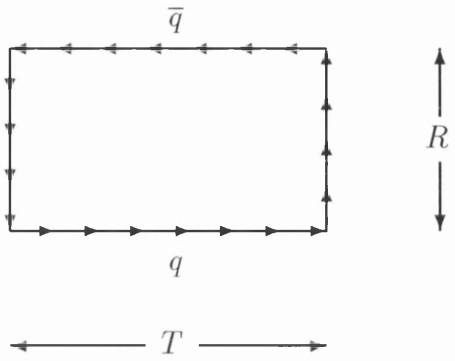

Figure 2.2: An example of a Wilson Loop

2.6 Potentials Studied on the Lattice

Alternatively the potential $V(r)$ can be extracted from first principles using the techniques of lattice QCD. In the limit $m_Q \rightarrow \infty$, the heavy quark becomes static. In space-time its world line becomes a line of QCD gauge fields in the time direction. As described in Chapter 1, for lattice QCD we break up space-time into a lattice of points and represent the gauge fields by $SU(3)$ colour matrices, U. The static quark propagator then becomes a string of U matrices. We can put a quark and antiquark together and join them up into a closed, and therefore gauge invariant loop, called a Wilson loop (see figure 2.2).

The value of the Wilson loop can be calculated on sets of gauge fields $\{U\}$ where a gauge field is defined on every link of the lattice. These sets $\{U\}$ are called configurations. The physical quantity of interest here is the matrix element of the Wilson loop between vacuum states and can be found by averaging values of the Wilson loop over an ensemble of configurations [16]. The heavy quark potential $V(r)$ is related to the expectation value over such an ensemble of gauge fields of a Wilson loop of spatial size R [2, 16]. The matrix element of the Wilson loop becomes exponentially related to the ground state energy of the quark-antiquark pair as the time T direction of the Wilson loop, W, tends to infinity.

$$\langle W(R,T)\rangle \stackrel{T\to\infty}{\longrightarrow} |\langle\psi(o)\chi(R)|0\rangle|^2 e^{-E(R)T} + \text{Higher order terms} \tag{2.47}$$

$|\langle\psi(o)\chi(R)|0\rangle|^2$ is the amplitude for transition between the vacuum and the state with two static sources separated by R. Since the quarks have no kinetic energy, $E(R)$ is the dimensionless lattice heavy quark potential $V_{latt}(R)$. Unfortunately as well as the real long range potential this contains an ultraviolet divergent self-energy term which comes from gluon loops sitting around the perimeter of the Wilson loop and so contributes, for large $T >> R$, a constant piece V_c to $V_{latt}(R)$ which is dependent on β [16]. Consequently

$$E(R) = V_{latt}(R) = V(R) + V_c \tag{2.48}$$

Once the ensemble of gauge field configurations has been generated, Wilson loops of various sizes in R and T are measured and average values of $W(R,T)$ obtained. For a fixed R, $W(R,T)$ is fitted to the exponential function (2.47) for large T ($T \to \infty$), allowing E (which equals $V_{latt}(R)$) to be extracted. Moving away from the large T limit, higher order terms need to be included in the fit. These higher order terms contain exponentials of excited states of the potential. Once $V_{latt}(R)$ is obtained it can either be used directly or it can be fitted to a functional form of R, such that it can be compared with the continuum potential models. The functional form usually used, takes the form of the Cornell potential (2.31) with $e = 4\alpha_s/3$ and an additive constant, V_c:

$$V_{latt}(R) = \sigma R - \frac{e}{R} + V_c \tag{2.49}$$

The fit then yields the parameters σ, e and V_c. In general e is taken as a constant. Since V_{latt} and the separation R are in dimensionless lattice units, the lattice spacing a has to be used to obtain physical units of GeV. Thus the continuum potential V is found by

$$V(r = Ra) = V_{latt} \times a^{-1} \tag{2.50}$$

As mentioned above, V_c, is an unphysical constant, and must be removed before applying the expression (2.50). If V_c is not removed at this stage it will diverge on approach to the continuum limit $a \rightarrow 0$.

Most precision lattice calculations of the heavy quark potential have used the quenched approximation where recent calculations have given a value of e around 0.3 [17], which is smaller than the typical values that phenomenological potentials have used, for example e =0.54 in [12]. This difference in values for e is partly due to the quenched approximation, where no light $q\overline{q}$ pairs are available for screening. This means the strong coupling α_s will run to zero too fast at small distances, hence

$$\begin{aligned} \alpha_s(r)_{Q.A.} &< \alpha_s(r)_{full\ theory} \\ V(r)_{Q.A.} &> V(r)_{full\ theory} \end{aligned}$$

when $V(r)$ is dominated by the Coloumb term.

Finally it is appropriate to mention the string tension, σ, which describes the linearly rising part of the potential. Since it has physical dimensions, $\sigma = \sigma_{latt} \times a^{-2}$, values from phenomenological models can be used to fix the lattice spacing a and hence convert all other dimensionless quantities to physical units. However, the string tension σ and e appearing in the Cornell potential (2.49) are anti-correlated, and so an alternative method of fitting the lattice spacing a can be achieved using the physical quantity r_0 obtained by setting $r^2F(r)$ to a fixed value [16]. $F(r)$ is the interquark force, obtained by differentiating the potential (2.49). Once a value of a has been obtained, $V_{latt} - V_c$ can be converted into the physical heavy quark potential which should be independent of the lattice spacing at which the calculation was done. Figure (2.3) shows this is true for current lattice results [17].

The infinitely massive heavy quark is only a source of colour; it carries no spin. As discussed in section (2.3), in order to obtain spin-splittings it is necessary to incorporate spin-dependent potentials into a Schrödinger equation, $H\psi = E\psi$, and solve for the splittings.

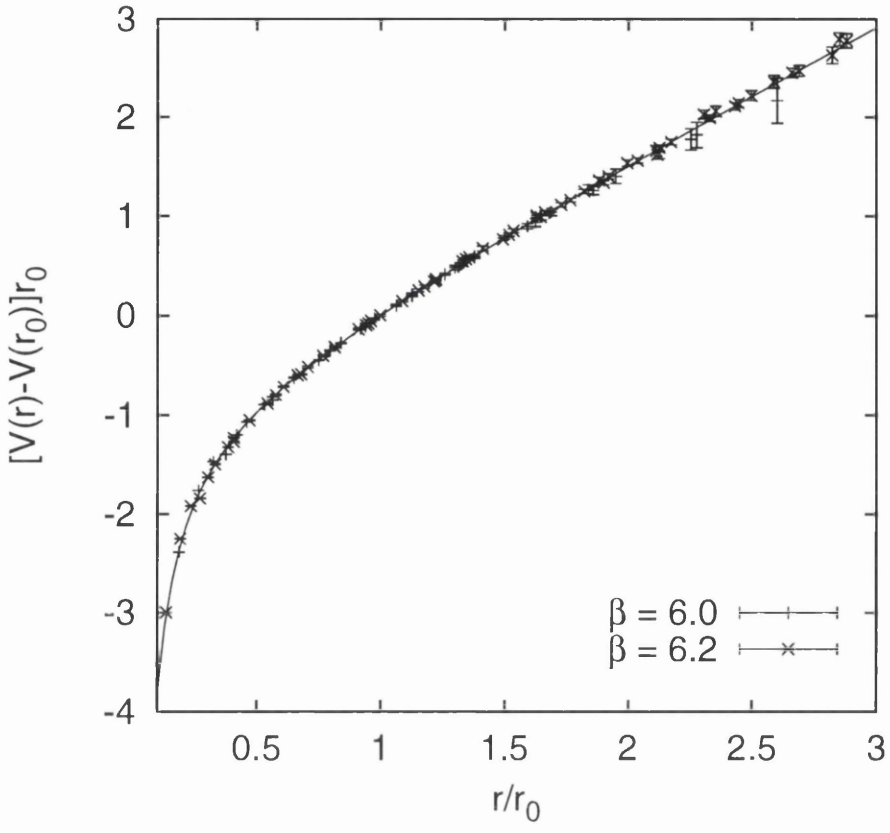

Figure 2.3: The heavy quark potential obtained from the lattice of two different values of the lattice spacing in the quenched approximation. The potential and separation are given in terms of the parameter r_0.

$$H = \sum_{i=1}^{2} \{ \frac{\mathbf{p}^2}{2m_i} - c_1 \frac{\mathbf{p}^4}{8m_i^3} \} + V_0(r) + V_{sd}(r, \mathbf{L}, \mathbf{S_1}, \mathbf{S_2}) \tag{2.51}$$

where V_0 is the central potential discusses in section (2.1) and V_{sd} includes the spin dependent potentials discussed in section (2.3). For heavy quarks of the same mass m_Q, the complete spin-dependent potential is given by

$$\begin{aligned} V_{SD}(r) &= \frac{1}{2m_Q^2 r} \mathbf{L} \cdot \mathbf{S} \left(V_0'(r) + 2V_1'(r) \right) \\ &+ \frac{1}{m_Q^2 r} \mathbf{L} \cdot \mathbf{S} V_2'(r) \end{aligned}$$

$$+ \quad \frac{1}{3m_Q^2}\left[3(\mathbf{S_1}\cdot\mathbf{r})(\mathbf{S_2}\cdot\mathbf{r}) - \mathbf{S_1}\cdot\mathbf{S_2}\right]V_3(r)$$

$$+ \quad \frac{2}{3m_Q^2}\mathbf{S_1}\cdot\mathbf{S_2}V_4(r) \tag{2.52}$$

These spin-dependent potentials can be extracted on the lattice by calculating the following expectation values [16, 17]:

$$\frac{R_k}{R}V_1'(R) = 2\epsilon_{ijk}\lim_{\tau\to\infty}\int_o^\tau dt\, t\Big\langle \boxed{\begin{matrix} E_j \bullet \\ \\ B_i \bullet \end{matrix}} \Big\rangle / Z_W \tag{2.53}$$

$$\frac{R_k}{R}V_2'(R) = \epsilon_{ijk}\lim_{\tau\to\infty}\int_o^\tau dt\, t\Big\langle \boxed{\begin{matrix} E_j \bullet \\ \\ \bullet B_i \end{matrix}} \Big\rangle / Z_W \tag{2.54}$$

$$[\hat{R}_i\hat{R}_j - \frac{1}{3}\delta_{ij}]V_3(R) + \frac{1}{3}\delta_{ij}V_4(R) = 2\lim_{\tau\to\infty}\int_o^\tau dt\Big\langle \boxed{\begin{matrix} B_j \bullet \\ \\ \bullet B_i \end{matrix}} \Big\rangle / Z_W \tag{2.55}$$

where the diagrams in the equations above represent Wilson loops with field insertions of E or B as required by each potential. The denominator Z_W is the expectation value of the Wilson loop without field insertions, as in figure (2.2).

Once the spin-dependent potentials are calculated using (2.53) to (2.55) they can be inserted into a Schrödinger equation and the energy shifts from the spin-independent states can be calculated [17]. Calculations using this method for studying spin-dependent potentials on the lattice have recently been carried out, and predictions have been made for the S-, P- and D-state spectrum of the Υ meson [17]. These predictions are shown in table (2.6) for different lattice spacings and where appropriate a comparison with experiment is made. The predictions for the masses in GeV for the P and D states are shown in table (2.6) for different lattice spacings. The first two columns give the results that were obtained using the quenched approximation, the third column shows unquenched results, while the last column displays a comparison with experiment where appropriate.

The quenched results at $\beta = 6.0$ and $\beta = 6.2$ are in agreement with each other but the spin splitting between these states are very small compared with

State	$\beta = 6.0$	$\beta = 6.2$	$e = 0.40$	experiment
1^1P_1	9.879	9.879	9.889	
1^3P_0	9.866	9.866	9.867	9.860
1^3P_1	9.878	9.878	9.886	9.892
1^3P_2	9.882	9.883	9.895	9.913
2^1P_1	10.238	10.238	10.243	
2^3P_0	10.226	10.225	10.223	10.232
2^3P_1	10.237	10.237	10.237	10.255
2^3P_2	10.241	10.242	10.249	10.269
1^1D_2	10.120	10.121	10.136	
1^3D_1	10.121	10.121	10.134	
1^3D_2	10.121	10.122	10.137	
1^3D_3	10.119	10.120	10.137	

Table 2.9: Shows predictions for the masses of various Υ states for quenched and unquenched results. The quenched results were carried out on different sizes of lattice. A comparison is made with experiment where appropriate.

the predictions of the continuum potential models discussed in the last section and seem to be in the wrong order. The unquenched predictions still give smaller splittings than the continuum results however this time the $^3D_3$ state has the highest mass while the $^3D_1$ state has the lowest mass which is in agreement with continuum results like [13] but the $^3D_2$ and $^1D_2$ states seem to be the wrong way round.

The problems outlined here arising from calculating the mass spectrum for Υ using a potential model on a lattice seem to be similar to the problems encountered with the continuum models of the previous section.

Chapter 3

Non-Relativistic QCD

3.1 Motivation for NRQCD

The advantage of studying heavy-quark mesons lies in the fact that the quarks can be treated in a non-relativistic way. From potential models it is possible to calculate the typical velocity of the bottom quark in the Υ meson as $v^2 \sim 0.1$ [16]. Low quark velocities have two important consequences. The first is the probability for finding low-energy gluons in the meson is small, since the amplitude for a quark to radiate a gluon is proportional to v, for example the probability for finding a $Q\overline{Q}g$ state in the meson is suppressed by $\mathcal{O}(v^2)$. The second is the quark-antiquark interaction is approximately instantaneous. A gluon exchanged by the quark and antiquark usually has momentum of order the quark momenta, making the gluon's energy larger than the quark kinetic energy by a factor of $1/v$: $E_g \sim P_g \sim Mv >> Mv^2$, where M is the quark mass. As a result, exchanged gluons have reaction times that are $1/v$ times shorter than the quark reaction time and can therefore be treated as instantaneous interactions. These two consequences suggest that we can model heavy quark mesons as $Q\overline{Q}$ bound states, interacting by instantaneous potentials. Indeed the phenomenological non-relativistic potential models examined in the last chapter have been very successful in describing much of the physics of the Υ and ψ systems. There are however disadvantages to their approach, since they are

only QCD inspired phenomenological models, and not calculations from first principles. So in order to improve the accuracy of their predictions often requires an increasing number of parameters which can make the models very complicated.

The approach of NRQCD [18, 19, 20, 21] allows first principles calculations and has several advantages over potential models in that it retains the quark dynamics, leading to a proper treatment of retardation effects. Therefore the appearance of hybrid states such as $Q\overline{Q}g$, whose components can be as large as $P(Q\overline{Q}g) \sim \mathcal{O}(v^2) \sim 10\%$ for the Υ meson and $Q\overline{Q}q\overline{q}$, where $q\overline{q}$ are a light quark/antiquark pair, are systematically accounted for. Another advantage of NRQCD is that it is formulated with only two parameters and the accuracy of its predictions can be improved relatively easily.

3.2 Energy Scales in NRQCD

In order to understand NRQCD it is important to realise that any study of non-relativistic systems presents a fundamental difficulty due to a wide range of important dynamical energy scales. These scales are the heavy quark mass $\sim M$, the quark's momentum $\sim Mv$ and the quark's kinetic energy $\sim Mv^2$. In order to see all three energy scales in a lattice simulation of Υ requires a lattice space-time grid that is large compared with $1/Mv^2$ so reducing finite volume errors and a lattice spacing that is small compared with $1/M$ thus reducing finite lattice spacing errors. To satisfy these conditions would require a space-time grid of $\sim 100^4$ which is beyond the reach of current computing power [18]. A way of avoiding this problem is to explicitly remove the largest scale, the mass M from the theory, since it plays only a minor role in the dynamics of a non-relativistic system. This is achieved by choosing a lattice spacing so as to exclude relativistic heavy-quark momenta from the theory, ie. setting the lattice spacing to $a \sim 1/M$ allowing a more realistic space-time grid of $\sim 20^4$ to be used.

One starting point for the derivation of NRQCD is to regularise the Dirac theory for quarks at non-relativistic energies by introducing an ultra-violet cut off $\Lambda \sim M$ so as to exclude relativistic momenta [18]. It is still possible for quarks

with average momentum Mv to fluctuate into relativistic states of value M but since this would occur for only short periods of time these relativistic intermediate states can be incorporated into the Lagrangian by adding local interactions in powers of $1/\Lambda$ with coefficients determined perturbatively. The resulting alterations to the Lagrangian leads to a modified theory, known as an effective field theory. Effective theories allow any desired accuracy $(p/\Lambda)^n$ to be attained by including all interactions up to order $1/\Lambda^n$ with the condition that the resulting couplings be determined by matching the modified theory to the full theory through order $(p/\Lambda)^n$. One way of modifying the Dirac theory in such a way is to apply a transformation known as a Foldy-Wouthuysen-Tani (FWT) transformation [22, 23, 24] which allows the Lagrangian to be expanded in powers of $1/M$, so that

$$\begin{aligned}\overline{\Psi}(\gamma^\mu D_\mu - M)\Psi \quad \rightarrow \quad & \psi^\dagger \left(iD_t - M + \frac{\mathbf{D^2}}{2M} \right) \psi \\ & + \psi^\dagger \left(\frac{\mathbf{D^4}}{8M^3} + \frac{g}{2M} \boldsymbol{\sigma} \cdot \mathbf{B} + \frac{g}{8M^3} \boldsymbol{\nabla} \cdot \mathbf{E} + \cdots \right) \psi \qquad (3.1) \\ & + \text{ antiquark terms } + \text{ quark-antiquark terms } + \cdots\end{aligned}$$

This transformation is a unitary transformation on the four component Dirac spinor Ψ which is decoupled such that the upper components form a 2-component Pauli spinor ψ describing the quark dynamics, while the lower components χ similarly describe the antiquark dynamics. Combining both the regularisation of the Dirac theory and the FWT transformation such that the cut off $\Lambda \sim M$, the FWT transformation (3.1) becomes an expansion in powers of $1/\Lambda$. Thus to obtain an accuracy of $(p/\Lambda^n) = v^n$, only terms up to and including the $\mathcal{O}(1/\Lambda^n)$ interactions need be retained in the Lagrangian. To summarise this section, NRQCD is an effective field theory which approximates ordinary relativistic QCD at low energies and in principle, the NRQCD action may be corrected to reproduce the exact results of QCD by including an infinite number of non-renormalisable interactions. Exact agreement with full QCD is unnecessary however since only a finite number of interactions are required to attain any accuracy desired in powers

of v. NRQCD has many advantages over the original Dirac theory; the quark field decouples from the antiquark field allowing quark propagators to be calculated separately, the fermion doubling problem of section (1.3.2) is completely avoided when dealing with non relativistic propagators on the lattice and the non relativistic propagators are much simpler and cost less to calculate than relativistic ones.

In the next section the work of [20] is followed to determine fundamentally which interactions to include in the corrected Lagrangian, using power counting methods.

3.3 Power Counting Rules for NRQCD

An estimation of the magnitude of the heavy quark field $\psi(x)$, or equivalently the antiquark field $\chi(x)$ can be made from the number operator for heavy quarks which is normalised to unity for a quarkonium meson

$$\int \mathbf{d^3x} \psi^\dagger(x)\psi(x) = 1 \tag{3.2}$$

From the uncertainty principle, the quark in the meson is localised within a region $\Delta x \sim 1/p$, therefore

$$\psi^\dagger(x)\psi(x) \sim p^3 \tag{3.3}$$

and so the quark field has a magnitude $\psi(x) \sim p^{3/2}$. The expectation value for the kinetic energy operator will be Mv^2 by definition

$$\int \mathbf{d^3x} \psi^\dagger(x) \frac{\mathbf{D^2}}{2M} \psi(x) \sim Mv^2 \tag{3.4}$$

and so the spatial covariant derivative acting on a quark field will be $\mathbf{D} \sim p$.

Field equations can be used to relate estimates for different operators. For example, the lowest-order FWT transformation applied to the Dirac theory gives a quark Lagrangian whose leading terms are those of a Schrödinger theory:

$$\mathcal{L} = \psi^\dagger(x)\left(iD_t + \frac{D^2}{2M}\right)\psi(x) - \frac{1}{4}F_{\mu\nu}(x)F^{\mu\nu}(x) \tag{3.5}$$

where the mass term M has been explicitly removed from the Lagrangian and can be added in later as a constant shift. The corresponding lowest-order field equation for the quark field is given by

$$\left(iD_t + \frac{D^2}{2M}\right)\psi(x) = 0 \tag{3.6}$$

implying that the temporal covariant derivative D_t has magnitude $\sim Mv^2$. For non-relativistic systems the most natural choice of gauge is the Coulomb gauge, in which the vector potential $\mathbf{A}$ is small and can be neglected. In this gauge the above equation becomes

$$\left(i\partial_t - g\phi(x) + \frac{\boldsymbol{\nabla}^2}{2M}\right)\psi(x) \simeq 0 \tag{3.7}$$

The potential energy that balances the kinetic energy and produces a bound state enters through the potential energy operator $g\phi(x)$ and consequently

$$g\phi(x) \sim Mv^2 \tag{3.8}$$

To estimate the magnitude of the vector potential $\mathbf{A}(x)$, the Euler-Lagrange equation

$$\frac{\partial\mathcal{L}}{\partial A^\mu} = \partial_\nu\left(\frac{\partial\mathcal{L}}{\partial(\partial_\nu A^\mu)}\right) \tag{3.9}$$

can be applied to the Lagrangian (3.5), giving the following field equations for $\phi(x)$ and $\mathbf{A}(x)$;

$$\boldsymbol{\nabla}^2 g\phi(x) = -g^2\psi^\dagger(x)\psi(x) \tag{3.10}$$

and

$$(\partial_t^2 - \boldsymbol{\nabla}^2)g\mathbf{A} = \frac{ig^2\boldsymbol{\nabla}^2\psi^\dagger(x)\psi(x)}{2M} - \frac{ig^2\psi^\dagger(x)\boldsymbol{\nabla}\psi(x)}{2M} + \partial_t(\boldsymbol{\nabla}g\phi(x)) \tag{3.11}$$

From the field equation (3.10) the magnitude of the coupling g can be estimated using the results from (3.3) and (3.8)

$$g^2 \sim \frac{p^2(Mv)^2}{p^3} = v \tag{3.12}$$

where ∇ is the momentum operator, $\sim p$, and so from (3.11), the magnitude of the vector potential is estimated as

$$g\mathbf{A}(x) \sim \frac{1}{p^2}\left(\frac{v}{M}p^4 + (Mv^2)p(Mv^2)\right) \sim Mv^3 \tag{3.13}$$

which is smaller than the scalar potential by a factor of the quark velocity. Thus estimates for the magnitudes of the electric and magnetic fields follow from

$$g\mathbf{E}(x) = -\nabla g\phi(x) + \cdots \sim p(Mv^2) = M^2v^3 \tag{3.14}$$

$$g\mathbf{B}(x) = \nabla \times g\mathbf{A}(x) + \cdots \sim p(Mv^3) = M^2v^4 \tag{3.15}$$

As expected for a nonrelativistic system, the magnetic fields are smaller than the electric fields by a factor of v in quarkonium. Equipped with these power counting rules, it is now possible to determine which terms in the quark action in NRQCD are potentially important for quarkonium physics.

3.3.1 Relativistic Corrections

Relativistic correction terms to the quark Lagrangian (3.5) must respect the symmetries of QCD such as gauge invariance, parity, charge conjugation and rotational symmetry. This limits the possibilities for interactions and to $\mathcal{O}(v^2)$ only four such correction terms are required

$$c_1\frac{1}{M^3}\psi^\dagger(x)\mathbf{D^4}\psi(x) \tag{3.16}$$

$$c_2\frac{g}{M^3}\psi^\dagger(x)(\mathbf{D}\cdot\mathbf{E} - \mathbf{E}\cdot\mathbf{D})\psi(x) \tag{3.17}$$

$$c_3 \frac{ig}{M^2} \psi^\dagger(x) \boldsymbol{\sigma} \cdot (\mathbf{D} \times \mathbf{E} - \mathbf{E} \times \mathbf{D}) \psi(x) \tag{3.18}$$

$$c_4 \frac{g}{M} \psi^\dagger(x) \boldsymbol{\sigma} \cdot \mathbf{B} \psi(x) \tag{3.19}$$

The first of the four corrections (3.16) follows from the expansion to $\mathcal{O}(Mv^4)$ of the formula for the relativistic energy of a noninteracting quark $E^2 = \mathbf{p}^2 + M^2$. The second correction (3.17) is the QCD equivalent of the Darwin term in QED which accounts for the zero point energy caused by fluctuations in the quark's position. The third correction (3.18) is a spin-dependent term called the spin-orbit coupling and it removes the degeneracy between states which have the same orbital angular momentum and spin quantum numbers but differing total angular momentum. The last correction (3.19) is also a spin-dependent term and this removes the degeneracy between states which have the same orbital angular momentum but differing spin.

To be able to use the NRQCD Lagrangian (3.5) together with the four correction terms (3.16) to (3.19) for QCD predictions, the coupling constants c_1, c_2, c_3, c_4 need to be evaluated. These coupling constants have unique values that are dependent on the ultra-violet cut-off Λ used to regulate the theory. Unlike QCD one is not able to remove the cut-off Λ in NRQCD by taking it to infinity since the theory contains power law divergences, contributing terms such as $\alpha_s \Lambda / M$ to the couplings making NRQCD non-renormalisable [18]. These terms render perturbation theory useless if Λ is made too large, however limiting the cut-off to $\Lambda \sim M$, the couplings can be obtained perturbatively. In the next section the coupling constants are obtained by computing simple scattering amplitudes in QCD, and matching them with scattering amplitudes from NRQCD.

3.4 Determination of the Couplings

Following the work of [20] tree-level values of the couplings c_1, ..., c_4 are established by matching results in NRQCD to those of low energy QCD through $\mathcal{O}(v^4)$

since the NRQCD Lagrangian is accurate to $\mathcal{O}(v^4)$.

As mentioned in section (3.3.1) for small momentum the relativistic energy-momentum dispersion relation can be expanded as

$$E = (\mathbf{p}^2 + M^2)^{1/2} = M + \frac{\mathbf{p}^2}{2M} - \frac{\mathbf{p}^4}{8M^3} + \cdots \tag{3.20}$$

so to order v^4, the $\mathbf{p^4}$ shift in the energy is accounted for by the correction term (3.16) which fixes $c_1 = 1/8$.

The tree level amplitude for scattering a quark off a static electric field in QCD is given by

$$M_E(\mathbf{p}, \mathbf{q}) = \overline{u}(\mathbf{q})\gamma^0 g\phi(\mathbf{q} - \mathbf{p})u(\mathbf{p}) \tag{3.21}$$

where ϕ is the scalar potential. The Dirac spinor for the quark is written in terms of the Pauli spinor ψ as

$$u(\mathbf{p}) = \left(\frac{E_p + M}{2E_p}\right)^{\frac{1}{2}} \begin{bmatrix} \psi \\ \frac{\boldsymbol{\sigma}\cdot\mathbf{p}}{E_p+M}\psi \end{bmatrix} \tag{3.22}$$

and is normalised nonrelativistically with $u^\dagger u = 1$ [25]. Inserting the spinor into the amplitude $M_E(\mathbf{p}, \mathbf{q})$ and expanding the dispersion relation $E_P = (\mathbf{p}^2 + M^2)^{1/2}$ in powers of $\mathbf{p}/M$, the amplitude can be divided into a spin-dependent part and a spin-independent part

$$M_E(\mathbf{p}, \mathbf{q}) = M_{SI}(\mathbf{p}, \mathbf{q}) + M_{SD}(\mathbf{p}, \mathbf{q}) \tag{3.23}$$

where

$$M_{SI}(\mathbf{p}, \mathbf{q}) = \left(i - \frac{i(\mathbf{p} - \mathbf{q})^2}{8M^2}\right) \psi^\dagger g\phi(\mathbf{q} - \mathbf{p})\psi \tag{3.24}$$

$$M_{SD}(\mathbf{p}, \mathbf{q}) = \left(\frac{-1}{4M^2} + \frac{3}{32M^4}(\mathbf{p}^2 + \mathbf{q}^2)\right) \psi^\dagger \boldsymbol{\sigma} \cdot \mathbf{q} \times \mathbf{p} g\phi(\mathbf{q} - \mathbf{p})\psi \tag{3.25}$$

The two parts contributing to the spin-independent amplitude can be shown to be accounted for by the NRQCD Lagrangian terms

$$\psi^\dagger(x)(iD_t)\psi(x) \text{ and} \tag{3.26}$$

$$c_2\frac{g}{M_2}\psi^\dagger(x)(\mathbf{D}\cdot\mathbf{E}-\mathbf{E}\cdot\mathbf{D})\psi(x) \tag{3.27}$$

since $\mathbf{E}(\mathbf{x}) = -\nabla\phi(\mathbf{x})$ for a static field, becomes $\mathbf{E}(\mathbf{p}) \sim \mathbf{p}\phi(\mathbf{p})$ in momentum space. From this comparison c_2 is found to be 1/8. Similarly the two parts contributing to $M_{SD}(\mathbf{p},\mathbf{q})$ are accounted for by the correction terms

$$c_3\frac{ig}{8M^3}\psi^\dagger(x)\boldsymbol{\sigma}\cdot(\mathbf{D}\times\mathbf{E}-\mathbf{E}\times\mathbf{D})\psi(x) \text{ and} \tag{3.28}$$

$$f_2\frac{ig}{M^4}\psi^\dagger(x)\{\mathbf{D}^2,\boldsymbol{\sigma}\cdot(\mathbf{D}\times\mathbf{E}-\mathbf{E}\times\mathbf{D})\}\psi(x) \tag{3.29}$$

from which c_3 is also found to be 1/8. The correction term (3.29) is of order $\mathcal{O}(v^6)$ and is of no importance for this work.

A similar analysis to the one above but with the quark scattering of a static vector potential gives a value of 1/2 for c_4.

3.5 NRQCD on the Lattice

As explained in section (1.3) lattice theory is developed in Euclidean space. Consequently in order to study the Υ meson on the lattice the NRQCD Lagrangian developed in sections (3.2) to (3.4) has to be transformed into Euclidean space where it is given by

$$\mathcal{L}_{NRQCD} = \psi^\dagger(x)\left(D_t - \frac{\mathbf{D}^2}{2M}\right)\psi(x) + \mathcal{L}_{SI} + \mathcal{L}_{SD} \tag{3.30}$$

where

$$\mathcal{L}_{SI} = -\frac{1}{8M^3}\psi^\dagger(x)\mathbf{D}^4\psi(x) + \frac{ig}{8M^2}\psi^\dagger(x)(\mathbf{D}.\mathbf{E}-\mathbf{E}.\mathbf{D})\psi(x) \tag{3.31}$$

$$\mathcal{L}_{SD} = -\frac{g}{8M^2}\psi^\dagger(x)\boldsymbol{\sigma}.(\mathbf{D}\times\mathbf{E}-\mathbf{E}\times\mathbf{D})\psi(x) - \frac{g}{2M}\psi^\dagger(x)\boldsymbol{\sigma}.\mathbf{B}\psi(x) \tag{3.32}$$

To discretise this action the covariant derivatives acting on the quark field in the continuum have to be replaced on the lattice by difference operations

$$a\Delta_\mu^{(+)}\psi(x) = U_\mu(x)\psi(x+a\hat{\mu}) - \psi(x) \tag{3.33}$$

$$a\Delta_\mu^{(-)}\psi(x) = \psi(x) - U_\mu^\dagger(x-a\hat{\mu})\psi(x-a\hat{\mu}) \tag{3.34}$$

$$a\Delta_\mu^{(\pm)}\psi(x) = \frac{1}{2}\left(a\Delta_\mu^{(+)} + a\Delta_\mu^{(-)}\right)\psi(x) \tag{3.35}$$

where the first two operations are forward and backward differences respectively, while the last operation is a centred or symmetric difference. The gauge invariance of the Lagrangian is maintained on the lattice by the inclusion of U_μ fields in each of the above operations.

The Laplacian operator $\mathbf{D}^2$ is replaced on the lattice by

$$\mathbf{\Delta}^{(2)} = \sum_i \Delta_i^{(+)}\Delta_i^{(-)} \tag{3.36}$$

allowing the kinetic energy operator H_0 to be written as

$$H_0 = -\sum_i \frac{\Delta_i^{(+)}\Delta_i^{(-)}}{2M} \tag{3.37}$$

The discretised quark action to leading order can now be written as

$$S = -a^3 \sum_x \psi^\dagger(x)\left(U_4(x)\psi(x+at) - (1-aH_0)\psi(x)\right) \tag{3.38}$$

Using the equation $\sum_{x'} K(x,x')G(x',0) = \delta_{x,0}$ one ends up with the evolution equation for the quark propagator

$$G(\mathbf{x}, t+a) = U_4^\dagger(x)(1-aH_0)G(\mathbf{x},t) + \delta_{\mathbf{x},0}\delta_{t,0} \tag{3.39}$$

where the notation $G(\mathbf{x},t) = G(\mathbf{x},t;\mathbf{x_0},t_0)$ has been used.

This evolution equation becomes unstable at high momentum modes. This can be seen by looking at (3.39) in momentum space where the kinetic energy operator is given by

$$aH_0 = \frac{\sum_i 4\sin^2 \frac{p_i a}{2}}{2Ma} \tag{3.40}$$

It can be seen immediately that the maximum value allowed for $aH_0 = 6/Ma$ where $p_i = \frac{\pi}{a}$. Since for smooth evolution one requires that $|1 - aH_0| < 1$, this means that the evolution equation will start to blow up for $Ma < 3$. To prevent this, the evolution equation is replaced by

$$G(\mathbf{x}, t+a) = \left(1 - \frac{aH_0}{2n}\right)^n U_4^\dagger(x) \left(1 - \frac{aH_0}{2n}\right)^n G(\mathbf{x}, t) + \delta_{\mathbf{x},0}\delta_{t,0} \tag{3.41}$$

which is now stable for $ma > \frac{3}{n}$ [20]. The high momentum modes are expected to have little effect on the spectrum of bottomium which is determined by much lower momentum modes. The instability from the high momentum modes is just a numerical effect and the extra interactions which will occur to eliminate the instability will be suppressed by the lattice spacing a.

Considering the next to leading order terms ($\mathcal{O}(v^4)$) in (3.31) and (3.32) requires the calculation of the chromoelectric and chromomagnetic fields on the lattice. In the continuum these fields are defined by

$$E_i(x) = F_{0i}(x) \tag{3.42}$$

$$B_i(x) = \frac{1}{2}\epsilon_{ijk}F_{jk}(x) \tag{3.43}$$

So a lattice equivalent of $F_{\mu\nu}(x)$ needs to be used. This is taken to be the cloverleaf representation [26] of $F_{\mu\nu}(x)$ defined in terms of plaquettes

$$F^c_{\mu\nu}(x) = -\frac{1}{4ga^2}\sum_P \mathcal{O}(P) \tag{3.44}$$

where

$$\mathcal{O}(P) = \frac{U_{\mu\nu}(x) - U^\dagger_{\mu\nu}(x)}{2i} - \frac{1}{3}Im(Tr(U_{\mu\nu}(x))I \tag{3.45}$$

with the summation over the four plaquettes centred at x and in the $\mu\nu$ plane. The cloverleaf definition makes $F^c_{\mu\nu}$ antihermitian and traceless as in the continuum case.

3.6 Lattice Spacing Errors

The finite spacing of the lattice introduces systematic errors into NRQCD which must be corrected if predictions from simulations are to be believed. That is, believing there is independence of the artificial cut-off introduced into the calculation as the lattice spacing. From the definition of the gauge field $U_\mu(x) = e^{igaA_\mu(x)}$ it can be seen (by Taylor expanding $\psi(x+a\hat{\mu})$) that the difference operators (3.33), (3.34) and (3.35) can be expanded by exponential power series in the covariant derivative D_μ

$$\begin{aligned} a\Delta^{(+)}_\mu \equiv \exp(aD_\mu) - 1 &= aD_\mu + \frac{a^2}{2}D^2_\mu + \dots \\ a\Delta^{(-)}_\mu \equiv 1 - \exp(-aD_\mu) &= aD_\mu - \frac{a^2}{2}D^2_\mu + \dots \\ a\Delta^{(\pm)}_\mu &= aD_\mu + \frac{a^3}{6}D^3_\mu + \dots \end{aligned} \tag{3.46}$$

From theses expansions, we obtain 1st order improvements to these difference operators that reproduce the effects of D_μ to order a^2 for (3.33), (3.34) and order a^4 for (3.35)

$$\begin{aligned} \tilde{\Delta}^{(+)}_\mu &= \Delta^{(+)}_\mu - \frac{a}{2}\Delta^{(+)2}_\mu \\ \tilde{\Delta}^{(-)}_\mu &= \Delta^{(-)}_\mu + \frac{a}{2}\Delta^{(-)2}_\mu \\ \tilde{\Delta}^{(\pm)}_\mu &= \Delta^{(\pm)}_\mu - \frac{a^2}{6}\Delta^{(+)}_\mu\Delta^{(\pm)}_\mu\Delta^{(-)}_\mu \end{aligned} \tag{3.47}$$

we can use these results to improve the lattice Laplacian, given by

$$a^2\mathbf{\Delta}^{(2)} = \sum_i \left(a^2 D_i^2 + \frac{a^4}{12}D_i^4 + \dots \right) \tag{3.48}$$

resulting in an improvement that is also accurate to order a^4

$$\tilde{\boldsymbol{\Delta}}^{(2)} = \boldsymbol{\Delta}^{(2)} - \frac{a^2}{12}\sum_i \left(\Delta_i^{(+)}\Delta_i^{(-)}\right)^2 \tag{3.49}$$

Temporal derivatives enter NRQCD differently than spatial derivatives because the theory is non-relativistic. A consequence of this is that quark propagation is governed by a Scrödinger-like equation with a single time derivative, making the calculation of the quark green functions an initial value problem. If we improve the time derivative operator as we did for spatial derivatives, this initial value problem would be lost as higher order time derivatives enter the theory. Alternatively using (3.47), the covariant time derivative may be written as

$$aD_4 = a\Delta_4^{(+)} - \frac{a^2}{2}D_4^2 - \frac{a^3}{6}D_4^3 - \frac{a^4}{24}D_4^4 - \ldots \tag{3.50}$$

where at lowest order $D_4 \simeq \frac{\mathbf{D}^2}{2M} \simeq -H_0$.

When replacing this improvement for the time derivative into the quark action (3.38) the extra terms in (3.50) form an exponential power series factor in H_0, which modifies the evolution equation (3.39)

$$G(\mathbf{x}, t+a) = U_4^\dagger(x)e^{-aH_0}G(\mathbf{x},t) + \delta_{\mathbf{x},0}\delta_{t,0} \tag{3.51}$$

However this evolution equation is unstable at high momentum modes for the same reasons discussed for the evolution equation (3.39), so it is necessary to incorporate the improvements for the time derivative into the evolution equation (3.41), stable at such modes for evolving the quark propagator at at lowest order. This is achieved by comparing evolution equations (3.41) and (3.51) giving the effective Hamiltonian of the second in terms of the Hamiltonian of the first

$$\begin{aligned} H_{eff} &= -\frac{2n}{a}\ln\left(1 - \frac{aH_0}{2n}\right) \\ &= H_0 + \frac{a}{4n}H_0^2 + \ldots \end{aligned} \tag{3.52}$$

The order a terms in the effective Hamiltonian cancels if we replace H_0 by

$$\tilde{H}_0 \equiv H_0 - \frac{a}{4n} H_0^2 \tag{3.53}$$

Making this replacement in the stable evolution equation (3.41) removes the leading error due to the lattice approximation of the time derivative.

As demonstrated in section (3.3), the four correction terms in the NRQCD Lagrangian (3.30) have magnitude $\mathcal{O}(Mv^4)$. Therefore any discretisation errors of magnitude $\mathcal{O}(Mv^4)$ or less must be corrected for in order to retain an accuracy of $\mathcal{O}(Mv^4)$ in the simulation. It can readily be seen that the correction term which improves the centred difference operator, given by (3.47) is a factor of $\mathcal{O}(a^2M^2v^2) \sim \mathcal{O}(v^2)$ (making the assumption $Ma \sim 1$) smaller in magnitude than the difference operator it corrects and since this difference operator is only required in the $\mathcal{O}(Mv^4)$ correction terms (3.31) and (3.32) the improved version is unnecessary. The improvements to the Hamiltonian (resulting from the temporal derivative) and the lattice Laplacian however, have to be included since they are of magnitude

$$-\frac{a}{4n} H_0^2 \sim a(Mv^2)^2 \sim Mv^4 \tag{3.54}$$

$$\frac{a^2}{24M} \sum_i (\Delta_i^{(+)} \Delta_i^{(-)})^2 \sim \frac{a^2}{M} (M^2v^2)^2 \sim Mv^4 \tag{3.55}$$

The way in which these corrections are implemented is demonstrated in the next section.

The cloverleaf electromagnetic field strength tensor $F^c_{\mu\nu}$ can also be improved and a detailed account can be found in [20]. However the first order corrections to the electromagnetic field have a magnitude $\mathcal{O}(a^2M^4v^5)$ which is a factor $\mathcal{O}(v^2)$ smaller than the magnitude of the lowest order field $\mathcal{O}(M^2v^3)$, hence the cloverleaf correction is not required when working to $\mathcal{O}(Mv^4)$.

3.7 The Evolution of the Quark Propagator

The evolution equation (3.41) for the quark propagator is appropriate for leading order $\mathcal{O}(Mv^2)$ terms. Now that all $\mathcal{O}(Mv^4)$ corrections have been established, the evolution equation can be modified to include them

$$G(\mathbf{x}, t+a) = \left(1 - \frac{aH_0}{2n}\right)^n U_4^\dagger(x) \left(1 - \frac{aH_0}{2n}\right)^n (1 - a\delta H) G(\mathbf{x}, t) \tag{3.56}$$

where the initial condition is given by

$$G(\mathbf{x}, 0) = \delta_{\mathbf{x},0} \tag{3.57}$$

and δH contains all four relativistic corrections and the two lattice spacing corrections.

$$\begin{aligned} \delta H \;=\; & -\frac{(\boldsymbol{\Delta}^{(2)})^2}{8(M_b^0)^3} + \frac{ig}{8(M_b^0)^2}(\boldsymbol{\Delta}_\pm \cdot \mathbf{E} - \mathbf{E} \cdot \boldsymbol{\Delta}_\pm) - \frac{g}{8(M_b^0)^2}\boldsymbol{\sigma} \cdot (\boldsymbol{\Delta}_\pm \times \mathbf{E} - \mathbf{E} \times \boldsymbol{\Delta}_\pm) \\ & -\frac{g}{2M_b^0}\boldsymbol{\sigma} \cdot \mathbf{B} + \frac{a^2 \boldsymbol{\Delta}^{(4)}}{24 M_b^0} - \frac{a(\boldsymbol{\Delta}^{(2)})^2}{16n(M_b^0)^2} \end{aligned} \tag{3.58}$$

All of the difference operators in (3.58) act on everything to the right, with their action identical to the difference operators defined in equations (3.33), (3.34) and (3.35). However the action of the centred difference operator acting on the **E** field in (3.58) is defined as

$$\boldsymbol{\Delta}_\pm \mathbf{E} = \frac{1}{2a} \sum_i \left[U_i(x) E_i(x + ai) U_i^\dagger(x) - U_i^\dagger(x - ai) E_i(x - ai) U_i(x - ai) \right] \tag{3.59}$$

This is different from that of (3.35) in order to preserve the gauge invariance of the NRQCD lattice Lagrangian.

3.8 Radiative Corrections

In section (3.3.1), relativistic correction terms to the nonrelativistic quark Lagrangian (3.5) were considered, each with its own coupling constant c_i. These

coupling constants were found by comparing NRQCD to low energy QCD at tree level. However radiative corrections to these tree level values are believed to be large and must therefore be taken into account, and the coupling constants must be shifted away from their tree level values appropriately. The belief that radiative corrections are large comes from the fact that Monte Carlo estimates for most short distance quantities on the lattice disagree poorly with lowest order lattice perturbation theory estimates. An example is the vacuum expectation value of the lattice gluon operator U_μ in the Landau gauge [27].

$$\langle 1 - \frac{1}{3} Tr U_\mu \rangle_{MC} = 0.139 \tag{3.60}$$

This is the lattice analogue of the expectation value $\langle A_\mu^2 \rangle$ of the square of the gauge field A_μ. Since $\langle A_\mu^2 \rangle$ is quadratically divergent, the loop integral is dominated by momenta close to the cutt-off and so at $\beta = 6.0$ perturbation theory should work for cut-offs of order a couple of GeV or larger, giving

$$\langle 1 - \frac{1}{3} Tr U_\mu \rangle_{PT} = 0.97 \alpha_{Latt} = 0.078 \tag{3.61}$$

where $\alpha_{Latt} \equiv g^2/4\pi$. As can be seen, the result obtained by perturbation theory, differs considerably from the Monte Carlo estimate. These differences arise from the naive relationship between the lattice gauge link and continuum gauge field

$$U_\mu(x) \equiv e^{iga A_\mu(x)} \rightarrow 1 + iga A_\mu(x) \tag{3.62}$$

This expansion seems reasonable when the lattice spacing a is small, but it is misleading since further higher corrections in the expansion do not vanish as powers of a in quantum theory. Higher order terms in the expansion of U_μ contain additional factors like $g^2 a^2 A_\mu^2$ where A_μ^2 will quadratically diverge as $\frac{1}{a^2}$ and so precisely cancel out the a^2. For example

$$g^2 a^2 A_\mu^2 \sim a^2 M^2 v^6 \sim \frac{a^2 v^6}{a^2} \sim g^3 \tag{3.63}$$

Consequently these higher correction terms to U_μ are suppressed only by powers of g (not a), and turn out to be large. These corrections are known as QCD

tadpole contributions and lead to large renormalizations between the lattice and the continuum, which in turn leads to large coefficients for perturbative expansions in α_{Latt} and hence poor convergence of these expansions. This problem can be resolved by refining the naive formula that connects the lattice operator to the continuum operator (3.62). Consider the vacuum expectation values of these operators. In the continuum, the expectation value $\langle 1 + iaga_\mu(x)\rangle$ is 1. In the lattice theory, tadpole contributions renormalize the link operator so that its vacuum expectation value is considerably smaller than 1 [27]. This suggests that the appropriate connection with the continuum fields is more like

$$U_\mu(x) \rightarrow u_0(1 + iagA_\mu(x)) \tag{3.64}$$

where u_0 is a gauge invariant expression, which can be defined is several ways, here it is chosen to be the fourth root of the plaquette expectation value

$$u_0 = \langle \frac{1}{3} TrU_P \rangle^{1/4} \tag{3.65}$$

For a more continuum like behaviour, all gauge links appearing in operators are divided by the parameter u_0. This is important when the chromoelectric and chromomagnetic fields are evaluated. This involves the evaluation of the plaquette which contains the four U_μ fields and tadpole improving using the above prescription will change the definition of the cloverleaf term according to

$$\begin{aligned} \mathbf{E} &\rightarrow \frac{\mathbf{E}}{u_0^4} \\ \mathbf{B} &\rightarrow \frac{\mathbf{B}}{u_0^4} \end{aligned} \tag{3.66}$$

This increases the strength of the fields and therefore neglecting tadpole-improvement will severly underestimate spin-plittings. Similarly, this prescription for building continuum operators suggests that

$$\tilde{S}_G = \sum \frac{1}{2\tilde{g}^2 u_0^4} Tr(U_P + U_P^\dagger) \qquad \text{where} \qquad \tilde{g}^2 = \frac{g^2}{u_0^4} \tag{3.67}$$

is a better gluon action for lattice QCD. In particular, perturbation theory, expanded in $\tilde{\alpha}_{Latt} = \tilde{g}^2/4\pi$ is far more convergent. This is because tadpole improvement has removed the tadpole contributions which are responsible for the bulk of radiative corrections meaning that it is now possible to keep tree level values for the arbitrary coupling constants $c_1, \ldots, c_6$.

3.9 Meson Operators

From section (3.2) it was seen that the FWT transformation decouples the 4 component Dirac spinor Ψ into a 2 component Pauli spinor ψ_Q describing the quark dynamics and a 2 component spinor χ_A describing the antiquark dynamics. The actions for the quark and antiquark are then defined by

$$S = S_Q + S_A \tag{3.68}$$

where the quark action can be written in the form

$$S_Q = \sum_{x,y} \psi^\dagger(x) K_Q(x,y) \psi(y) \tag{3.69}$$

where $K_Q(x,y)$ is the inverse of the quark Greens function from which the quark propagator can be found. The antiquark action is similarly written as

$$S_A = \sum_{x,y} \chi^\dagger(x) K_A(x,y) \chi(y) \tag{3.70}$$

A consequence of the decoupling from a Dirac spinor Ψ to 2 Pauli spinors ψ_Q and χ_A is that $K_A(x,y) = K_Q^*(x,y)$ [29]. This result is important since it connects the dynamics of the quark and antiquark meaning that the antiquark propagator is given by the complex conjugate of the quark propagator.

In order to simulate mesons on the lattice, it is necessary to define meson operators.

$$\mathcal{O}(x) = \chi_A(x) \Gamma^\dagger \psi_Q(x) \quad \mathcal{O}^\dagger(x) = \psi_Q^\dagger(x) \Gamma \chi_A^\dagger(x) \tag{3.71}$$

where for example $\psi_Q^\dagger(x)$ creates a quark and $\chi_A^\dagger(x)$ creates an antiquark, combining these in the form of $\mathcal{O}^\dagger(x)$ creates a meson, with the appropriate quantum numbers determined by Γ. $\mathcal{O}(x)$ consequently must be a meson annihilation operator that destroys the quark and antiquark. To define meson correlation functions for each type of meson state, it is necessary to define Γ explicitly. The spectroscopic notation for meson states are conventionally labelled by the quantum numbers spin S, orbital angular momentum L and total angular momentum J, usually given in the compact form $^{2S+1}L_J$. Of these three quantum numbers, only the total angular momentum J is conserved. However two other quantum numbers, the intrinsic parity P and the charge conjugation C are conserved and for mesons are given by $P = (-1)^{L-1}$ and $C = (-1)^{L+S}$. It is therefore possible to label meson states by J^{PC} instead. From this we can see that states with the same J^{PC} will mix together, for example, the $^3S_1$ and $^3D_1$. The types of operator Γ chosen to create various meson states are given in table (3.1), along with the lattice cubic group representation for each state.

As an example of how these operators work consider the creation of the $^1S_0$ state, where the operator Γ is chosen to be the identity matrix I. This choice can be justified by noting that the state has spin $S = 0$ and orbital angular momentum $L = 0$. It therefore does not need components formed from Pauli spin matrices to project spin or spatial derivatives to project angular momentum.

As another example consider the $^3S_1$ state where $S = 1$, $L = 0$, and $J = 1$, again no derivatives are required to act on the fields to project orbital angular momentum, while spin $S = 1$ is created using the Pauli spin matrices

$$\boldsymbol{\sigma} = (\sigma_x, \sigma_y, \sigma_z) \tag{3.72}$$

It is possible to project individual polarisations of $^3S_1$ state; ^3S_1x, ^3S_1y and ^3S_1z using the respective spin matrices σ_x, σ_y and σ_z.

As a final example consider the $^1P_1$ state where $S = 0$, $L = 1$ and $J = 1$. It can be seen that this state requires no spin matrices since $S = 0$ but requires $L = 1$ which can be achieved by making the operator Γ acting on the field, a

Meson state $^{2S+1}L_J\ (J^{PC})$	Lattice Representation	Γ
$^1S_0\ (0^{-+})$	A_1^{-+}	I
$^3S_1\ (1^{--})$	$T_{1(i)}^{--}$	σ_i
$^1P_1\ (1^{+-})$	$T_{1(i)}^{+-}$	Δ_i
$^3P_0\ (0^{++})$	A_1^{++}	$\sum_j \Delta_j\sigma_j$
$^3P_1\ (1^{++})$	$T_{1(k)}^{++}$	$\Delta_i\sigma_j - \Delta_j\sigma_i$
$^3P_2\ (2^{++})$	$E_{(k)}^{++}$	$\Delta_i\sigma_i - \Delta_j\sigma_j$
	$T_{2(ij)}^{++}$	$\Delta_i\sigma_j + \Delta_j\sigma_i$
		$(i \neq j)$
$^1D_2\ (2^{-+})$	$E_{(k)}^{-+}$	$D_{ii} - D_{jj}$
	$T_{2(ij)}^{-+}$	D_{ij}
		$(i \neq j)$
$^3D_1\ (1^{--})$	$T_{1(i)}^{--}$	$\sum_j D_{ij}\sigma_j$
$^3D_2\ (2^{--})$	$E_{(j)}^{--}$	$D_{ij}\sigma_k - D_{jk}\sigma_i$
	$T_{2(ij)}^{--}$	$(D_{ii} - D_{jj})\sigma_k +$
		$D_{jk}\sigma_j - D_{ki}\sigma_i$
$^3D_3\ (3^{--})$	S_2^{--}	$(D_{ij}\sigma_k + D_{jk}\sigma_i + D_{ki}\sigma_j)/3$
	$T_{1(i)}^{--}$	$D_{ii}\sigma_i - 2/5\sigma_j D_{ij}\sigma_j$
	$T_{2(ij)}^{--}$	$(D_{ii} - D_{jj})\sigma_k +$
		$2(D_{ki}\sigma_i - D_{kj}\sigma_j)$

Table 3.1: Various meson operators. Δ_i denotes the symmetric lattice derivative and $D_{ij} \equiv \Delta_i\Delta_j - \delta_{ij}\Delta^2/3$.

derivative Δ_i. A far more rigorous derivation of many of the different meson operators shown in table (3.1), can be found in [29].

3.10 Meson Correlators

In the previous section it was shown how meson operators can be formed to create or annihilate mesons with specific quantum numbers. The propagation of these mesons from space point $\mathbf{x_0}$ to $\mathbf{x}$ and time t_0 to t is represented by the correlation function

$$C(\mathbf{x}, t; \mathbf{x_0}, t_0) = \langle 0|\mathcal{O}(\mathbf{x}, t)\mathcal{O}^\dagger(\mathbf{x_0}, t_0)|0\rangle \tag{3.73}$$

Inserting the meson operators (3.71) we obtain

$$C(\mathbf{x}, t; \mathbf{x_0}, t_0) = \langle 0|\chi(\mathbf{x}, t)\Gamma^\dagger\psi(\mathbf{x}, t)\psi^\dagger(\mathbf{x_0}, t_0)\Gamma\chi^\dagger(\mathbf{x_o}, t_0)|0\rangle \tag{3.74}$$

making colour and spin indices explicit, the correlation function can be written as

$$\begin{aligned} C(\mathbf{x}, t; \mathbf{x_0}, t_0) &= \langle 0|\chi_i^\alpha(\mathbf{x}, t)\Gamma^\dagger_{\alpha\beta}\psi_i^\beta(\mathbf{x}, t)\psi_j^{\dagger\delta}(\mathbf{x_0}, t_0)\Gamma_{\delta\epsilon}\chi_j^{\dagger\epsilon}(\mathbf{x_o}, t_0)|0\rangle \\ &= \langle 0|\chi_i^\alpha(\mathbf{x}, t)\chi_j^{\dagger\epsilon}(\mathbf{x_o}, t_0)\Gamma^\dagger_{\alpha\beta}\psi_i^\beta(\mathbf{x}, t)\psi_j^{\dagger\delta}(\mathbf{x_0}, t_0)\Gamma_{\delta\epsilon}|0\rangle \end{aligned} \tag{3.75}$$

We can now write the correlation function in terms of Green functions [30]

$$\begin{aligned} C(\mathbf{x}, t; \mathbf{x_0}, t_0) &= G^{*\alpha\epsilon}_{i,j}(\mathbf{x}, t; \mathbf{x_0}, t_0; U)\Gamma^\dagger_{\alpha\beta}G^{\beta\delta}_{i,j}(\mathbf{x}, t; \mathbf{x_0}, t_0; U)\Gamma_{\delta\epsilon} \\ &= Tr[G^\dagger(\mathbf{x}, t; \mathbf{x_0}, t_0; U)\Gamma^\dagger G(\mathbf{x}, t; \mathbf{x_0}, t_0; U)\Gamma] \end{aligned} \tag{3.76}$$

where the Green functions represent quark propagators on a single gauge configuration U, which are then averaged over the complete set of gauge configurations $\{U\}$ with the correct Boltzmann weight (see section 1.4 for more details). The trace is taken over both spin and colour indices.

3.11 Effective Mass

In the Euclidean space of the lattice these two point correlation functions decay exponentially with time with an exponent equal to the energy of the hadronic state in question. To show that this is the case consider the correlation function

$$C(t) = G_M(t) = \langle 0|\mathcal{O}(t)\mathcal{O}^\dagger(0)|0\rangle \tag{3.77}$$

In the Feynman path integral approach the operator $\mathcal{O}$ is in the Heisenberg representation and evolves in Euclidean time

$$\mathcal{O}(t) = U^\dagger \mathcal{O}(0) U \tag{3.78}$$

where $U = e^{-\mathcal{H}t}$ is the Euclidean space evolution operator for some Hamiltonian operator $\mathcal{H}$. Inserting a complete set of energy eigenstates states into equ (3.77)

$$\sum_n |n\rangle\langle n| = 1 \tag{3.79}$$

we obtain

$$\begin{aligned} C(t) &= \sum_n \langle 0|\mathcal{O}(t)|n\rangle\langle n|\mathcal{O}^\dagger(0)|0\rangle_{HR} \\ &= \sum_n \langle 0|U^\dagger\mathcal{O}(0)U|n\rangle\langle n|\mathcal{O}^\dagger(0)|0\rangle_{HR} \\ &= \sum_n \langle 0|\mathcal{O}(0)e^{-\mathcal{H}t}|n\rangle\langle n|\mathcal{O}^\dagger(0)|0\rangle_{SR} \\ &= \sum_n |\langle 0|\mathcal{O}(0)|n\rangle|^2 e^{-E_n t} \\ &= |\langle 0|\mathcal{O}(0)|1\rangle|^2 e^{-M_1 t} + \cdots \end{aligned} \tag{3.80}$$

where we have restricted ourselves to states with zero momentum so that $E_n = M_n$. For hadrons at rest equ (3.80) is known as a timeslice propagator for the hadron with quantum numbers of the operator $\mathcal{O}$.

A useful tool in diagnosing the point in time at which all the higher mass states have decayed away is the effective mass function

$$m_{eff} = -\ln\left[\frac{C(t+1)}{C(t)}\right] \tag{3.81}$$

As $t \to \infty$ this function levels out into a plateau at M_1, enabling one to identify the ground state. In practice however it is usual to use the effective mass function to pick out the time region in which the ground state dominates. The meson mass is then extracted with more accuracy by fitting the timesliced propagator to an exponential Ae^{-mt} over this region. The amplitude $\langle 0|\mathcal{O}(0)|n\rangle$ is the matrix element for the decay of the meson, a non-perturbative quantity which can only be calculated by lattice simulations.

3.12 Smearing

As discussed in the last section the ground state mass of a particular meson state is extracted by eliminating contributions from all the higher mass states $|n\rangle$ from the correlation function (3.80). This is achieved by taking the time to infinity. On a lattice, however this is not possible since there is a restriction on the size of the time direction and the signal will become dominated by noise before the ground state is isolated. To increase the numerical accuracy of the simulation the signal must be extracted at earlier times where the noise has not yet started to dominate. This is possible using smeared operators. In earlier sections only local operators were considered, meaning for example that the two-point correlation function for the ${}^1S_0$ state is calculated by creating the meson at a single source point. Similarly in the case of the ${}^1P_1$ state, the antiquark was displaced by a minimal amount, of one lattice spacing relative to the quark to project out the required angular momentum. Mesons are thus created at a single local source point, for example at the origin of the lattice at $t = 0$, and evaluated at all possible sink points. These sink points are then summed over the three spatial directions to obtain the timesliced propagator from which masses are extracted. There are thus three choices for improving the local hadron operators using smearing; smear the sink, smear the source or both. To implement smearing the quark or

anti-quark is smeared over the whole of the lattice relative to the antiquark or quark with an appropriate weighting function. The idea is that a meson operator is chosen in such a way that the ground state (or first excited state, ...) overlap will dominate from small times onwards.

The meson operators used to create the states investigated in this thesis are formed from two operators Γ and $S(r)$, where Γ is the 2×2 matrix in spin space discussed in section (3.9) which generally includes derivatives that act on the radial smearing function $S(r)$. The smeared meson operator is defined as

$$\Gamma(\mathbf{x}) = \Gamma S(\mathbf{x}) \tag{3.82}$$

The role of the radial smearing function allows us to create states which we wish to extract with a specific energy quantum number n. Γ, as in the last section makes sure that the state has the required quantum numbers J^{PC}. To put it on a more formal basis we define the smeared anti-quark field at the source by the replacement

$$\chi^\dagger(x_0,t) \rightarrow \tilde{\chi}^\dagger(x_0,t) = \sum_z S(z-x_0)\chi^\dagger(z,t) \tag{3.83}$$

and the smeared antiquark field at the sink by

$$\chi(x,t) \rightarrow \tilde{\chi}(x,t) = \sum_y \chi(y,t)S^\dagger(y-x) \tag{3.84}$$

A general expression for the meson correlator with smearing at the source and sink can be obtained by substituting these replacements into (3.77)

$$\begin{aligned} C(t;t_0) &= \sum_x \langle 0|\tilde{\chi}(x,t)\Gamma^\dagger\psi(x,t)\psi^\dagger(x_0,t_0)\Gamma\tilde{\chi}^\dagger(x_0,t_0)|0\rangle \\ &= \sum_{x,y,z} \langle 0|\chi(y,t)\phi^\dagger(|y-x|)\Gamma^\dagger\psi(x,t)\psi^\dagger(x_0,t_0)\Gamma\phi(|z-x_0|)\chi^\dagger(z,t)|0\rangle \\ &= \sum_{x,y,z} \langle 0|\chi(y,t)\Gamma^{(sk)\dagger}(y-x)\psi(x,t)\psi^\dagger(x_0,t_0)\Gamma^{(sc)}(z-x_0)\chi^\dagger(z,t)|0\rangle \end{aligned} \tag{3.85}$$

To implement smearing at the source numerically, it is known that at $t = 0$

$$\langle 0|\chi^\dagger(y)\chi(x_0)|0\rangle = \delta_{y,x_0} \tag{3.86}$$

and so

$$\begin{aligned}\langle 0|\chi^\dagger(y)\tilde{\chi}(x_0)|0\rangle &= \sum_z \langle 0|\chi^\dagger(y)\chi(z)|0\rangle S(z-x_0) \\ &= \sum_z \delta_{z,y} S(z-x_0) \\ &= S(y-x_0)\end{aligned} \tag{3.87}$$

Therefore instead of starting off with a delta function in the evolution, this can be simply replaced by the function $S(y-x_0)$ over the whole of the lattice.

For this thesis, smearings were required to reproduce ground and first excited D states. These smearings are denoted by n_{sc} and n_{sk}, depending on whether the smearing is at the source or sink. For example, $n_{sc} = 1$ and $n_{sk} = 2$ denotes ground and first excited state smearing at the source respectively. $n_{sc} = loc$ denotes local smearing at the source and is given by the delta function in (3.86). The explicit forms of smearing functions $S(r)$ for any particular meson state are obtained using a Richardson potential model [5], which yields values at integral values of the radius from the origin r. Values in between are obtained using linear interpolation.

3.13 Correlated Fits

As described in section (3.11) the effective mass function can be used as a naive model to determine the ground state mass. However since the values of the correlator at only two timeslices are used a more effective method of determining the ground and subsequent excited states would be to fit the data from one correlation function $C(t;t_0)$ to some functional form over as many timeslices as possible. From equation (3.80) we know the form of the behaviour of the asymptotic fall off for a meson correlation function. It would then seem appropriate to fit the data from one correlation $C(t;t_0)$ to the function

$$C_{theo}(t;t_0) = A_1 e^{-E_1} + A_2 e^{-E_2} + \ldots \tag{3.88}$$

where the energy of the ground state E_1, the first excited state $E_2 \ldots$, and the amplitudes $A_1, A_2, \ldots$ are given as initial guesses. The usual way to fit data to a functional form is to minimise a measure of the goodness of fit as a function of the fit parameters $(A_1, E_1, \ldots)$. The goodness of fit for this model is given by the χ^2-function

$$\chi^2 = \sum_{i=1}^{N} \left(\frac{C(t_i) - C_{theo}(t_i; A_1, A_2, \ldots, E_1, E_2, \ldots)}{\sigma_i^2} \right) \tag{3.89}$$

and is subsequently minimised by varying each of the parameters in turn and re-evaluating. The χ^2 function has no specific value which needs to be reached upon minimisation but in general if χ^2 per degree of freedom is less than one then the fit is deemed acceptable. The number of degrees of freedom are defined as $N - n$ where N is the number of data points and n is the number of fitted parameters. The quantities represented by σ_i are just the standard deviations of the meson correlators averaged over configurations. The variance in this case is defined as

$$\sigma^2 = \sum_{i=1}^{N} \frac{(C(t_i) - C_{theo}^{min\chi^2}(t_i))^2}{N - n} \tag{3.90}$$

which can be calculated once the minimum χ^2 has been found.

3.13.1 Multi-Correlated Fits

The method of fitting to a single correlation discussed in the previous section is a naive model to use for extracting masses from the data and can be improved by simultaneously fitting to several meson correlators which have different types of smearing. This improved method described in [29] involves fitting correlation data to one of two functional forms.

Firstly define the meson correlation function as

$$C(n_{sc}, n_{sk}; t) = \langle 0|\mathcal{O}_{sk}(t)\mathcal{O}^{\dagger}_{sc}(0)|0\rangle \tag{3.91}$$

where $\mathcal{O}_{sk}$ represents the type of smearing at the sink etc. Inserting a complete set of energy eigenstates one obtains

$$C(n_{sc}, n_{sk}; t) = \sum_{k} \langle 0|\mathcal{O}_{sk}(t)|k\rangle\langle k|\mathcal{O}^{\dagger}_{sc}(0)|0\rangle e^{-E_k t} \tag{3.92}$$

The first functional form that can be fitted is called the matrix fit and is given by

$$C_{theo}(n_{sc}, n_{sk}; t) = \sum_{k=1}^{N_{exp}} a(n_{sc}, k)a^*(n_{sk}, k)e^{-E_k t} \tag{3.93}$$

Often the group of correlators used for the matrix fit have (n_{sc}, n_{sk}) given by $(1,1),(1,2),(2,1),(2,2)$. One can make the identification $a(n_{sc}, k) = \langle n|\mathcal{O}^{\dagger}_{sc}(0)|0\rangle$, $a(n_{sk}, k) = \langle n|\mathcal{O}^{\dagger}_{sk}(0)|0\rangle$ as the sum over the exponential tends to infinity.

The second functional form is called the vector or row fit and is given by

$$C_{theo}(n_{sc}, n_{sk}; t) = \sum_{k=1}^{N_{exp}} b(n_{sc}, k)e^{-E_k t} \tag{3.94}$$

with $b(n_{sc}, k) = a(n_{sc}, k)a^*(loc, k)$, where n_{sk} in equ (3.93) has been replaced with loc. The group of correlators used for the row fit have (n_{sc}, loc) given by $(1, loc), (2, loc), \ldots$.

Different combinations of smearing at the sink and at the source can be used simultaneously in the fit restraining the energy parameters for each of the radial excitations to have the same value. This will involve using data which is correlated between data points from different meson correlation functions as well as the correlation from different time values. To do this we define a generalised version of equ (3.89) for the χ^2 to be minimised

$$\chi^2 = \sum_{\alpha,\beta=1}^{N_{corr}} \sum_{t,t'=t_{min}}^{t_{max}} \left(C_\alpha(t) - C^{theo}_\alpha(t, a_i)\right) \left(\sigma^2\right)^{-1}_{\alpha\beta}(t, t') \left(C_\beta(t) - C^{theo}_\beta(t, a_i)\right) \tag{3.95}$$

The α, β indices represent different meson correlation functions, i.e., different types of smearing combinations and t and t' are time indices. C_{theo} is the functional form that is fitted, which is either of the type (3.93) or (3.94) and a_i are the fitting parameters. The matrix σ^2 is called the covariance matrix and measures the likely error on each of the data-points. It is defined by

$$\sigma^2_{\alpha\beta}(t,t') = \frac{1}{N_{conf}-1} \sum_{i=1}^{N_{conf}} \left(C_\alpha(t) - \langle C_\alpha(t)\rangle\right)\left(C_\beta(t) - \langle C_\beta(t)\rangle\right) \tag{3.96}$$

where N_{conf} is the number of gauge configurations. The covariance matrix is a square matrix of side length $(N_{corr} \times N_t)$, where N_{corr} is the number of correlators used in the simultaneous fit and N_t is the time range in which the fitting is performed. The best fit, using the multi correlated fit is obtained in the same way as detailed in the last section. Initial guesses are given for each of the fit parameters and χ^2 is calculated and then minimised by varying each of the parameters in turn until the χ^2 per degree of freedom is less than one.

Chapter 4

Simulation Results

In this chapter the spectrum of the D-states of Υ at β=6.0 will be studied in detail. The spectrum can be obtained using the multi-exponential and multi-correlated fitting methods described in the last chapter. Simulation data is also studied for $\beta = 5.7$ so that scaling behaviour can be examined.

The work of this chapter was performed on $16^3 \times 24$ lattices at $\beta = 6.0$. 105 quenched configurations using the standard Wilson gluonic action were used, gauge fixed to Coulomb gauge with simulations beginning on 8 different origin sites and 4 different starting time slices per configuration as described in [32]. Equation (3.56), discussed in section (3.7), was used to evolve quark propagators.

4.1 Tuning the Bare Quark Mass

As discussed in Chapter 3, the parameters of NRQCD must be tuned to match experimental values. The inverse lattice spacing a^{-1} is determined by matching energy levels splittings to their experimental values. For this thesis an inverse lattice spacing of $a^{-1} = 2.59(5)$ GeV was used for the $\beta = 6.0$ simulation data which was obtained by matching the $1P - 1S$ dimensionless splitting to experiment. This work was carried out by [34]. The bare quark mass M_b^0 is determined as follows.

From experiment, there is evidence to show that spin-independent splittings

such as $1P-1S$ do not depend strongly on the bare quark mass M_b^0 [10, 31], however the spin-dependent splittings do [31]. For the hyperfine splitting ${}^3S_1 - {}^1S_0$, there are no experimental results, however it seems to be inversely proportional to M_b^0 from perturbation theory and at least roughly on the lattice [31]. So it is very important to tune this mass to its correct value.

As described in [31], the method for tuning the bare quark mass involves two simulations of the Υ meson in the ${}^3S_1$ channel. The first simulation is to compute the non-relativistic energy for the Υ's with small components of three-momenta, the other with zero momentum. The difference between these non-relativistic energies equals the kinetic energy of the meson

$$E_\Upsilon(\mathbf{p}) - E_\Upsilon(\mathbf{0}) = \frac{\mathbf{p}^2}{2M_{kin}} \tag{4.1}$$

where M_{kin} is called the kinetic mass. Hence the mass obtained is matched to the experimental Υ rest mass value of 9.46 GeV. This work was carried out in [31] and a dimensionless bare b quark mass of aM_b^0 =1.71 was found to give a kinetic Υ mass of 3.94(3) which when multiplied by a^{-1} =2.59(5) GeV gives a kinetic Υ mass of 9.5(4) GeV, which is equal to the experimental value within error.

4.2 Fitting Results for the D states

In this section multiple exponential fits are used to extract the ground and first excited states for the D states of the Υ meson which are listed in table (3.1) in section (3.9). These states are the ${}^1D_2T$, ${}^1D_2E$, ${}^3D_2T$, ${}^3D_2E$, ${}^3D_3S$ and ${}^3D_1$, where E and T label the two possible lattice cubic group representations for the ${}^1D_2$ and ${}^3D_2$ states. In principle at least, the E and T representations of the ${}^1D_2$ state should have the same ground state mass within errors, as should the E and T representations of ${}^3D_2$. Carrying out n multi exponential fits will give an accurate value for $n-1$ states with higher excited state contamination contained in the last exponential.

Before utilising the fitting methods outlined in section (3.13.1) the quality

of the data was assessed by looking at effective mass plots for all possible smearing combinations of each state. These plots were also used to determine the initial values for the fitting parameters to be input in the fitting routines. In figures (4.1) to (4.7) the effective masses are plotted for each of the D states studied for this thesis. Looking at figure (4.1) the effective masses are plotted against time t for every type of (source,sink) combination of the ${}^1D_2T$ state. The (loc,1), (1,loc) and (1,1) plots have reasonable plateaux which suggests that ground state smearing has worked. The (loc,2), (2,loc) and (2,2) plots show reasonable plateaux at low t indicating a first excited state, the signal then decays towards the ground state and is eventually lost in noise.

Table (4.1) shows results obtained from vector fits to the ${}^1D_2T$ ground state energy over various t_{min}/t_{max} ranges as well as the quality of the fit, Q. The upper part of the table involved shows the simplest possible fit - a single correlation function with $(n_{sc}, n_{sk}) = (1, loc)$ which was fitted to a single exponential ansatz of the form (3.88). It can be seen from the table that the ground state is steady over a large t_{min}/t_{max} and exhibits good, stable Q values down to $t_{min} = 4$. In general the best estimate for the ground state mass is taken to be given at the lowest t_{min} possible, corresponding to such a stable range of appropriate Q values shown in the table. Hence a good estimate of the ground state mass is indicated by the Q value of 0.49, giving 0.770(5) for the mass at $t_{min} = 4$. First and higher excited states can contaminate the ground state. In order to see if there is higher state contamination, two correlations fitted to two exponentials can be used instead of one to extract the ground state mass and give a rough estimate of the first excited state. It is often possible to obtain a good fit at a lower t_{min} using this method than in the simple single correlation fit. If this is the case, then the single correlation fit shows that the ground state has probably been contaminated by the first excited state at this lower time range. The two correlation fit is then usually considered to be the more accurate fit at the lower time range where higher state contamination has taken place for extracting the ground state mass, although as stated above the first excited state extracted from this fit is only a rough estimate since it may be contaminated by the second excited state. Even in

the cases where ground states extracted from single correlation vector fits cannot be relied upon, they still have value, as they can often be used to obtain estimates for energies and amplitudes for particular states with different smearings (n_{sc}, n_{sk}) and these amplitudes can be used as initial guesses for fits that are harder to perform, such as matrix fits.

The lower part of table (4.1) shows results obtained from a vector fit to the ${}^1D_2T$ ground and first excited state energies over various t_{min}/t_{max} ranges. The fit involved two correlation functions with $(n_{sc}, n_{sk}) = (1, loc)$ and $(2, loc)$ which were fitted to a two exponential ansatz. Again it can be seen that the ground state is reasonably steady at low t_{min}/t_{max}, and a good estimate is given at $t_{min} = 2$, giving 0.750(7) with Q value 0.42 and the first excited state is estimated by 0.987(9). As can be seen from the table, the inclusion of a second correlation and exponential to the fit allows the ground state mass to be extracted at a lower t_{min} than in the single correlation case, suggesting that the ground state was contaminated by the first excited state. Figure (4.2) shows plots of the ground state given by the one and two correlation vector fits. It can be seen clearly that the ground state from the two correlation fit is stable at low t_{min}. This is because any contamination from higher states is removed by the second exponential. This case contrasts clearly with the single correlation fit where the ground state can be seen to rise at low t_{min} due to the excited state, but at higher t_{min}, both fits are in agreement as expected. Table (4.2) shows results obtained from matrix fits to four ${}^1D_2T$ correlations with $(n_{sc}, n_{sk}) = (1,1)$, $(1,2)$, $(2,1)$ and $(2,2)$. It was generally harder to obtain reasonable Q values for matrix fits of the D states since the signals for the above correlations are lost in noise earlier than the (1,loc) correlation used in the vector fits, and so for this reason the time range over which the fitting took place was reduced slightly. However, a steady ground state can be seen over a reasonable t_{min}/t_{max} and the Q value of 0.10 corresponding to $t_{min} = 8$ indicates a good fit and gives an estimate of 0.740(31) for the ground state mass. The corresponding first excited state mass is estimated to be 0.812(40).

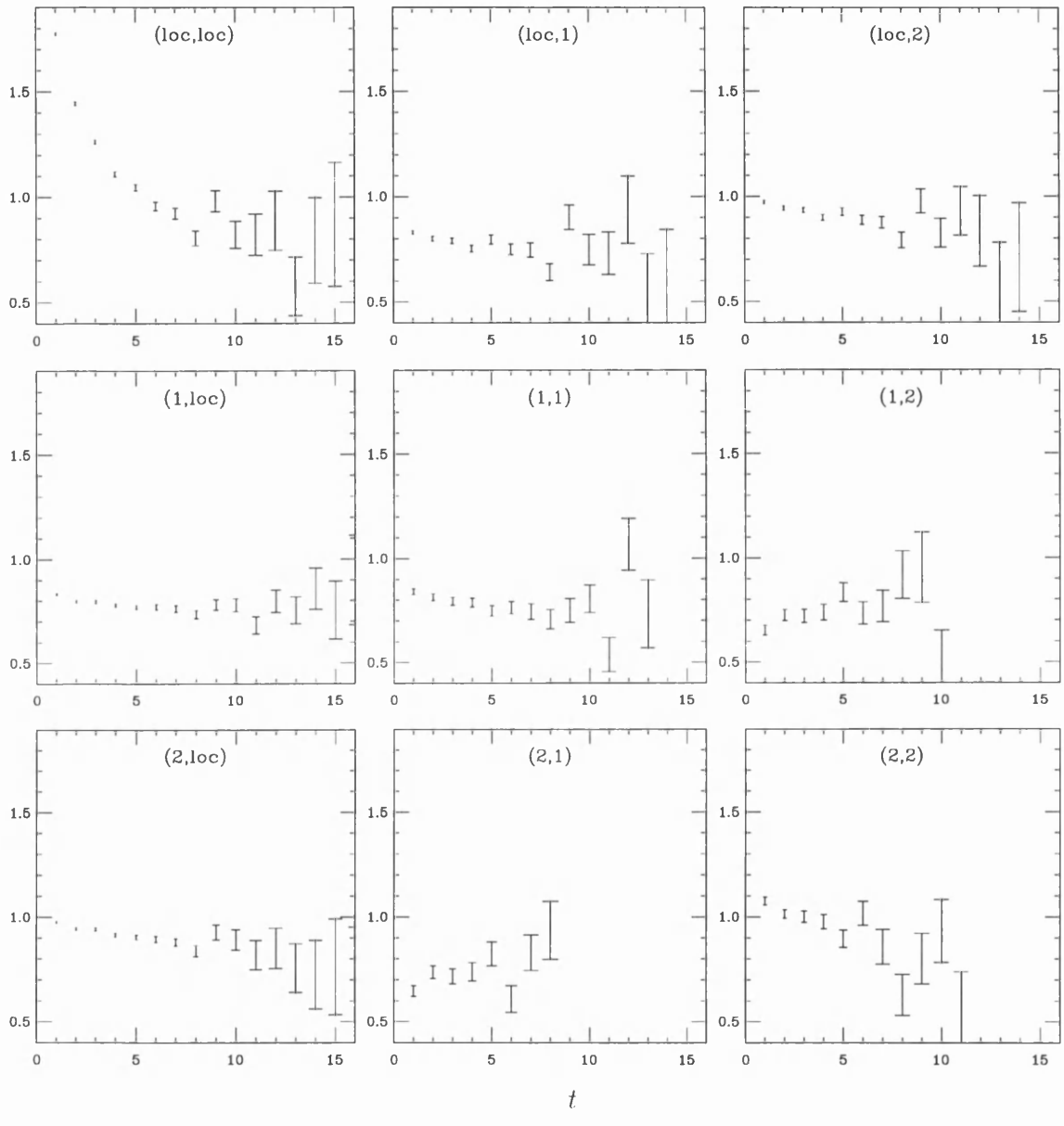

Figure 4.1: ${}^1D_2T$ Effective masses by (source,sink)

fit	N_{exp}	t_{min}/t_{max}	E_1	E_2	Q
fit to	1	3/16	0.779(4)		0.05
(1,loc)		4/16	0.770(5)		0.49
		5/16	0.766(6)		0.58
		6/16	0.763(7)		0.52
		7/16	0.759(8)		0.50
		8/16	0.756(11)		0.41
		9/16	0.767(15)		0.46
		10/16	0.759(18)		0.40
		11/16	0.750(23)		0.31
		12/16	0.788(31)		0.86
		13/16	0.785(43)		0.69
		14/16	0.818(70)		0.55
fits to (1,loc)	2	1/16	0.749(5)	0.996(7)	0.04
and (2,loc)		2/16	0.750(7)	0.987(9)	0.42
		3/16	0.753(9)	0.993(13)	0.36
		4/16	0.748(13)	0.960(18)	0.69
		5/16	0.754(17)	0.955(27)	0.59

Table 4.1: Vector fits to ${}^1D_2T$ with 1 and 2 exponentials.

fit	N_{exp}	t_{min}/t_{max}	E_1	E_2	Q
fits to	2	4/14	0.763(8)	0.959(22)	0.06
(1,1),(1,2)		5/14	0.754(10)	0.929(30)	0.04
(2,1),(2,2)		6/14	0.753(13)	0.912(44)	0.03
		7/14	0.733(24)	0.828(33)	0.08
		8/14	0.740(31)	0.812(40)	0.10
		9/14	0.755(23)	0.925(86)	0.15
		10/14	0.753(23)	1.055(161)	0.21
		11/14	0.750(35)	1.104(243)	0.09
		12/14	0.821(47)	1.398(189)	0.47

Table 4.2: Matrix fit to ${}^1D_2T$.s with 2 exponentials.

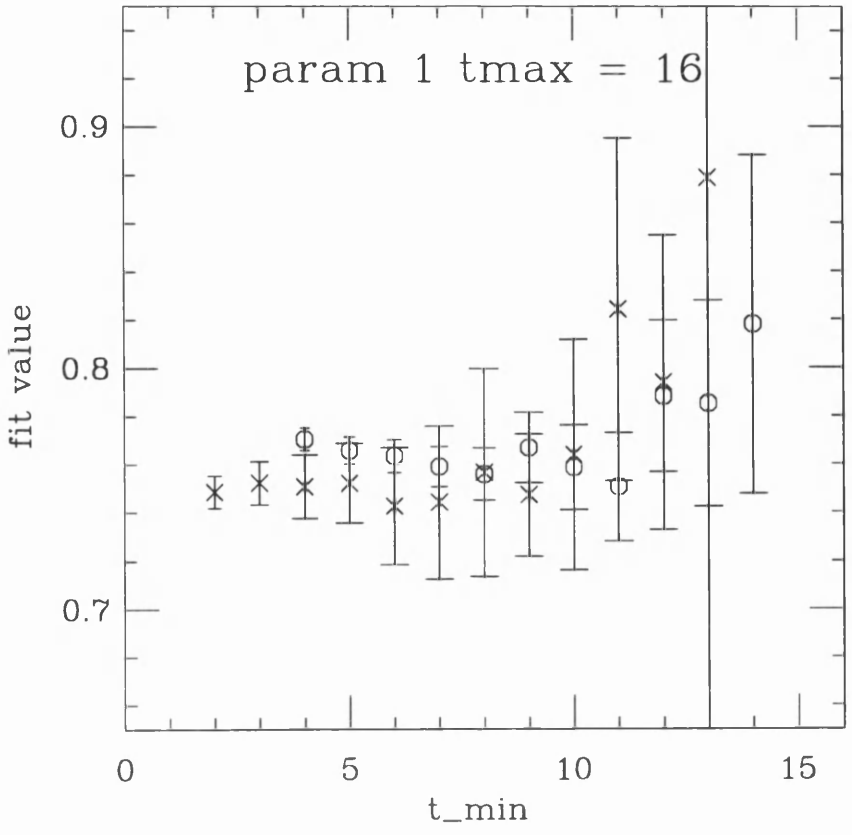

Figure 4.2: The circles show a 1 exponential fit while the crosses show a 2 exponential fit for the ${}^1D_2T$ state.

The results from similar vector fits carried out on the ${}^1D_2E$ ground state energies are shown in table (4.3). The upper part of the table shows a single $(1, loc)$ correlation fitted to a single exponential. As can be seen the ground state is steady over a large t_{min}/t_{max} and a good mass estimate is given at $t_{min} = 5$ of 0.741(7) with Q value of 0.42. As before, to see if there is any first excited state contamination, two correlations are fitted to two exponentials. This two correlation fit was hard to perform since it seemed sensitive to the initial fitting parameters given to the fitting routine and consequently most of the fits attempted (for different amplitudes, energies and t_{max}'s) had very poor Q values. The final and best fit shown in the lower half of the table shows acceptable ground state masses with

reasonably stable Q values. The best estimate of the ground state is indicated by $Q = 0.30$ at $t_{min} = 5$ giving 0.76(4) and the first excited state is estimated to be 0.86(5). However the amplitude (obtained from the fitting routine) for the overlap of the first excited state to the ground state was essentially zero (since it was 50 per cent smaller than it's error) suggesting that the two correlator functions are uncorrelated, i.e. smearing for the ground state is working well, so overlap with the first excited state is very small. This may explain why it was more difficult to perform this fit compared with the two correlation vector fit for ^1D_2T since more realistic initial fitting parameters had to be estimated in order to achieve convergence in the fitting routine, since the effective mass plot for $(1, loc)$ clearly shows that there is little overlap with $(2, loc)$. See figure (4.3). It is also evident from this figure that the $(2, loc)$ signal is lost in noise before it can decay to the ground state, c.f. (2,loc) plot in figure (4.1). It appears then, that the two correlation fit has not given any improvement in statistical accuracy over the single correlation fit, which in this case is believed to give the more reliable estimate of the ground state. Table (4.4) shows the matrix fit to the four ^1D_2E correlations $(1,1)$, $(1,2)$, $(2,1)$ and $(2,2)$. This state has a steady ground state and a good estimate is given at $t_{min} = 6$ as 0.757(14) with Q value of 0.76 and are consequently in agreement with the single correlation vector fit.

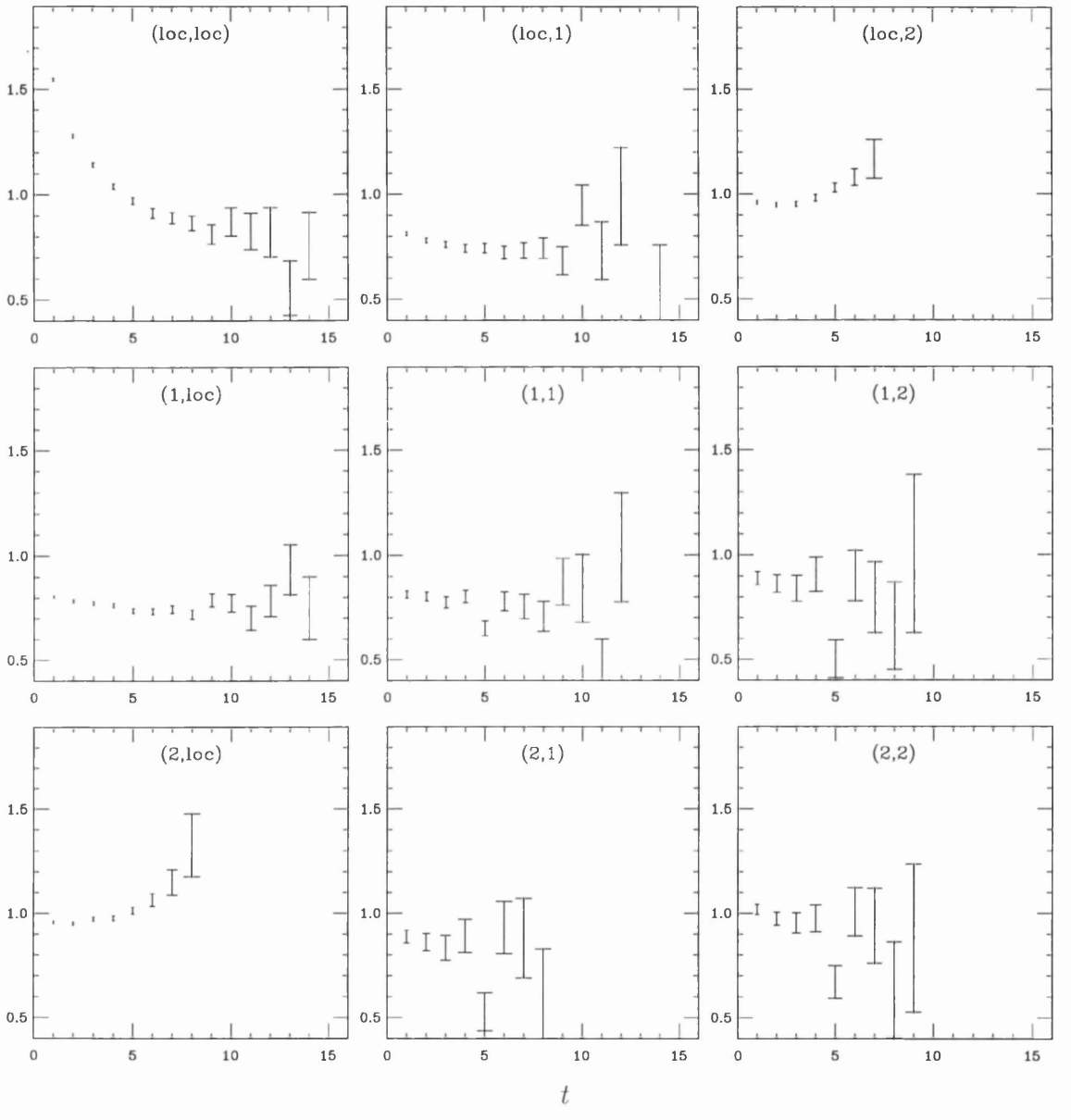

Figure 4.3: ${}^1D_2E$ Effective masses by (source,sink)

fit	N_{exp}	t_{min}/t_{max}	E_1	E_2	Q
fit to	1	3/14	0.758(5)		0.03
(1,loc)		4/14	0.749(6)		0.18
		5/14	0.741(7)		0.42
		6/14	0.742(8)		0.32
		7/14	0.748(11)		0.29
		8/14	0.751(13)		0.21
		9/14	0.775(19)		0.45
		10/14	0.768(25)		0.32
		11/14	0.767(35)		0.17
		12/14	0.829(56)		0.30
fits to (1,loc)	2	3/14	0.719(14)	0.890(16)	0.03
and (2,loc)		4/14	0.710(20)	0.869(22)	0.05
		5/14	0.762(35)	0.859(45)	0.30
		6/14	0.779(41)	0.859(56)	0.20
		7/14	0.784(53)	0.888(88)	0.11
		8/14	0.855(100)	0.904(141)	0.08
		9/14	0.758(69)	1.038(226)	0.06
		10/14	0.808(239)	1.031(737)	0.02

Table 4.3: Vector fits to ${}^1D_2E$ with 1 and 2 exponentials.

fit	N_{exp}	t_{min}/t_{max}	E_1	E_2	Q
fits to	2	1/12	0.770(6)	0.970(9)	0.00
(1,1),(1,2)		2/12	0.761(6)	0.942(11)	0.00
(2,1),(2,2)		3/12	0.753(8)	0.926(17)	0.03
		4/12	0.745(11)	0.885(22)	0.25
		5/12	0.732(15)	0.854(28)	0.24
		6/12	0.757(14)	0.898(57)	0.76
		7/12	0.805(56)	0.752(27)	0.83
		8/12	0.766(19)	0.725(103)	0.75
		9/12	0.781(26)	0.768(38)	0.68
		10/12	0.492(232)	0.758(43)	0.73

Table 4.4: Matrix fit to ${}^1D_2E$.s with 2 exponentials.

Table (4.5) shows the two vector fits applied to the ${}^3D_2T$ ground and first excited state energies. The upper part of the table shows a single correlation fit to one exponential and again shows a steady ground state over a large t_{min}/t_{max}. The Q value of 0.73 corresponding to a ground state mass of 0.747(8) at t_{min} =4 indicates a reasonable estimate. The lower part of the table shows the two correlation fit where it was also difficult to obtain reasonable Q values, since it was highly sensitive to the initial fitting parameters. After much variation of these parameters a final fit was obtained with reasonable ground state masses and stable Q values where a best estimate of the ground state is given by 0.75(4) at $t_{min} = 5$ with Q value 0.17. The corresponding first excited state is estimated to be 0.87(7), although once again the amplitude for the overlap of the first excited state with the ground state is essentially zero and the $(2, loc)$ effective mass plot in figure (4.4) shows that the first excited state signal is lost in noise before it can decay to the ground state. Again the single correlation fit is deemed more acceptable. Table (4.6) shows the corresponding matrix fit to the ${}^3D_2$ ground and first excited state energies, where a steady ground state is present and the best estimate is given by 0.770(18) at $t_{min} = 6$ with Q value 0.36 and the corresponding first excited state is estimated to be 0.99(10). The estimate for the ground state extracted from the matrix fit agrees within errors to the estimate extracted from the single correlation vector fit.

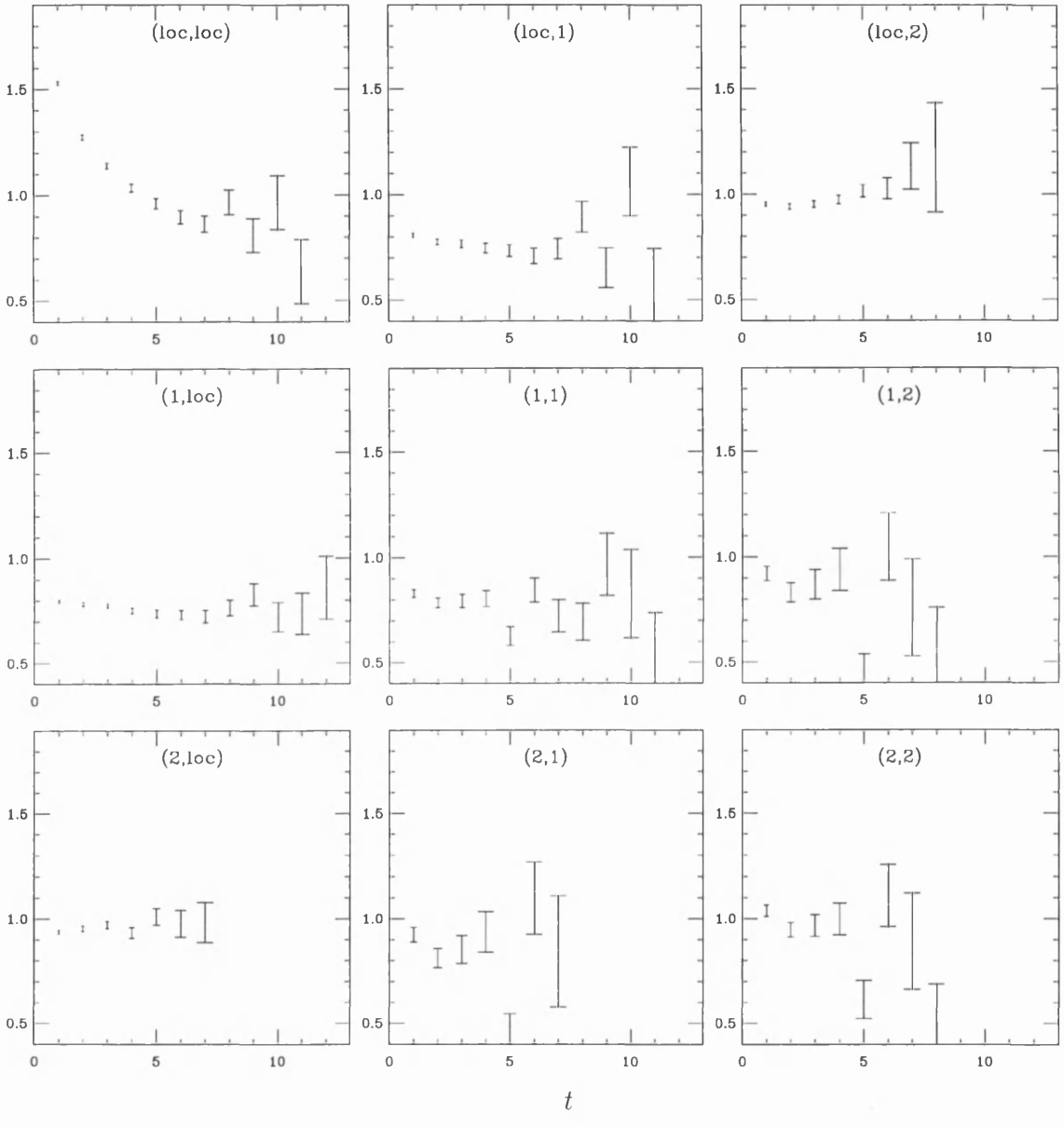

Figure 4.4: ${}^3D_2T$ Effective masses by (source,sink)

fit	N_{exp}	t_{min}/t_{max}	E_1	E_2	Q
fit to	1	1/12	0.777(4)		0.00
(1,loc)		2/12	0.767(5)		0.07
		3/12	0.757(6)		0.31
		4/12	0.747(8)		0.73
		5/12	0.743(10)		0.67
		6/12	0.745(12)		0.56
		7/12	0.754(17)		0.52
		8/12	0.773(23)		0.66
		9/12	0.774(35)		0.45
		10/12	0.723(51)		0.93
fits to (1,loc)		2/13	0.740(35)	0.868(42)	0.06
and (2,loc)	2	3/13	0.723(28)	0.856(37)	0.07
		4/13	0.712(35)	0.830(48)	0.10
		5/13	0.751(44)	0.870(73)	0.17
		6/13	0.711(75)	0.768(80)	0.17
		7/13	0.751(77)	0.870(126)	0.12
		8/13	0.866(105)	0.999(188)	0.44
		9/13	0.688(719)	0.859(***)	0.63
		10/13	0.751(207)	0.870(440)	0.36

Table 4.5: Vector fits to ${}^3D_2T$ with 1 and 2 exponentials.

fit	N_{exp}	t_{min}/t_{max}	E_1	E_2	Q
fits to	2	3/12	0.756(10)	0.937(23)	0.00
(1,1), (1,2)		4/12	0.751(13)	0.907(31)	0.01
(2,1), (2,2)		5/12	0.745(18)	0.881(39)	0.05
		6/12	0.770(18)	0.989(96)	0.36
		7/12	0.746(36)	0.828(83)	0.43
		8/12	0.744(86)	0.809(74)	0.28
		9/12	0.753(49)	1.234(484)	0.82
		10/12	0.584(398)	0.695(105)	0.77

Table 4.6: Matrix fit to ^3D_2T.s with 2 exponentials.

Table (4.7) shows vector fits to the ^3D_2E ground and first excited state energies. Again the upper part of the table shows a one correlation fit and it also displays steady estimates of the ground state masses which have a steady Q values over a large t_{min}/t_{max} range. The Q value of 0.87 signals a good estimate of 0.776(6) at t_{min} =4. The lower part of the table shows the two correlation, two exponential fit and this too displays a steady ground state of which a good estimate is indicated at Q value of 0.32 of 0.763(11) at t_{min}=2 and the corresponding first excited state is estimated by 0.98(1). Table (4.8) shows the matrix fit to the ^3D_2E ground and first excited state. Again there is a steady ground state over a large t_{min}/t_{max} and a good estimate is given at t_{min} = 2 giving 0.786(7) with Q value 0.21 and the first excited state is estimated to be 1.01(1). The estimate for the ground state extracted from the matrix fit agrees within errors to the estimate extracted from the single correlation vector fit.

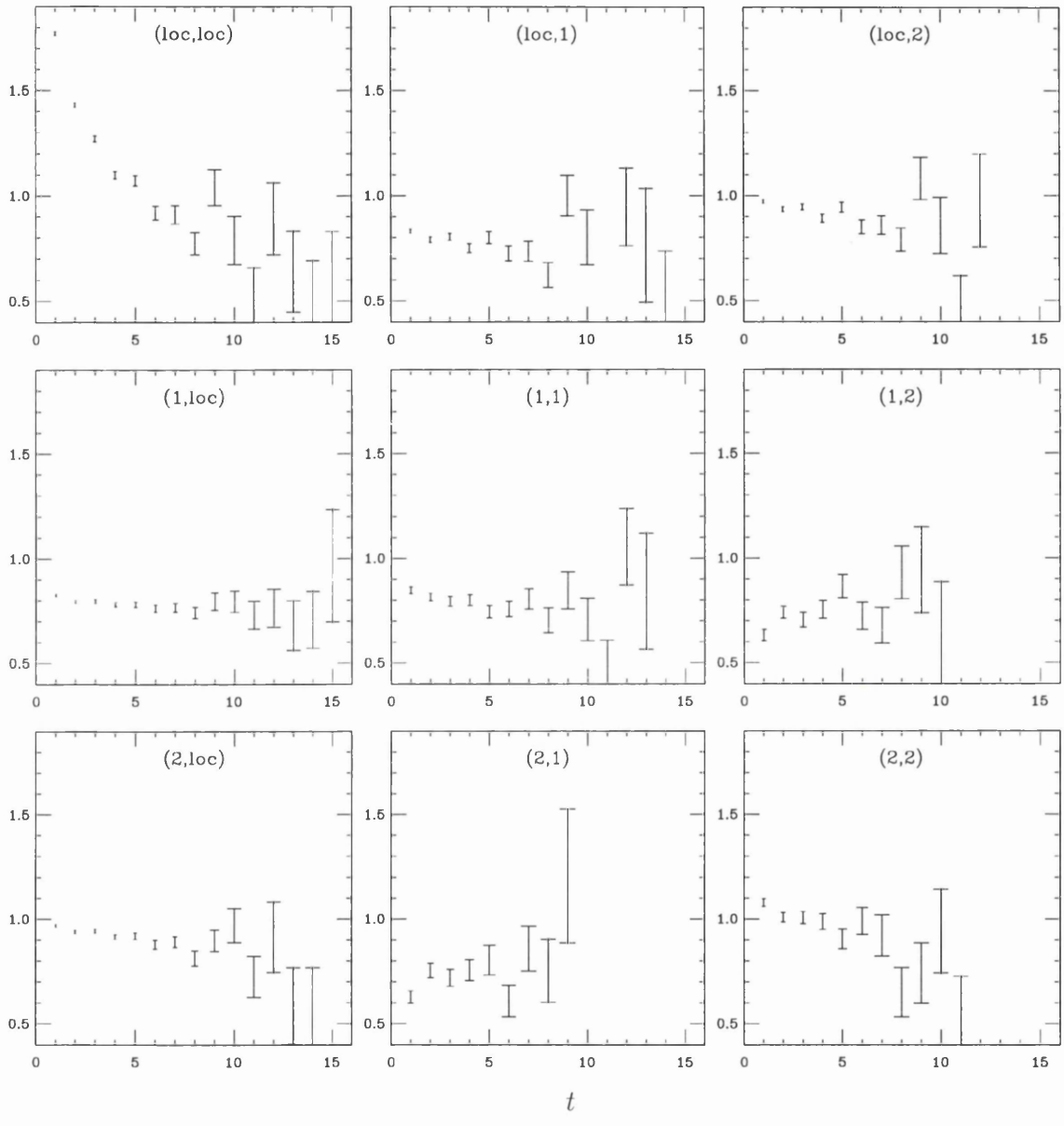

Figure 4.5: ${}^3D_2E$ Effective masses by (source,sink)

fit	N_{exp}	t_{min}/t_{max}	E_1	E_2	Q
fit to	1	1/15	0.801(4)		0.00
(1,loc)		2/15	0.788(4)		0.44
		3/15	0.784(5)		0.52
		4/15	0.776(6)		0.87
		5/15	0.771(8)		0.89
		6/15	0.764(9)		0.95
		7/15	0.764(13)		0.90
		8/15	0.762(16)		0.84
		9/15	0.772(22)		0.81
		10/15	0.754(29)		0.83
		11/15	0.725(38)		0.94
		12/15	0.717(53)		0.84
		13/15	0.686(75)		0.86
fits to (1,loc)	2	1/15	0.780(12)	0.972(12)	0.00
and (2,loc)		2/15	0.763(11)	0.978(13)	0.32
		3/15	0.751(12)	1.005(17)	0.44
		4/15	0.747(17)	0.989(25)	0.50
		5/15	0.754(22)	1.016(42)	0.51
		6/15	0.754(34)	0.970(65)	0.46
		7/15	0.769(49)	0.987(114)	0.33
		8/15	0.730(67)	0.963(132)	0.27

Table 4.7: Vector fits to ^3D_2E with 1 and 2 exponentials.

fit	N_{exp}	t_{min}/t_{max}	E_1	E_2	Q
fits to	2	1/9	0.800(5)	1.040(10)	0.01
(1,1),(1,2)		2/9	0.786(7)	1.009(13)	0.21
(2,1),(2,1)		3/9	0.779(8)	1.008(20)	0.21
		4/9	0.773(11)	0.969(27)	0.17
		5/9	0.761(15)	0.943(39)	0.13
		6/9	0.768(18)	0.977(74)	0.13
		7/9	0.753(48)	0.827(83)	0.07
		8/9	0.757(39)	0.494(225)	0.42

Table 4.8: Matrix fit to ^3D_2E.s with 2 exponentials.

Table (4.9) shows the two vector fits that were applied to the ^3D_3S ground and first excited state energies. As before the upper part of the table shows the single correlation fit to the ground state again showing a steady range of ground state mass estimates over large t_{min}/t_{max}. A good estimate is given at $t_{min} = 4$ of 0.781(6) with Q value 0.60. The lower part of the table shows the two correlation fit to the ground state and also shows a steady range of values over large t_{min}/t_{max}, where a good estimate is given at t_{min} =3 of 0.760(15) with Q value 0.70 and the first excited state is estimated to be 1.01(2). Table (4.10) shows the matrix fit to the ^3D_3S ground and first excited state energies. There is a steady ground state with reasonable Q values and a good estimate is indicated by the Q value 0.17 given at $t_{min} = 2$ of 0.789(7) and the first excited state is estimated by 1.01(1).

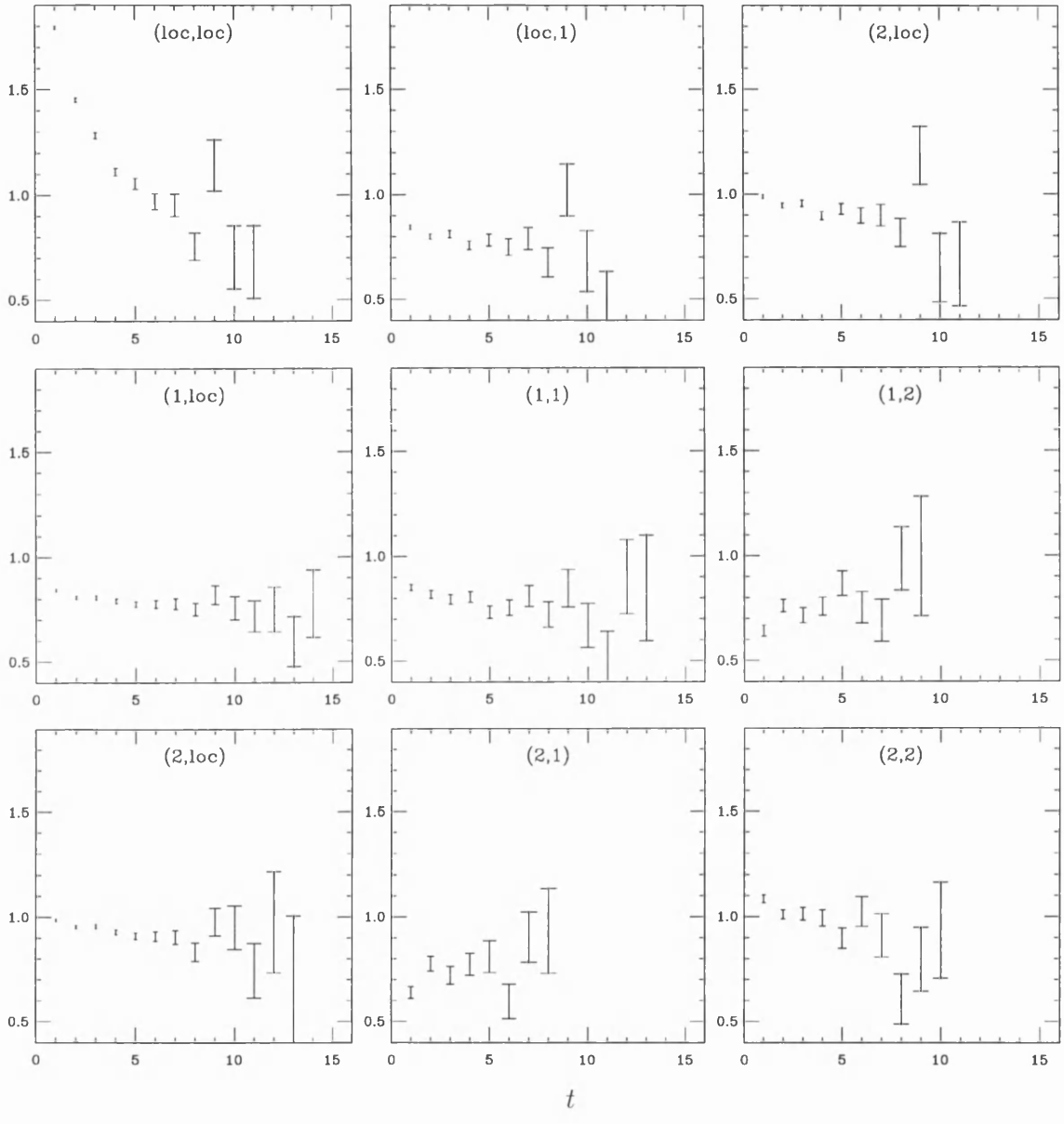

Figure 4.6: ${}^3D_3S$ Effective masses by (source,sink)

fit	N_{exp}	t_{min}/t_{max}	E_1	E_2	Q
fit to	1	2/14	0.798(4)		0.08
(1,loc)		3/14	0.791(5)		0.19
		4/14	0.781(6)		0.60
		5/14	0.773(8)		0.74
		6/14	0.771(10)		0.65
		7/14	0.766(14)		0.57
		8/14	0.759(19)		0.48
		9/14	0.761(26)		0.34
		10/14	0.724(31)		0.66
		11/14	0.699(43)		0.61
		12/14	0.674(67)		0.38
fits to (1,loc)	2	1/14	0.781(12)	0.979(13)	0.00
and (2,loc)		2/14	0.781(15)	0.979(17)	0.39
		3/14	0.760(15)	1.009(19)	0.70
		4/14	0.745(20)	0.971(26)	0.84
		5/14	0.757(31)	0.965(45)	0.76
		6/14	0.738(40)	0.959(62)	0.65
		7/14	0.702(56)	0.935(82)	0.56
		8/14	0.609(78)	0.890(76)	0.62

Table 4.9: Vector fits to ^3D_3S with 1 and 2 exponentials.

fit	n_{exp}	t_{min}/t_{max}	E_1	E_2	Q
fits to	2	1/9	0.804(6)	1.042(10)	0.01
(1,1), (1,2)		2/9	0.789(7)	1.008(13)	0.17
(2,1), (2,2)		3/9	0.780(9)	1.007(20)	0.21
		4/9	0.772(11)	0.970(26)	0.18
		5/9	0.758(16)	0.942(37)	0.11
		6/9	0.770(20)	0.968(72)	0.07
		7/9	0.725(88)	0.802(46)	0.07
		8/9	0.769(40)	0.431(220)	0.92

Table 4.10: Matrix fit to ^3D_3S.s with 2 exponentials.

Table (4.11) shows the two vector fits for the $^3D_1$ ground and first excited state energies. Again the upper part of the table shows the single correlation fit, and it displays steady estimates of the ground state masses which have steady Q values over a large t_{min}/t_{max} range. The Q value of 0.90 indicates an estimate of 0.749(6) for the ground state at t_{min}=5. The lower part of the table shows the two correlation vector fit and this exhibits a steady ground state down t_{min} of 2. A good estimate is indicated by the Q value 0.50 of 0.740(17) at t_{min}=4 and the corresponding first excited state is estimated to be 0.91(2). Table (4.12) shows the matrix fit applied to the $^3D_1$ ground and first excited states, where a ground state mass can be extracted from t_{min}=9 upwards. The best value is given by 0.72(3) with Q value 0.11 at t_{min}=9 and the first excited state is estimated to be 0.85(11). The estimate for the ground state extracted from the matrix fit agrees within errors to the estimate for the ground state extracted from the two correlation fit.

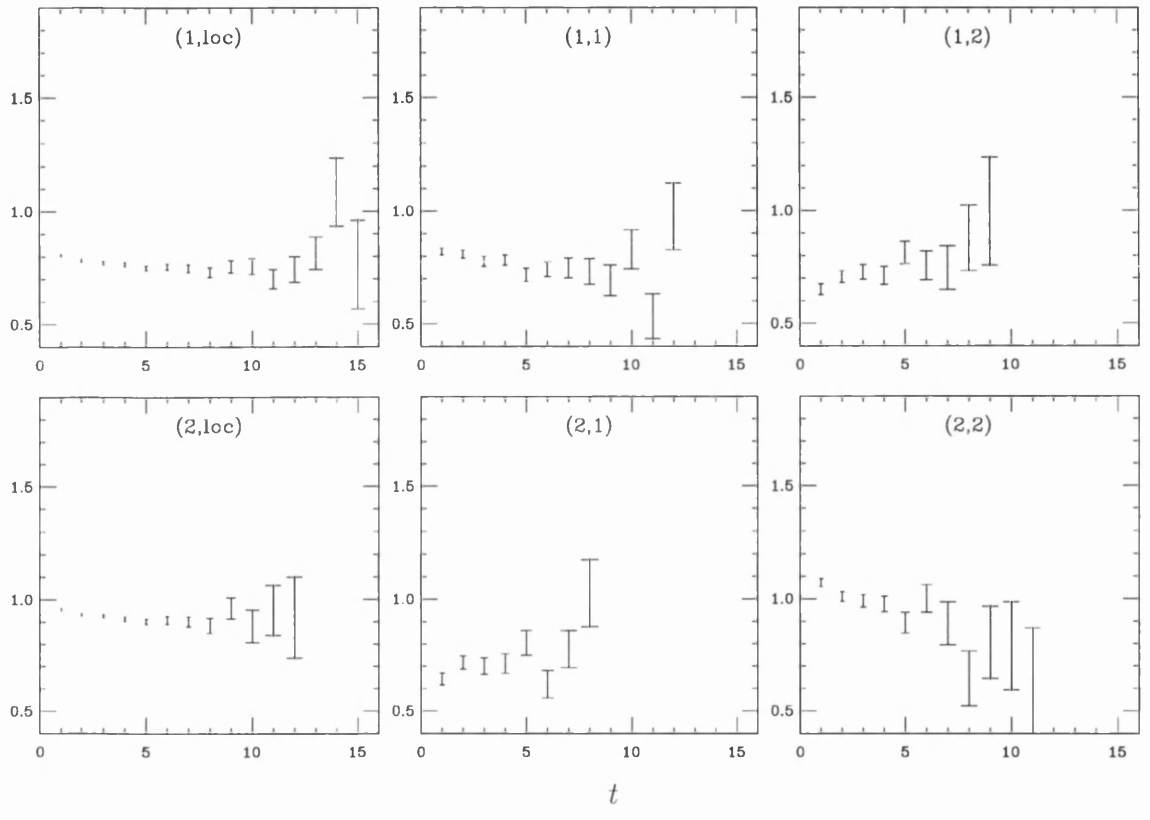

Figure 4.7: ${}^3D_1$ Effective masses by (source,sink)

fit	N_{exp}	t_{min}/t_{max}	E_1	E_2	Q
fit to	1	1/14	0.781(3)		0.00
(1,loc)		2/14	0.769(3)		0.05
		3/14	0.762(4)		0.34
		4/14	0.755(5)		0.73
		5/14	0.749(6)		0.90
		6/14	0.748(8)		0.84
		7/14	0.743(9)		0.84
		8/14	0.741(12)		0.75
		9/14	0.747(15)		0.69
		10/14	0.742(19)		0.56
		11/14	0.735(26)		0.38
		12/14	0.770(41)		0.43
fits to (1,loc)	2	1/15	0.741(6)	0.957(8)	0.03
and (2,loc)		2/15	0.737(8)	0.947(10)	0.29
		3/15	0.743(11)	0.941(14)	0.25
		4/15	0.740(17)	0.908(21)	0.50
		5/15	0.748(23)	0.901(31)	0.45
		6/15	0.753(33)	0.887(48)	0.32
		7/15	0.762(42)	0.895(73)	0.21
		8/15	0.796(59)	0.915(119)	0.17
		9/15	0.809(96)	0.966(238)	0.12

Table 4.11: Vector fits to $^3D_1$ with 2 exponentials.

fit	N_{exp}	t_{min}/t_{max}	E_1	E_2	Q
fits to	2	7/13	0.727(23)	0.850(52)	0.00
(1,1), (1,2)		8/13	0.706(41)	0.793(47)	0.00
(2,1), (2,2)		9/13	0.721(32)	0.845(111)	0.11
		10/13	0.727(31)	0.912(202)	0.15
		11/13	0.686(71)	0.948(278)	0.16

Table 4.12: Matrix fit to ${}^3D_1$.s with 2 exponentials.

State	Vector fit	Matrix fit
${}^3D_3S$	0.760(15)	0.789(7)
${}^3D_2E$	0.763(11)	0.786(7)
${}^3D_2T$	0.747(8)	0.770(18)
${}^1D_2E$	0.741(7)	0.757(14)
${}^1D_2T$	0.750(7)	0.740(13)
${}^3D_1$	0.740(17)	0.72(3)

Table 4.13: Comparison of results obtained from vector and matrix fitting method

To conclude this section table (4.13) summarises the results obtained for vector and matrix fits. As can be seen, the errors are quite high, although any discrepancies between vector and matrix fits for a particular state are not more than 2 sigma.

4.3 Fitting Results for Spin Splittings

Spin splittings for S, P and D states etc., arise from terms in the Lagrangian (3.30) which involve the spin $\boldsymbol{\sigma}$,

$$-c_3\frac{g}{8(M_b^0)^2}\boldsymbol{\sigma}\cdot(\boldsymbol{\Delta}\times\mathbf{E}-\mathbf{E}\times\boldsymbol{\Delta}) \qquad \text{and} \qquad -c_4\frac{g}{M_b^0}\boldsymbol{\sigma}\cdot\mathbf{B} \tag{4.2}$$

The first term gives rise to the P and D state fine structure, while the second accounts for the hyperfine S splitting. For this thesis, only the D state spin splittings were examined, and consequently only the first term is of interest here. An order of magnitude for the first term can be made following the arguments of section (3.3). The couplings are set to tree-level values, $c_3 = c_4 = 1$, and putting $\boldsymbol{\sigma} = 1/2$ and $M_b^0 \sim M$, the spin term is evaluated as

$$-c_3\frac{g}{8(M_b^0)^2}\boldsymbol{\sigma}\cdot(\boldsymbol{\Delta}\times\mathbf{E}-\mathbf{E}\times\boldsymbol{\Delta}) \sim \frac{Mv^4}{16} \tag{4.3}$$

Taking the dimensionless mass as aM=1.71 and $v^2 \sim 0.1$, the spin term has a dimensionless order of magnitude 0.001. As can be seen from tables (4.1) to (4.12) the typical error for ground state masses for both vector and matrix fits would not be able to distinguish these splittings adequately. To get around this problem, one can take advantage of the fact that meson correlation functions with the same orbital angular momentum but differing spin orientation, can be highly correlated. This allows a direct fit to the splitting between them, using a single exponential of the form

$$\text{Ratio(t)} = Ae^{-\delta Et} \tag{4.4}$$

Where δE is the difference between the ground state energies of both the mesons involved. The method is known as ratio fitting and has the advantage of reducing statistical errors because the high correlation between the numerator and denominator is divided out.

In the attempt to evaluate the D state splittings, advantage was taken of the maximum correlation between particular polarisations of lattice representations for D states obtained from the same source state. For example the ${}^1D_2Txy$ polarisation is formed from the spin/spatial symmetry matrix $\Gamma = D_{xy}$. The

^1D_2Txy state will be maximally correlated with the following particular polarisations consisting of the ^3D_2Ex state having $\Gamma = D_{zx}\sigma_y - D_{xy}\sigma_z$, the ^3D_2Ey state having $\Gamma = D_{xy}\sigma_z - D_{yz}\sigma_x$ and ^3D_3S state having $\Gamma = (D_{xy}\sigma_z + D_{yz}\sigma_x + D_{zx}\sigma_y)/3$ (see table (3.1)). Since the initial source spinors only have an upper spin component and since the action of σ_z preserves this, the above mentioned states will be maximally correlated with the particular polarisation of ^1D_2Txy. Using similar arguments, it is possible to work out which other polarisation states are maximally correlated.

From the potential models discussed in Chapter 2, it is expected that the D state spin splittings will not be as large as those for the P states. The study by [12] predicted the D state masses to be $^3D_1$ 10.120, $^3D_2$ 10.126, $^1D_2$ 10.127 and $^3D_3$ 10.130 GeV respectively, giving an average splitting of around 4 MeV. The average splittings for the P states are found experimentally to be around 20 MeV [10]. From another study of the Υ meson using NRQCD [32], splittings of around 0.007 in lattice units were found for the P states at $\beta = 6.0$. This means that we can probably expect the splittings for the D states to be roughly around 0.003 in lattice units. Unfortunately this is below the statistical error in a lot of the ratio fits carried out for this thesis.

Despite the fact that the ratio fits cannot be used to accurately determine the spin splittings for the D states, they can be used to help establish the order of the states. For example from the results of ratio fits, it seemed true that the $^3D_2$ and $^1D_2$ were heavier than the $^3D_1$ state (tables (4.14), (4.15) and (4.16)). The $^3D_3$ was heavier than the ^3D_2E (tables (4.17) and (4.18)), however the ratio fit of $^3D_3$ to ^1D_2T looks strange (table (4.19)).

Of the remaining possible fits (i.e. the ratio fits for $^3D_2$ to $^1D_2$) there were some problems with the $^3D_2$ and $^1D_2$ states. It was originally thought that these problems could be due to discretisation errors or finite volume effects. Finite volume effects would probably effect all of the D states together since they are of similar size. Discretisation errors will act to split the T representation from the E representation for both the $^1D_2$ and $^3D_2$ states. As an example of the problems encountered table (4.20) shows the results for a ratio fit for the

fit	n_{exp}	t_{min}/t_{max}	E_1	Q
(1,loc)	1	2/13	0.0082(15)	0.13
		3/13	0.0078(22)	0.09
		4/13	0.0029(32)	0.22
		5/13	0.0068(46)	0.24
		6/13	0.011(7)	0.22
		7/13	0.019(9)	0.22
		8/13	0.038(14)	0.58
		9/13	0.041(20)	0.42
		10/13	0.036(29)	0.25
		11/13	0.044(45)	0.10

Table 4.14: Ratio fit to ${}^3D_2 Tyz$-${}^3D_1 x$ with 1 exponential.

fit	n_{exp}	t_{min}/t_{max}	E_1	Q
(1,loc)	1	1/15	0.0114(9)	0.11
		2/15	0.0089(14)	0.26
		3/15	0.0098(24)	0.21
		4/15	0.027(34)	0.78
		5/15	−0.0026(49)	0.89
		6/15	−0.0065(66)	0.90
		7/15	−0.0063(89)	0.84

Table 4.15: Ratio fit to ${}^3D_2 Tzx$-${}^3D_1 y$ with 1 exponential.

fit	n_{exp}	t_{min}/t_{max}	E_1	Q
(1,loc)	1	1/14	0.0208(11)	0.00
		2/14	0.0141(16)	0.27
		3/14	0.0120(21)	0.34
		4/14	0.0077(28)	0.69
		5/14	0.0075(38)	0.60
		6/14	0.0101(53)	0.55
		7/14	0.0173(73)	0.72
		8/14	0.024(10)	0.75
		9/14	0.033(14)	0.77

Table 4.16: Ratio fit to ${}^1D_2Eyz$-${}^3D_1z$ with 1 exponential.

fit	n_{exp}	t_{min}/t_{max}	E_1	Q
(1,loc)	1	2/15	0.0106(3)	0.42
		3/15	0.0082(20)	0.55
		4/15	0.0053(30)	0.63
		5/15	0.0016(42)	0.69
		6/15	0.0075(61)	0.78
		7/15	0.0051(87)	0.71
		8/15	0.004(12)	0.64
		9/15	−0.005(16)	0.54
		10/15	−0.023(20)	0.69
		11/15	−0.006(28)	0.69
		12/15	0.012(43)	0.57

Table 4.17: Ratio fit to ${}^3D_3S$-${}^3D_2Ex$ with 1 exponential.

fit	n_{exp}	t_{min}/t_{max}	E_1	Q
(1,loc)	1	2/15	0.0112(13)	0.12
		3/15	0.0066(20)	0.67
		4/15	0.0048(29)	0.64
		5/15	0.0018(42)	0.65
		6/15	0.0096(61)	0.89
		7/15	0.0045(87)	0.89
		8/15	0.0032(125)	0.81
		9/15	−0.0052(168)	0.78
		10/15	−0.021(23)	0.83

Table 4.18: Ratio fit to ^3D_3S-^3D_2Ey with 1 exponential.

fit	n_{exp}	t_{min}/t_{max}	E_1	Q
(1,loc)	1	1/14	−0.0068(3)	0.00
		2/14	−0.0037(5)	0.08
		3/14	−0.0026(8)	0.16
		4/14	−0.0014(11)	0.20
		5/14	−0.0014(17)	0.14
		6/14	−0.00006(238)	0.11
		7/14	0.0013(34)	0.08
		8/14	0.0002(50)	0.05
		9/14	0.097(72)	0.11

Table 4.19: Ratio fit to ^3D_3S-^1D_2Txy with 1 exponential.

fit	n_{exp}	t_{min}/t_{max}	E_1	Q
(1,loc)	1	1/14	0.022(3)	0.38
		2/14	0.022(3)	0.31
		3/14	0.030(5)	0.78
		4/14	0.032(6)	0.72
		5/14	0.037(8)	0.73
		6/14	0.029(11)	0.77
		7/14	0.022(16)	0.72
		8/14	0.021(22)	0.60
		9/14	0.016(29)	0.46
		10/14	0.024(43)	0.31

Table 4.20: Ratio fit to ^3D_2Ex-^1D_2Eyz with 1 exponential.

$^3D_2Ex-{}^1D_2Eyz$ splitting, which seems to show that the ^3D_2E is heavier than the ^1D_2E by something like 0.02. This is a much bigger splitting than expected and probably in the wrong direction (the potential model predictions have $^1D_2$ heavier than $^3D_2$). Similar results were found for ratio fits using different polarisations of ^3D_2E and ^1D_2E. When the ratio fits with the T representation were examined, it was very unclear whether $^1D_2$ or $^3D_2$ was heavier.

In an attempt to determine whether the problems outlined above arose from finite volume effects or discretisation errors, ratio fits were carried out for the E to T representation for the $^3D_2$ and $^1D_2$ states respectively. For the the case of $^1D_2$ it seems pretty clear that the E representation is split from the T and that all of the ^1D_2T states (i.e ^1D_2Txy, Tyz and Tzx) have the same mass as each other. Similarly the ^1D_2E states (i.e. ^1D_2Exy and ^1D_2Eyz seem to have the same mass as each other. This is exactly what one would expect from discretisation errors. The splittings found for each of the possible ratio fits seem quite high and are all very similar, around 0.01-0.02, putting the ^1D_2T above the ^1D_2E. See table (4.21) for an example. It is unclear why these discretisation errors were not

fit	n_{exp}	t_{min}/t_{max}	E_1	Q
(1,loc)	1	1/14	0.020(2)	0.70
		2/14	0.019(3)	0.67
		3/14	0.021(4)	0.66
		4/14	0.022(5)	0.57
		5/14	0.025(7)	0.51
		6/14	0.017(10)	0.55
		7/14	0.014(14)	0.45
		8/14	0.006(18)	0.38
		9/14	0.07(24)	0.34

Table 4.21: Ratio fit to ${}^1D_2Txy$-${}^1D_2Exy$ with 1 exponential.

observed for the P state splittings. One possibility may be that the D states are more sensitive to the errors that appear, perhaps because they are more squeezed in the volume.

For the ${}^3D_2$ case, it is not as clear. There seems to be a splitting within the ${}^3D_2T$ representation itself with ${}^3D_2Txy$ lighter than the others. It is unclear why this should happen, though it may be related to the fact that the ${}^3D_2Txy$ is unusual in that it has the same source as the ${}^1D_2E$ states. All of the other ${}^3D_2$ states overlap with ${}^1D_2T$ at the source. So the ${}^3D_2Txy$ may look a bit like a ${}^1D_2E$ which is below the ${}^1D_2$ (from the discussion in the paragraph above). Apart from that, there is no obvious sign of splitting for the ${}^3D_2$ state, in that ${}^3D_2Ex$ and Ey seem to match well to ${}^3D_2Tyz$ and Tzx.

If the problems examined here are due to discretisation errors it is important to discuss how improvements can be made to achieve better results. There is a choice of going to a finer lattice which is costly or further improving the NRQCD action. How this is carried out is investigated in [20], and has been implemented by [33] for S and P states. This would allow someone to repeat these results but with smaller discretisation errors. They would probably also need higher

statistics and perhaps a bigger spatial volume and none of these implementations would be possible on a finer lattice without utilising massive computer resources.

4.4 Upsilon D States at $\beta = 5.7$

In addition to the study of the D states at $\beta = 6.0$, the $^1D_2$ state was also studied on a coarser lattice, with a spacing of $\beta = 5.7$. This work was performed on $12^3 \times 24$ lattices with 42 quenched configurations using the standard Wilson gluonic action. The simulation began on 8 different spatial origin sites and 2 different starting time slices per configuration. The inverse lattice spacing used in this thesis for $\beta = 5.7$ was taken from [34] and is given by $a^{-1} = 1.41(4)$ GeV.

Only two smearings were available for the $^1D_2$, (1,loc) and (1,1), which meant only single exponential fits were possible. Figure (4.8) shows the effective mass plots for both smearings, with both plots showing plateaux indicating a ground state for the $^1D_2$

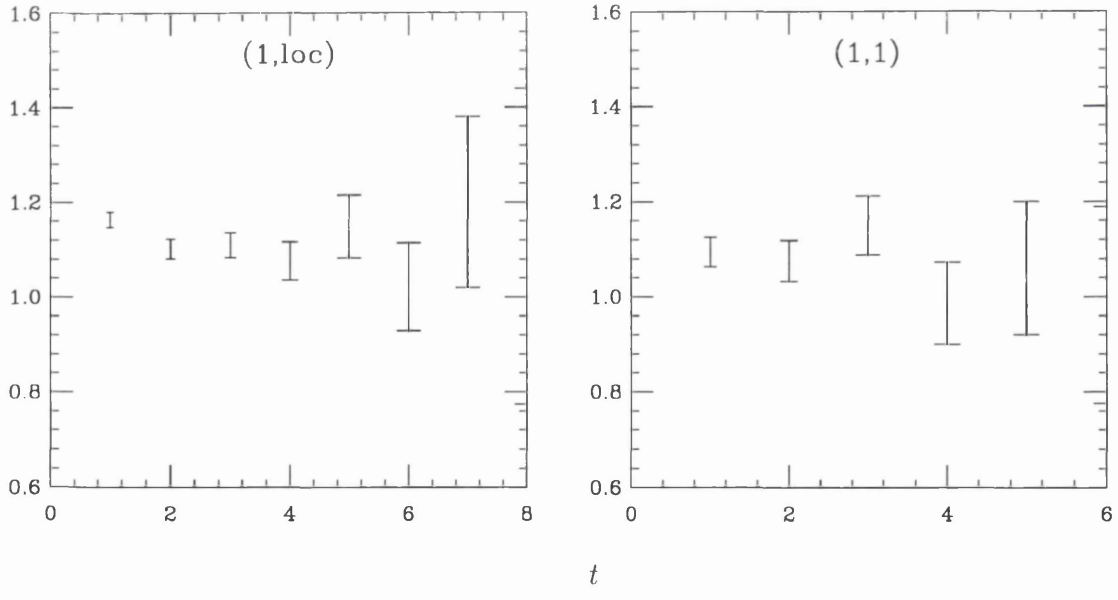

Figure 4.8: $^1D_2$ Effective masses by (source,sink)

Table (4.22) shows the results of the single exponential fit to the $^1D_2$ state

with (1,loc) smearing and it shows the presence of a steady ground state over a reasonable t_{min}/t_{max}. The Q value of 0.87 corresponding to a ground state of 1.103(14) at $t_{min} = 2$ indicates a reasonable estimate.

Table (4.23) shows the results of the single exponential fit to the $^1D_2$ state with (1,1) smearing. This also shows the presence of a steady ground state over a reasonable t_{min}/t_{max}. The Q value 0.69 corresponding to a ground state mass of 1.084(24) at $t_{min} = 2$ indicates a reasonable estimate.

fit	N_{exp}	t_{min}/t_{max}	E_1	Q
fit to	1	1/9	1.128(11)	0.27
(1,loc)		2/9	1.103(14)	0.93
		3/9	1.099(19)	0.87
		4/9	1.084(28)	0.85
		5/9	1.103(44)	0.81
		6/9	1.081(66)	0.67
		7/9	1.175(143)	0.73

Table 4.22: Vector fit to $^1D_2$ with 1 exponential.

4.5 Scaling of Results

The dimensionless ground state mass for $^1D_2$ at $\beta = 5.7$ can be used to obtain a dimensionless splitting with the $^3S_1$ ground state mass predicted at $\beta = 5.7$ in an earlier work carried out by [29]. Here the ground state mass of the $^3S_1$ was found to be 0.5187(6). This gives a dimensionless splitting of $1^1D_2 - 1^3S_1 = 0.584(14)$ in lattice units, where the value of 1.103(14) from the $(1, loc)$ fit was taken as the best value for 1^1D_2. In order to make this splitting dimensionful so that the scaling at $\beta = 5.7$ can be compared with $\beta = 6.0$ predictions, it must be multiplied by the inverse lattice spacing for $\beta = 5.7$ of $a^{-1} = 1.41(4)$ GeV. This gives the splitting as 0.823(31) GeV.

fit	N_{exp}	t_{min}/t_{max}	E_1	Q
fits to	1	1/8	1.091(17)	0.78
(1,1)		2/8	1.084(24)	0.69
		3/8	1.083(36)	0.55
		4/8	1.033(53)	0.63
		5/8	1.078(85)	0.55
		6/8	1.113(152)	0.29

Table 4.23: Vector fit to $^1D_2$ with 1 exponential.

A similar calculation to that above can be used for the $\beta = 6.0$ predictions of section (4.2). In this case the ground state mass of the $^3S_1$ state is taken as 0.4534(8), from the earlier work of [31]. The dimensionless splitting is given by $1^1D_2 - 1^3S_1 = 0.294(5)$, where an average has been taken for the $^1D_2$ predictions listed in table (4.13). Again to make this splitting dimensionful it must be multiplied by the inverse lattice spacing for $\beta = 6.0$ of $a^{-1} = 2.59(5)$ GeV, giving the splitting as 0.761(20) GeV.

As can be seen from the two splittings from the different lattice spacings there is some sign of lack of scaling. However only single exponential fits could be carried out for $\beta = 5.7$ as the $(2, loc)$ smearings etc. were not available, so this could be the reason for the problem. Figure (4.9) shows a graph of the two splittings against a^2.

As can be seen from the graph the scaling is not too bad and we can conclude that lack of scaling indicates that the continuum result is smaller than either result. Though of course a cannot be taken to zero in NRQCD (because of the non-renormalisable interactions) so in principle we have to improve the action until this plot is flat.

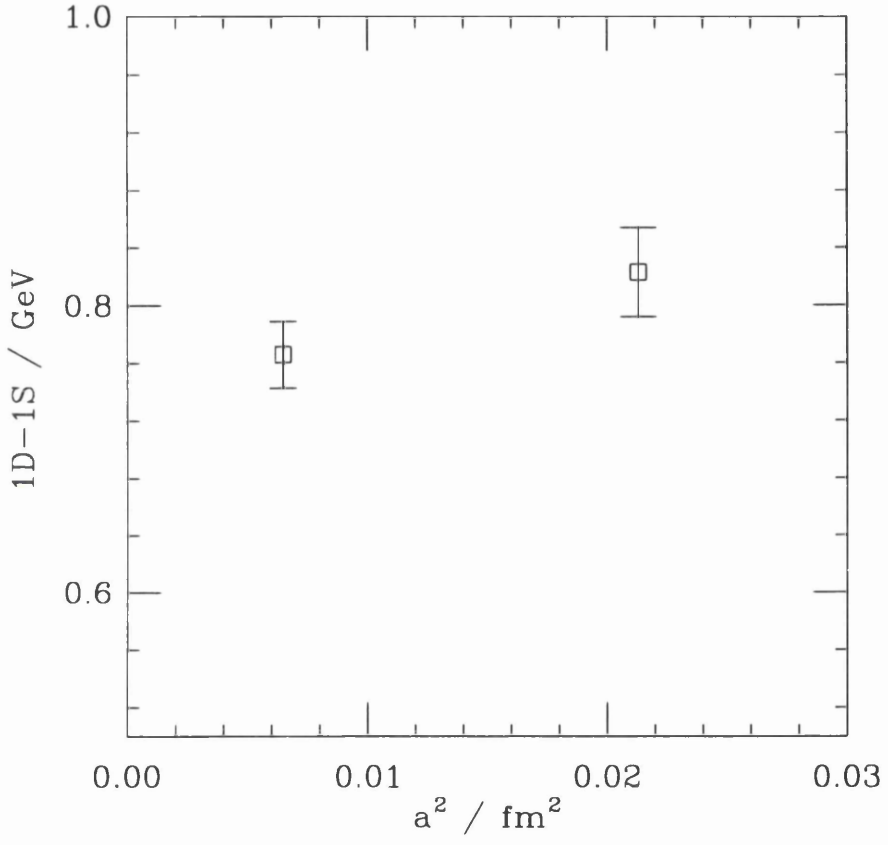

Figure 4.9: The graph shows a scaling plot of the $1D - 1S$ splittings results for $\beta = 5.7$ and $\beta = 6.0$ against a^2.

Chapter 5

Conclusions

The method of NRQCD has been shown in the past to be an excellent method for simulation and analysis of the S and P states of the upsilon spectrum [31, 32]. The quenched simulations at $\beta = 6.0$ of Chapter 4 provided determinations of the D states of the upsilon spectrum, using the methods of vector and matrix fitting. Although the predictions for each of the D states had fairly high errors, any discrepancies between vector and matrix fits for a particular state were within 2 sigma. Quenched simulation data on a coarser lattice at $\beta = 5.7$ was also studied for the $^1D_2$ ground state to provide scaling analysis with the $\beta = 6.0$ simulation data. Results of the scaling analysis gave a $1D - 1S$ splitting of 0.823(31) GeV for $\beta = 5.7$ and a splitting of 0.761(20) GeV for $\beta = 6.0$. These results point to a lack of scaling. However, the fact that only single exponential fits were carried out for $\beta = 5.7$, could be contributary to the lack of scaling.

Although no upsilon D states have been observed experimentally, an experimental D state for charmonium has been observed. It is the $\psi(3770)$ and is almost certainly a $^3D_1$ state (probably with some S state admixture). So the splitting between the $\psi(3770)$ and the J/ψ gives some idea of the expected splitting between Υ ($^3S_1$) and the D states (although of course a spin average would be preferable for a better estimate). That the $\psi(3770)$ is a D state is immediately apparent when the levels are plotted and it's width examined for the annihilation decay to e^+e^- [16]. It's width is much smaller than the other states and is pro-

portional to the wavefunction at the origin squared in perturbation theory. So if it was entirely a D state this would be zero and the state could never be made in e^+e^- collisions. This is why it is so hard to find them. For the upsilon D states, they will not be seen experimentally if there is not some mixing with the S states to give them some wavefunction at the origin.

From experimental studies of charmonium, the 1^3D_1 splitting with the spin averaged S state is 702 MeV. Also the potential model results quoted in Chapter 2 seem to be expecting a splitting of around 700 MeV. So either we are seeing scaling violations and the 'continuum' splitting is more like 700 MeV, or we are seeing quenching errors. However the standard arguments about quenching are that it affects states with wavefunction at the origin, which would mean that the 1D-1S splitting should not be affected any more than the 1P-1S splitting (which was used to set the scale). The other possibility is a finite volume effect squeezing the D states in the lattice 'box' and pushing up their mass. Calculations would need to be carried out on a bigger spatial volume (in physical units) to check this.

Finally in conclusion, from the single state fits the ordering of the D states are about right but the fine structure could not be determined accurately from the ratio fits. This was probably due to discretisation errors and possibly a lack of statistics. These results could be improved upon by going to a finer lattice or further improving the NRQCD action. This would allow a repeat of these results but with smaller discretisation errors. Increased statistics would probably also be neccessary and perhaps on a finer lattice, although all of these improvements would require a huge amount of computer resources.

Bibliography

[1] L. H. Ryder, *Quantum Field Theory*, Cambridge University Press (1991).

[2] H. J. Rothe, *Lattice Gauge Theories, An Introduction*, World Scientific (1992).

[3] J. F. Donoghue, E. Golowich and B. R. Holstein, *Dynamics of the Standard Model*, Cambridge (1992).

[4] I. J. R. Aitchison and A. J. G. Hey, *Gauge Theories in Particle Physics*, Adam Hilger (1989)

[5] W. Lucha, F. F. Schöberl and D. Gromes, *Bound States of Quarks*, Phys. Rep. **200**, 127 (1991).

[6] W. Lucha, F. F. Schöberl, *Effective Potential Models for Hadrons*, hep-ph/9601263.

[7] D. Gromes, *Effective Hamiltonian for Charmonium and Similar Two Fermion Systems* Nucl. Phys. B. **131**, 80 (1977).

[8] L. D. Landau and E. M. Lifshitz, *Quantum Mechanics*, Pergamon Press (1977).

[9] E. Eichten, K. Gottfried, T. Kinoshita, K. D. Lane and T. M. Yan, *Charmonium: Comparison With Experiment*, Phys. Rev. D. **21**, 203 (1980).

[10] L. Montanet et al., *Particle Data Group*, Phys. Rev. D. **50**, 1173 (1994).

[11] W. Kwong, J. L. Rosner, *D-Wave Quarkonium Levels of the* Υ *Family*, Phys. Rev. D. **38**, 279 (1988).

[12] E. Eichten, F. Feinberg, *Spin-Dependent Forces in Quantum Chromodynamics*, Phys. Rev. D. **23**, 2724 (1981).

[13] E. Eichten, C. Quigg, *Mesons with Beauty and Charm: Spectroscopy*, Phys. Rev. D. **49**, 5845 (1994).

[14] W. Kwong, J. L. Rosner, C. Quigg, *Heavy Quark Systems*, Annu. Rev. Nucl. Part. Sci. **37**, 325 (1987).

[15] H. B. Thacker C. Quigg and J. L. Rosner, *Inverse Scattering for Quarkonium Systems. II. Application to ψ and Υ Families*, Phys. Rev. D. **18**, 287 (1978).

[16] C. T. H. Davies, *The Heavy Hadron Spectrum*, Lectures at Schladming School (1997).

[17] G. S. Bali, K. Schilling and A. Wachter, *Complete $\mathcal{O}(v^2)$ corrections to the static interquark potential from SU(3) gauge theory*, Phys. Rev. D. **56**, 2566 (1997).

[18] B. A. Thacker and G. P. Lepage, *Heavy-quark bound states in lattice QCD*, Phys. Rev. D **43**, 196 (1991).

[19] G. P. Lepage and B. A. Thacker, *Effective Lagrangians for Simulating of Heavy Quark Systems*, Nucl. Phys. B (Proc. Suppl.) **4**, 199 (1988).

[20] G. P. Lepage, L. Magnea, C. Nakhleh, U. Magnea and K. Hornbostel, *Improved Nonrelativistic QCD for Heavy Quark Physics*, Phys. Rev. D **46**, 4052 (1992).

[21] G. T. Bodwin, E. Braaten and G. P. Lepage, *Rigorous QCD Analysis of Inclusive Annihilation and Production of Heavy Quarkonium*, Phys. Rev. D **51**, 1125 (1995).

[22] W. Greiner, *Relativstic Quantum Mechanics*, Springer-Verlag (1990).

[23] J. P. Costella and B. H. J. McKellar, *The Foldy-Wouthuysen Transformation*, Amer. Journ. Phys. **63**, 1119 (1995).

[24] C. Itzykson and J. B. Zuber, *Quantum Field Theories*, McGraw-Hill (1980).

[25] P. M. Mathews and K. Venkatesan, *A Textbook of Quantum Mechanics*, Tata McGraw-Hill (1993).

[26] B. Sheikholeslami and R. Wohlert, *Improved Continuum Limit Lattice Action for QCD with Wilson Fermions*, Nucl. Phys. B **259**, 572 (1985).

[27] G. P. Lepage and P. B. Mackenzie, *On the Viability of Lattice Perturbation Theory*, Phys. Rev. D **48**, 2250 (1993).

[28] C. J. Morningstar, *Radiative-corrections to the kinetic couplings in nonrelativistic lattice QCD* Phys. Rev. D **50**, 5902 (1994).

[29] A. J. Lidsey, PhD thesis, *Non-Relativistic QCD on the Lattice.*

[30] I. Montvay, G. Munster, *Quantum Fields on a Lattice*, Cambridge Monographs on Mathematical Physics (1997).

[31] C. T. H. Davies, K. Hornbostel, A. Langnau, G. P. Lepage, A. Lidsey, J. Shigemitsu and J. Sloan, *Precision Υ spectroscopy from nonrelativistic lattice QCD*, Phys. Rev. D **50**, 6963 (1994).

[32] P. McCallum, PhD thesis, *Upsilon Spectroscopy Using Lattice QCD.*

[33] T. Manke et al., *Υ spectrum from NRQCD with improved action.*

[34] C. T. H. Davies, K. Hornbostel, G. P. Lepage, A. Lidsey, P. McCallum, J. Shigemitsu, J. sloan, *Scaling of the Υ spectrum in Lattice NRQCD*, hep-lat/9802024.